ACOUSTIC WAVE PROPAGATION AND INTENSITY FLUCTUATIONS DUE TO SHALLOW WATER INTERNAL WAVES IN THE 2006 SHALLOW WATER EXPERIMENT

by

Jing Luo

A dissertation submitted to the Faculty of the University of Delaware in partial fulfillment of the requirements for the degree of Doctor of Philosophy in Electrical Engineering

Aug. 2012

© 2012 Jing Luo
All Rights Reserved

TABLE OF CONTENTS

LIST OF FIGURES . . . . . **vii**
ABSTRACT . . . . . **xiii**

Chapter

1 INTRODUCTION **1**

1.1 Introduce the problem (acoustic propagation in a IW environment) . 1

1.1.1 Solitons in ocean 1
1.1.2 Acoustical effects of solitons 3

1.2 Outline of Thesis 4

2 THEORY OF SHALLOW WATER WAVEGUIDE AND COMPUTER MODELS **7**

2.1 Linear Wave Equation and Helmholtz Equation 7
2.2 Normal Modes 8

2.2.1 Normal Modes for Range-Independent Environments 8
2.2.2 Normal Modes for Range-dependent Environments 9
2.2.3 Normal Modes for 3-D Environments 10

Horizontal Refraction Equation 10

2.2.4 Mode Filtering 12

2.3 Parabolic Equation 13

2.3.1 Split-Step Fourier Transform Method 14

2.3.2 Standard and Wide Angle Approximation 17

2.4 A Brief introduction to Nonlinear Internal Waves (Soliton) 19

2.4.1 Reconstruction of 3D IW environment 19

The leading front of internal wave maintains a straight line . . 20
Waveform changes only slightly along fronts 20
Constant internal wave speed and direction 21

2.4.2 Water temperature extrapolation 21
2.4.3 Reconstruct a 3D temperature field 22

3 SHALLOW WATER 2006 EXPERIMENT 23

3.1 Experiment site and environment moorings 23
3.2 Acoustic moorings 24

3.2.1 Sources 24
3.2.2 Receiver array 25

3.3 Internal wave observation 26

3.3.1 Internal wave event 50 27

4 ACOUSTIC OBSERVATIONS IN EVENT 50 35

4.1 Transmission from the fixed source(NRL 300Hz) 36

4.1.1 Phase I: 20:30-20:37GMT & 21:00-21:07GMT 36
4.1.2 Phase II: 21:30-21:37GMT 37
4.1.3 Phase III: 22:00-22:07GMT, 22:30-22:37GMT, 23:00-23:07GMT & 23:30-23:37GMT 37
4.1.4 Phase IV: after 23:30GMT 38
4.1.5 23:00GMT-23:07GMT 38
4.1.6 23:30GMT-23:37GMT 38

4.2 Transmissions from mobile source (R/V Sharp) 62

4.2.1 21:11GMT-21:27GMT 62
4.2.2 21:41GMT-21:57GMT 62
4.2.3 22:11GMT-22:27GMT 62
4.2.4 22:41GMT-22:57GMT 62

4.2.5 23:11GMT-23:27GMT 63

5 ANALYSIS AND MODELING 77

5.1 Intensity fluctuation and statistics 77
5.2 Acoustic signal coherence time and length 79

5.2.1 Fixed source 79
5.2.2 Moving source 80

5.3 Behavior of horizontal ray beams 80

5.3.1 Horizontal Ray 80
5.3.2 Horizontal beamforming 80
5.3.3 Single mode propagation 80
5.3.4 Mode coupling 80

5.4 Horizontal Lloyd's mirror effect 80

5.4.1 Two-dimensional case 80
5.4.2 Three-dimensional case 82

6 SUMMARY 93

BIBLIOGRAPHY 95

LIST OF FIGURES

1.1 Internal solitary waves 5

1.2 Two-layer model of an internal solition. 6

3.1 Map of SW06 experiment site and the locations of the environment and acoustic moorings 29

3.2 Current data record by ADCP at mooring SW32 during event 50 in SW06 experiment (upper panel) and temperature data at the same location. 30

3.3 Image of SW06 experiment site taken by the Canadian RADARSAT satellite on 16 August, 2006. 31

3.4 Depth of 18^oC degree thermocline on Aug. 17, 2006, recorded on WHOI Sharp VLA (SW54) 32

3.5 Angular distribution of the direction of the internal wave recored during SW06. 33

3.6 Diagram showing the fixed acoustic source(NRL300), receiver array (Shark VHLA) and the semi-circular track of R/V Sharp the IW event 50. Zone 1 5 represent the location of J15 in the time periods when it was transmitting in event 50. 34

4.1 Matched filter output of received chirp signal on VLA Shark at GMT 20:30:04, Aug 16th. The red dash line shows the centroid arrival time, which is different than the peak arrival time. 39

4.2 Temperature record at three location along the fixed sourc-receiver track. Panel (a), (b) and (c) show the temperature at the NRL300 source (SW45), the midpoint (SW20) and the Shark VLA (SW54). 40

4.3 Temperature record at three location along the fixed sourc-receiver track. Panel (a), (b) and (c) show the temperature at the NRL300 source (SW45), the midpoint (SW20) and the Shark VLA (SW54). 41

4.4 Interpolated internal wave field at 20:30GMT, Aug. 17, water depth = 20m. (Refer to section 3.4 for detailed interpolation method) . . 42

4.5 Received signal on Shark VLA (top), HLA (bottom) and signal intensity (middle) from Aug.17 20:30GMT to 20:37GMT 43

4.6 Mode decomposition of received signal on Shark VLA. Left column: mode 1-3, right column: mode 4-6 44

4.7 Surface expression of internal wave package at 21:00GMT, Aug. 17, recorded by R/V Sharp and R/V Oceanus. Blue and red lines indicate their movements, respectively. (Blue: R/V Sharp's, red: R/V Oceanus' 45

4.8 Interpolated internal wave field at 21:00GMT, Aug. 17, water depth = 20m. (Refer to section 3.4 for detailed interpolation method) . . 46

4.9 Received signal on Shark VLA (top), HLA (bottom) and signal intensity (middle) from Aug.17 21:00GMT to 21:07GMT 47

4.10 Mode decomposition of received signal on Shark VLA. Left column: mode 1-3, right column: mode 4-6 48

4.11 Mode coupling between mode 1 4 49

4.12 Surface expression of internal wave package at 21:30GMT, Aug. 17, recorded by R/V Sharp and R/V Oceanus. Blue and red lines indicate their movements, respectively. (Blue: R/V Sharp's, red: R/V Oceanus' 50

4.13 Interpolated internal wave field at 21:30GMT, Aug. 17, water depth = 20m. (Refer to section 3.4 for detailed interpolation method) . . 51

4.14 Received signal on Shark VLA (top), HLA (bottom) and signal intensity (middle) from Aug.17 21:30GMT to 21:37GMT 52

4.15 Mode decomposition of received signal on Shark VLA. Left column: mode 1-3, right column: mode 4-6 53

4.16 Surface expression of internal wave package at 22:00GMT, Aug. 17, recorded by R/V Sharp and R/V Oceanus. Blue and red lines indicate their movements, respectively. (Blue: R/V Sharp's, red: R/V Oceanus' 54

4.17 Interpolated internal wave field at 22:00GMT, Aug. 17, water depth = 20m. (Refer to section 3.4 for detailed interpolation method) . . 55

4.18 Received signal on Shark VLA (top), HLA (bottom) and signal intensity (middle) from Aug.17 22:00GMT to 22:07GMT 56

4.19 Mode decomposition of received signal on Shark VLA. Left column: mode 1-3, right column: mode 4-6 57

4.20 Surface expression of internal wave package at 22:30GMT, Aug. 17, recorded by R/V Sharp and R/V Oceanus. Blue and red lines indicate their movements, respectively. (Blue: R/V Sharp's, red: R/V Oceanus' 58

4.21 Interpolated internal wave field at 22:30GMT, Aug. 17, water depth = 20m. (Refer to section 3.4 for detailed interpolation method) . . 59

4.22 Received signal on Shark VLA (top), HLA (bottom) and signal intensity (middle) from Aug.17 22:30GMT to 22:37GMT 60

4.23 Mode decomposition of received signal on Shark VLA. Left column: mode 1-3, right column: mode 4-6 61

4.24 Temperature record at three location along the fixed sourc-receiver track. Panel (a), (b) and (c) show the temperature at the NRL300 source (SW45), the midpoint (SW20) and the Shark VLA (SW54). 64

4.25 Surface expression of internal wave package at 21:15GMT, Aug. 17, recorded by R/V Sharp and R/V Oceanus. Blue and red lines indicate their movements, respectively. (Blue: R/V Sharp's, red: R/V Oceanus' 65

4.26 Received signal on Shark VLA (top), HLA (bottom) and signal intensity (middle) from Aug.17 21:15GMT to 21:25GMT 66

4.27 Surface expression of internal wave package at 21:41GMT, Aug. 17, recorded by R/V Sharp and R/V Oceanus. Blue and red lines indicate their movements, respectively. (Blue: R/V Sharp's, red: R/V Oceanus' 67

4.28 Received signal on Shark VLA (top), HLA (bottom) and signal intensity (middle) from Aug.17 21:41GMT to 21:56GMT 68

4.29 Surface expression of internal wave package at 22:11GMT, Aug. 17, recorded by R/V Sharp and R/V Oceanus. Blue and red lines indicate their movements, respectively. (Blue: R/V Sharp's, red: R/V Oceanus' 69

4.30 Received signal on Shark VLA (top), HLA (bottom) and signal intensity (middle) from Aug.17 22:11GMT to 22:26GMT 70

4.31 Surface expression of internal wave package at 22:41GMT, Aug. 17, recorded by R/V Sharp and R/V Oceanus. Blue and red lines indicate their movements, respectively. (Blue: R/V Sharp's, red: R/V Oceanus' 71

4.32 Received signal on Shark VLA (top), HLA (bottom) and signal intensity (middle) from Aug.17 22:41GMT to 22:46GMT 72

4.33 Surface expression of internal wave package at 23:11GMT, Aug. 17, recorded by R/V Sharp and R/V Oceanus. Blue and red lines indicate their movements, respectively. (Blue: R/V Sharp's, red: R/V Oceanus' 73

4.34 Received signal on Shark VLA (top), HLA (bottom) and signal intensity (middle) from Aug.17 23:11GMT to 23:26GMT 74

4.35 Data of depth-integrated intensity and estimated angle for each zone 75

5.1 Depth integrated intensity from PE modeling results at 21:30:15GMT and 21:33:45GMT repectively, with a short white line indicating the length and direction of the Shark HLA 83

5.2 Depth integrated intensity from PE modeling results at 22:00:00GMT and 22:03:35GMT repectively, with a short white line indicating the length and direction of the Shark HLA 83

5.3 Beamforming results on Shark HLA 84

5.4 From left to right, vertical modes 1-4 excited by a 330Hz frequency signal. Temperature data were recorded at NRL300 source, GMT21:30, Aug 17, 2006. 85

5.5 Broadband model decomposition of acoustic signal from 21:30GMT to 21:37GMT (mode1-6). 86

5.6 PE modal coupling. From left to right, the excited modes at source; from top to bottom, the coupled modes. Most energy is confined at the excited mode at the source, which is consistent with the theory about adiabatic propagation at near-parallel environment. Higher modes show stronger coupling effects than lower modes. Energy from mode 1 will couple to mode 3, while mode 4 can couple up to mode 8. 87

5.7 (Modal dependence) Acoustic intensity is shown for vertical modes 1 3 at GMT21:30:00(left) and GMT 21:43:40(right) respectively. A single frequency signal (330Hz) source is placed at (0,0), depth = 70m. Temperature contour overlay shows the passing internal waves. 88

5.8 (Frequency dependence) Acoustic integrated sound intensity of vertical modes 1-3 at frequency = 270Hz, 330Hz at GMT21:30:00. Source position (x,y) = (0, 0) and source depth = 70m. Temperature contour overlay shows the passing internal waves. 89

5.9 3-D PE modeling results showing the acoustic intensity and the temperature contour at depth 20 m. Source is located at point (0,0) and white dashed lines indicate the acoustic track. 90

5.10 (a) Data and (b) model comparison of the intensity as a function of depth (top panels) and depth-integrated intensity (bottom panels) on Zone 3, August 17, 2006 at 22:11 to 22:26 GMT. The occurrence of focusing at geotime about 22:21:30 observed in the data was well predicted by the model. 90

5.11 PE model results and experiment data comparison for moving source J15. Solid line shows the results of 3D PE model. The propagating angles are shown at the top for the beginning and end of each transmission session 91

5.12 autocovariance function of channel 0 at 21:00 91

5.13 autocovariance function of channel 0 at 21:30 92

5.14 autocovariance function of channel 0 at 22:00 92

ABSTRACT

Fluctuations of the low frequency sound field in the presence of an internal solitary wave packet during the Shallow Water '06 (SW06) experiment are analyzed. Acoustic, environmental, and on-board ship radar image data were collected simultaneously before, during, and after a strong internal solitary wave packet passed through the acoustic track. Preliminary analysis of the acoustic wave temporal intensity fluctuations agrees with previously observed phenomena and the existing theory of the horizontal refraction mechanism, which causes focusing and defocusing when the acoustic track is nearly parallel to the front of the internal waves.

Chapter 1

INTRODUCTION

Underwater acoustic propagation has been an active research field for more than a century now. Originated from military purposes, its applications have expanded to other areas such as environment monitoring, navigation and underwater communication in modern era. Scientists have made great advancements in understanding the theories and developing the modeling tools for underwater acoustics, yet the shallow water still remains one of the most challenging environments due to the combination of different ocean phenomena at different temporal and spacial scales, among which, is the nonlinear internal waves generated at the shelf break region.

1.1 Introduce the problem (acoustic propagation in a IW environment)

1.1.1 Solitons in ocean

Isolated nonlinear wave has been reported by scientists since 19th century, and the theoretical explanation was given by Boussinesq and Rayleigh in 1870s, and by Korteweg and de Vries in 1895[1]. More recently, a number of experiments for internal wave solitons were conducted, and the findings and analysis have been reported by, e.g., Ostrovsky and Stepanyants[4], Apel[7], Duda and Farmer[5].

Internal soliton waves can manifest itself on sea surface, whose expression is usually large enough and can been seen on radar. Solitons, despite the name, travels in package or trains consisting of about 10 distinguishable waves and a less separated, smoother tail.

The internal solitons normally appear as a depression in the pycnocline. Apel et al. [7] provide a solution for the internal wave KdV equation,

$$\eta_t + c\eta_x + \alpha\eta\eta_x + \beta\eta_{xxx} = 0, \tag{1.1}$$

where η is the vertical displacement of an isopycnal surface from their equilibrium levels. The rescaled nonlinear and dispersion parameters(α and β, respectively) are

$$\alpha = \frac{3c\sigma}{2H}, \beta = \frac{cDH^2}{2} \tag{1.2}$$

where σ and D are nondimensional parameters describing nonlinearity and high-frequency dispersion, respectively. The quantities α and β are environmental parameters and incorporate the effects of buoyancy (density stratification), shear currents in general and depth.

In a two-layer simplified model,

$$c = \left[\frac{g(\rho_2 - \rho_1)h_1 h_2}{\rho_2 h_1 + \rho_1 h_2}\right]^{1/2} \tag{1.3}$$

$$\alpha = \frac{3c}{2h_1 h_2}\frac{\rho_2 h_1^2 - \rho_1 h_2^2}{\rho_2 h_1 + \rho_1 h_2} \tag{1.4}$$

$$\beta = \frac{ch_1 h_2}{6}\frac{\rho_1 h_1 + \rho_2 h_2}{\rho_2 h_1 + \rho_1 h_2} \tag{1.5}$$

where h_1 and h_2 are the thickness of two layers.

The soliary solution to the KdV equation is,

$$\eta(x,t) = \eta_0 sech^2\left(\frac{x - Vt}{\Delta}\right). \tag{1.6}$$

where the soliton phase speed, V is

$$V = c + \alpha\eta_0/3 \tag{1.7}$$

and the characteristic width, Δ, is given by,

$$\Delta^2 = \frac{12\beta}{\alpha\eta_0} \tag{1.8}$$

From the characteristic width equation, η_0 has the some sign of α. In a common case of shallow pycnocline over a deeper layer (i.e., $\rho_2 h_1^2 < \rho_1 h_2^2$), η is negative, which indecates a depressive wave, consistant with most experimental observations.

We use some parameter from SW06 experiment in this simply model. $\eta_0 = -20m$, $\rho_1 = 1012.05kg/m^3$, $\rho_2 = 1015.27kg/m^3$, $h_1 = 15m$,$h_2 = 55m$. The soliton phase speed, estimated from thermistor data (see Chap. 4) is $V = 0.92m/s$.

The tidal interaction with bottom feature (e.g., shelf break) appears to be the dominant mechanism for generation of the internal waves near the continents. At least two mechanisms have been advanced to explain the generation process at the shelf break. The first hypothesizes that the when tide will be scattered when it arrives at the shelf break from a relative smooth bathymetric area (i.e. the continental shelf). The second is a kind of lee-wave mechanism, wherein tidal flow directed offshore beyond the shelf break results in an oscillating depression of the pycnocline just offshore of the break.

1.1.2 Acoustical effects of solitons

In 1991, Zhou *et al.*[8] first reported the acoustical effects of soliton in the Yellow Sea series of experiments, where anomalously high propagation loss up to 30-40dB was observed. These high losses were attributed to Bragg resonant scattering when acoustic signal travels through a strong internal wave train. Preisig & Duda [9] have shown, with detailed numerical simulation, coupled mode is the main mechanism responds for cross-wavefront scattering.

For the topic of propagating along the IW wavefront. Katznelson & Perseselkov [10] predicted via the theory the detailed scattering of so-called "horizontal sound duct" formed by two neighboring high sound-speed solitons in a wave train with a relatively low speed region in between. Their findings have been confirmed by Badiey *et al.*.[11],[12] with great consistency. This ducting effect can easily produce 6-8dB level increases in low frequency broadband transmissions. Moreover, since this is a fully three-dimensional effect, the focusing of energy gives amplitude fluctuation over and about the one would expect from a saturated normal mode multipath interference in two dimensions(x-y plane). Additionally, the description of such propagation requires a fully 3D theory and numerical model, which has been a active research topic recently.

There are also other experiments and theoretical studies dedicated to the case between these two extremes. Rubenstrein [13] reported and modeled an experiment

conducted in Gulf of Mexico where the acoustic signal shows a strong resonance with the passing internal wave train at an intersecting angle of 30 degree.

1.2 Outline of Thesis

Chapter 2 discusses the basic theory of acoustic propagation in a waveguide; introduce the normal mode propagation and the associated topics like mode filtering; expand 2D to 3D model; horizontal ray and vertical mode theory; the PE solution as an alternative technique the acoustic field.

Chapter 3 discusses the SW06 experiment and the data collection and processes in this thesis: acoustic and oceanographic experimental configuration such as the geometry of the acoustic source and receiver, transmitted signals and their characteristics, and oceanographic data. The oceanographic data are used to reconstruct a detailed 3D environment that is critical to the modeling.

Chapter 4 discuss the analysis of the acoustic signal received in SW06. Signal transmitted from fixed and moving sources and received on an L-shaped array sources (i.e., 32 horizontal and 16 vertical hydrophones). Details of the data are explained in this chapter. The WHOI 300Hz source provides a better signal to noise ration (SNR) despite the longer propagating distance, while the J15 source gives an unique opportunity to study the angle dependence with a better angular coverage. Both transmissions are first modeled with horizontal-ray vertical mode model for its concision and the analogy with ray theory. Then the data are compared with PE model results.

Chapter 5 summarizes the conclusions of this research and proposes the future investigation.

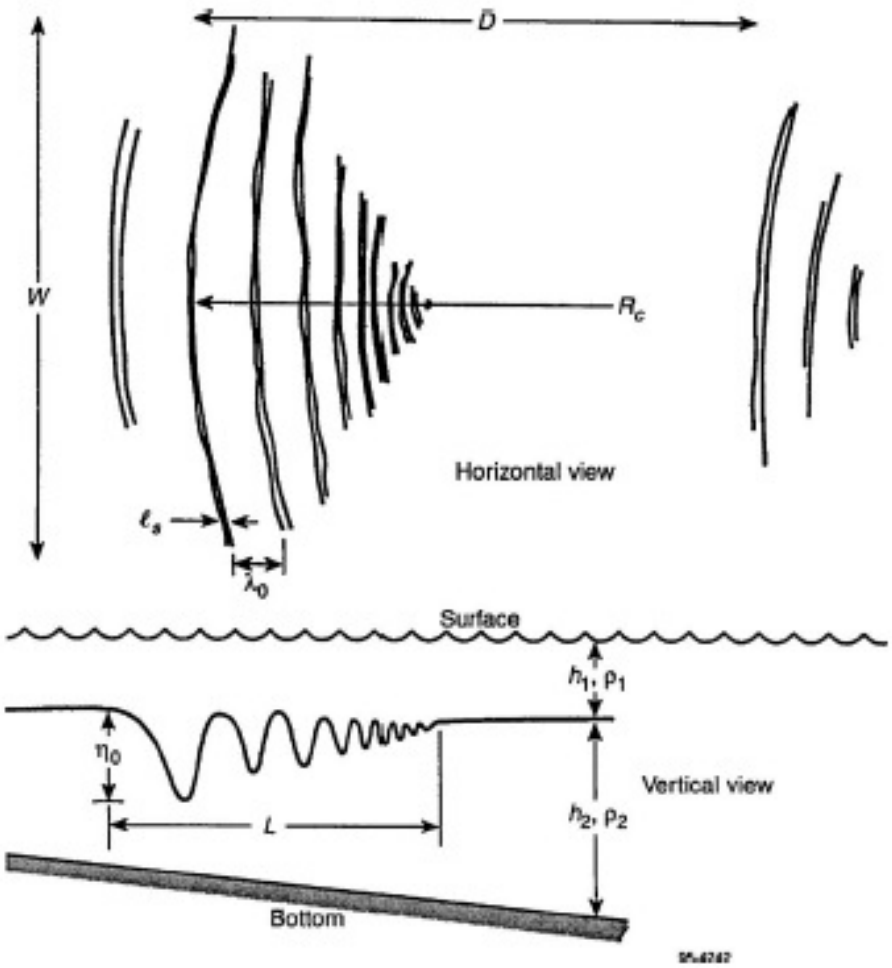

Figure 1.1: Internal solitary waves

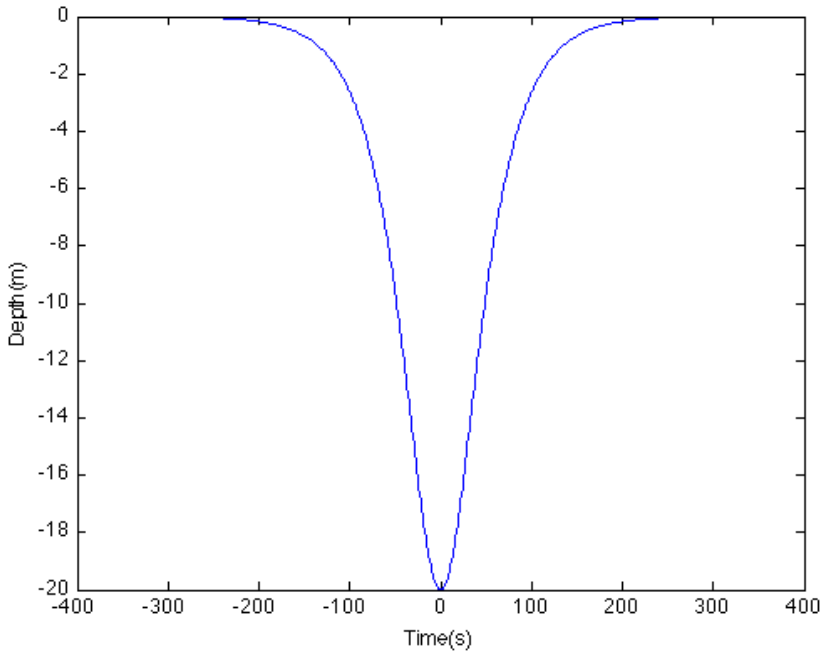

Figure 1.2: Two-layer model of an internal solition.

Chapter 2

THEORY OF SHALLOW WATER WAVEGUIDE AND COMPUTER MODELS

2.1 Linear Wave Equation and Helmholtz Equation

We start from linear wave equation

$$\frac{\partial \rho'}{\partial t} = -\rho_0 \nabla \cdot \mathbf{v}, \tag{2.1}$$

$$\frac{\partial \mathbf{v}}{\partial t} = -\frac{1}{\rho_0} \nabla p'(\rho), \tag{2.2}$$

$$p' = \rho' c^2. \tag{2.3}$$

Where c is the speed of sound in the fluid, ρ is the density, $\mathbf{v}$ the particle velocity, p the pressure. Small perturbations are used for pressure and density, $p = p_0 + p'$, $\rho = \rho_0 = \rho'$. And $\mathbf{v}$ is also a small quantity compare to c.

Rearrange Eq.2.1-Eq.2.3 to obtain a wave equation for pressure,

$$\rho \nabla \cdot \left(\frac{1}{\rho} \nabla p \right) - \frac{1}{c^2} \frac{\partial^2 p}{\partial t^2} = 0, \tag{2.4}$$

where we have omitted the primes for pressure and density perturbations. If the density is constant is space, Eq.2.4 can be replaced by

$$\nabla^2 p - \frac{1}{c^2} \frac{\partial^2 p}{\partial t^2} = 0. \tag{2.5}$$

The coefficients to the two differential operators in Eq.2.4 are independent of time, by use of the Forier transform, the wave equation becomes to Helmholtz equation,

$$\rho \nabla \cdot \left(\frac{1}{\rho} \nabla p \right) + k(\mathbf{r})^2 p = 0, \tag{2.6}$$

or, in the case of constant density,

$$\nabla^2 p + k(\mathbf{r})^2 p = 0. \tag{2.7}$$

where $k(\mathbf{r})$ is the medium wavenumber at radial frequency ω,

$$k(\mathbf{r}) = \frac{\omega}{c(\mathbf{r})}. \tag{2.8}$$

2.2 Normal Modes

2.2.1 Normal Modes for Range-Independent Environments

In a cylindrical coordinate system $\mathbf{r} = (r, \varphi, z)$, assuming sound speed and density depending only on depth z, with a point source located at coordinates $r = 0, z = z_s$, the Helmholtz equation:

$$\frac{1}{r}\frac{\partial}{\partial r}\left(r\frac{\partial p}{\partial r}\right) + \rho(z)\frac{\partial}{\partial z}\left(\frac{1}{\rho(z)}\frac{\partial p}{\partial z}\right) + \frac{\omega^2}{c^2(z)}p = -\frac{\delta(r)\delta(z - z_s)}{2\pi r}. \tag{2.9}$$

Eq.2.9 is readily solved via the technique of separation of variables. Assuming a solution of the unforced equation in the form $p(r, z) = \Phi(r)\Psi(z)$. After substuting into the above equation and dividing through by $\Phi(r)\Psi(z)$ we find,

$$\frac{1}{\Phi}\left[\frac{1}{r}\frac{d}{dr}\left(r\frac{d\Phi}{dr}\right)\right] + \frac{1}{\Psi}\left[\rho(z)\frac{d}{dz}\left(\frac{1}{\rho(z)}\frac{d\Psi}{dz}\right) + \frac{\omega^2}{c^2(z)}\Psi\right] = 0. \tag{2.10}$$

Denoting the separation constant by k_{rm}^2, we obtain the modal equation,

$$\rho(z)\frac{d}{dz}\left[\frac{1}{\rho(z)}\frac{d\Psi_m(z)}{dz}\right] + \left[\frac{\omega^2}{c^2(z)} - k_{rm}^2\right]\Psi_m(z) = 0. \tag{2.11}$$

where k_m is the mode m horizontal wavenumber, and each Ψ_m is subject to certain boundary conditions that depend on the environment. For instance, with a pressure-release surface located at $z = 0$ and a perfectly rigid bottom located at $z = D$, the corresponding boundary condition for Ψ is

$$\Psi(0) = 0, \qquad \left.\frac{d\Psi}{dz}\right|_{z=D} = 0. \tag{2.12}$$

The modal equation is a classical Sturm-Liouville eigenvalue problem whose properties are well-known. The function $\Psi_m(z)$ is an eigenfunction and k_{rm} is an eigenvalue. The modes are orthogonal, i.e.,

$$\int_0^D \frac{\Psi_m(z)\Psi_n(z)}{\rho(z)} d(z) = 0, \qquad \text{for} \qquad m \neq n. \tag{2.13}$$

The solutions of the modal equation are arbitrary to a multiplicative constant, therefore the mode shape function is usually normalized so that

$$\int_0^D \frac{\Psi_m^2(z)}{\rho(z)} dz = 1. \tag{2.14}$$

The total acoustic pressure field takes the form

$$p(r,z) = \sum_m \Phi_m(r)\Psi_m(z) \tag{2.15}$$

where $\Psi_m(z)$ is the vertical modal shape, and $\Phi_m(r)$ is the mode coefficient for mode m at range r.

2.2.2 Normal Modes for Range-dependent Environments

For a range-dependent environment, the Helmholtz equation in cylindrical coordinates is,

$$\frac{\rho}{r}\frac{\partial}{\partial r}\left(\frac{r}{\rho}\frac{\partial p}{\partial r}\right) + \rho\frac{\partial}{\partial z}\left(\frac{1}{\rho}\frac{\partial p}{\partial z}\right) + \frac{\omega^2}{c^2(r,z)}p = -\frac{\delta(r)\delta(z-z_s)}{2\pi r}. \tag{2.16}$$

Since the modes form a complete set, we can represent the solution at any range as a sum of local modes. We therefore seek a solution of the range-dependent problem in the form

$$p(r,z) = \sum_m \Phi_m(r)\Psi_m(r,z) \tag{2.17}$$

where $\Psi_m(r,z)$ are the local modes defined by

$$\rho(r,z)\frac{\partial}{\partial z}\left[\frac{1}{\rho(r,z)}\frac{\partial \Psi_m(r,z)}{\partial z}\right] + \left[\frac{\omega^2}{c^2(r,z)} - k_{rm}^2(r)\right]\Psi_m(r,z) = 0. \tag{2.18}$$

Thus, at any range r, $\Psi)m(r,z)$ is found by solving the depth-separated modal equation with the environmental properties at that range. Substitution in the Helmholtz equation yields

$$\sum_m \frac{\rho}{r}\frac{\partial}{\partial r}\left(\frac{r}{\rho}\frac{\partial(\Phi_m\Psi_m)}{\partial r}\right) + \sum_m k_{rm}^2(r)\Phi_m\Psi_m = -\frac{\delta(r)\delta(z-z_s)}{2\pi r}. \tag{2.19}$$

We now assume that ρ is independent of r. We can apply the operator

$$\int (\cdot) \frac{\Psi_n(r,z)}{\rho} dz, \tag{2.20}$$

and because of the orthogonality property many of the terms in the sum will disappear. The result is

$$\frac{1}{r}\frac{d}{dr}\left(r\frac{d\Phi_n}{dr}\right) + \sum_m 2B_{mn}\frac{d\Phi_m}{dr} + \sum_m A_{mn}\Phi_m + k * 2_{rn}(r)\Phi_n = -\frac{\delta(r)\Psi_n(z_s)}{2\pi r}, \tag{2.21}$$

where

$$A_{mn} = \int \frac{1}{r}\frac{\partial}{\partial r}\left(r\frac{\partial \Psi_m}{\partial r}\right)\frac{\Psi_n}{\rho} dz, \tag{2.22}$$

$$B_{mn} = \int \frac{\partial \Psi_m}{\partial r}\frac{\Psi_n}{\rho} dz. \tag{2.23}$$

Equation 2.21 is a statement of coupled modes written for the case of continuous variation of sound speed. It can be solved directly by, for instance finite-differences. The adiabatic approximation can now be stated simply as the assumption that the coupling matrics A_{mn} and B_{mn} are negligible. We then obtain a set of decoupled equations,

$$\frac{1}{r}\frac{d}{dr}\left(r\frac{d\Phi_n}{dr}\right) + k_{rn}^2(r)\Phi_n = -\frac{\delta(r)\Psi_n(z_s)}{2\pi r} \tag{2.24}$$

2.2.3 Normal Modes for 3-D Environments

To extend the 2-D model to a 3-D model, a direct approach is to simply running the 2-D models repeatedly along a number of different bearings. Along each bearing one then uses the sound-speed profile and bathymetry for that track. Combining these results along numerous bearings allow one to build-up a 3-D image of the acoustic field, which, however, is just an N $\times$ 2-D calculation where horizontal refraction has been ignored. The "Horizontal ray vertical modes" approach introduced in the next section is able to overcome this problem.

Horizontal Refraction Equation

We return to the Helmholtz equation in three dimensions,

$$\rho\nabla\cdot\left(\frac{1}{\rho}\nabla p\right) + \frac{\omega^2}{c^2(x,y,z)}p = -\delta(x)\delta(y)\delta(z-z_s). \tag{2.25}$$

We seek a solution of the form

$$p(x,y,z) = \sum_m \Phi_m(x,y)\Psi_m(x,y,z), \tag{2.26}$$

where $\Psi_m(x,y,z)$ are the local modes. Substituting into the Helmholtz equation and applying the operator

$$\int (\cdot)\frac{\Psi_n(x,y,z)}{\rho}dz, \tag{2.27}$$

yields

$$\begin{aligned}\frac{\partial^2\Phi_n}{\partial x^2} &+ \frac{\partial^2\Phi_n}{\partial y^2} + k_{rn}^2(x,y)\Phi_n + \sum_m A_{mn}\Phi_m \\ &+ \sum_m 2B_{mn}\frac{\partial\Phi_m}{\partial x} + \sum_m 2C_{mn}\frac{\partial\Phi_m}{\partial y} = -\delta(x)\delta(y)\delta(z-z_s),\end{aligned} \tag{2.28}$$

where

$$\begin{aligned}A_{mn} &= \int\left(\frac{\partial^2}{\partial x^2}+\frac{\partial^2}{\partial y^2}\right)\Psi_m\frac{\Psi_n}{\rho}dz, \\ B_{mn} &= -B_{nm} = \int\frac{\partial\Psi_m}{\partial x}\frac{\Psi_n}{\rho}dz, \\ C_{mn} &= -C_{nm} = \int\frac{\partial\Psi_m}{\partial y}\frac{\Psi_n}{\rho}dz,\end{aligned} \tag{2.29}$$

Here we have assumed that the density $\rho(z)$ depends only on depth z. The adiabatic approximation can then be obtained by neglecting the contributions of the coupling matrices A, B and C. This yields the horizontal refraction equation

$$\frac{\partial^2\Phi_n}{\partial x^2} + \frac{\partial^2\Phi_n}{\partial y^2} + k_{rn}^2(x,y)\Phi_n = -\Psi_n(z_s)\delta(x)\delta(y). \tag{2.30}$$

Using the local normal modes, we have eliminated the z-dimension from the problem and obtained a new Helmholtz equation, but now in the lateral coordinates x and y. The effective index of refraction is given by the horizontal wavenumber $k_{rn}(x,y)$ so that every mode generates a corresponding Helmholtz equation. Such 2-D Helmholtz equations can be treated by various methods like normal modes, ray, or PE. In our study, we use ray model for its clear physics meaning.

2.2.4 Mode Filtering

To the characterize the acoustic propagation through an ocean volume and internal wave tomography, one needs to estimate the normal modes propagating at a given location. The acoustic pressure field as superposition of local modes (Eq.2.14)

$$p(r,z) = \sum_m \Phi_m(r)\Psi_m(r,z) \tag{2.31}$$

The spatial samples of the pressure field observed at vertical array of N hydrophones can be written as

$$\begin{bmatrix} p(z_1) \\ \vdots \\ p(z_N) \end{bmatrix} = \begin{bmatrix} \Psi_1(z_1) & \cdots & \Psi_M(z_1) \\ \vdots & \ddots & \vdots \\ \Psi_1(z_N) & \cdots & \Psi_M(z_N) \end{bmatrix} \begin{bmatrix} \Phi_1 \\ \vdots \\ \Phi_M \end{bmatrix} + \begin{bmatrix} n(z_1) \\ \vdots \\ n(z_N) \end{bmatrix}, \tag{2.32}$$

or in vector notation

$$\mathbf{p} = \mathbf{\Psi}\mathbf{\Phi} + \mathbf{n} \tag{2.33}$$

where $\mathbf{n}$ is the vector of observation noise at the hydrophone locations, and $z_1, \ldots, z_n$ are the depths of the hydrophones. The goal of mode filtering is to estimate the mode coefficients ($\mathbf{\Phi}$) from the observed pressure samples ($\mathbf{p}$) under the interference of unknown noise ($\mathbf{n}$).

One potential issue of hydrophone array is poor spatial sampling. At times, the number of hydrophones N is fewer than the number of propagating modes. In this scenario, Eq. 2.32 is an underdetermined least squares problem, and thus lacks a unique solution. While it is possible to find the minimum norm solution to this equation, there is no reason to believe that the modes propagating are the set giving the minimum norm for $\mathbf{\Phi}$. For this reason, it is crucial to insure that the number of hydrophones in the array exceeds the number of modes that can reasonably be expected to be observed at the array for the frequency of propagation.

In order to minimize the squared error between $\mathbf{\Psi}\mathbf{\Phi}$ and the observation $\mathbf{p}$, in this study, we use the pseudo-inverse (PI) mode filter $\mathbf{H}$ that is the pseudo-inverse of mode shape matrix $\mathbf{\Psi}$,

$$\mathbf{H} = (\mathbf{\Psi}^H\mathbf{\Psi})^{-1}\mathbf{\Psi}^H \tag{2.34}$$

2.3 Parabolic Equation

Start from the Helmholtz equation for a constant-density medium in cylindrical coordinates (r, φ, z) and for a harmonic point source of time dependence $exp(-i\omega t)$,

$$\frac{\partial^2 p}{\partial r^2} + \frac{1}{r}\frac{\partial p}{\partial r} + \frac{\partial^2 p}{\partial z^2} + k_0^2 n^2 p = 0 \tag{2.35}$$

where we have assumed azimuthal symmetry and hence no dependence on the φ-coordinate. Here $p(r, z)$ is the acoustic pressure, $k_0 = \omega/c_0$ is a reference wavenumber, and $n(r, z) = c_0/c(r, z)$ is the index of refraction. We assume the solution of Eq.2.35 to take the form

$$p(r, z) = \Psi(r, z) H_0^{(1)}(k_0 r), \tag{2.36}$$

in which $H_0^{(1)}(\cdot)$ is the Hankel function of the first kind. For $k_0 r \gg 1$, the Hankel function is replaced by its asymptotic form

$$H_0^{(1)}(k_0 r) \simeq \sqrt{\frac{2}{\pi k_0 r}} e^{i(k_0 r - \frac{\pi}{2})}. \tag{2.37}$$

Substituting the trial solution, Eq. 2.36, into the Helmholtz equation, and makeing use of the Hankel-function property, we obtain,

$$\frac{\partial^2 \Psi}{\partial r^2} + \left(\frac{2}{H_0^{(1)}(k_0 r)} \frac{\partial H_0^{(1)}(k_0 r)}{\partial r} + \frac{1}{r} \right) \frac{\partial \Psi}{\partial r} + \frac{\partial^2 \Psi}{\partial z^2} + k_0^2 (n^2 - 1)\Psi = 0. \tag{2.38}$$

Next we make the farfield assumption, $k_0 r \gg 1$, and use Eq.2.37 to obtain the simplified elliptic wave equation

$$\frac{\partial^2 \Psi}{\partial r^2} + 2ik_0 \frac{\partial \Psi}{\partial r} + \frac{\partial^2 \Psi}{\partial r} + \frac{\partial^2 \Psi}{\partial z^2} + k_0^2 (n^2 - 1)\Psi = 0. \tag{2.39}$$

Implicit in the farfield analysis is the small angle approximation, evident from the expression for the uniform ocean Green's function,

$$p = \frac{1}{[r^2 + (z - z_s)^2]^{1/2}} e^{ik_0 [r^2 + (z - z_s)^2]^{1/2}} \tag{2.40}$$

where z_s is the source depth. For small angles of propagation, $|\theta| = \frac{|z - z_s|}{r} \ll 1$, so

$$p = \frac{1}{r} e^{ik_0 \left[r + \frac{z - z_s)^2}{2r} \right]} = \frac{1}{\sqrt{r}} \Psi e^i k_0 r. \tag{2.41}$$

The corresponding form for Ψ is found to satisfy a parabolic type equation. The general form of the parabolic approximation to the wave equation simply follows then from the acknowledgment that Ψ is a slowly varying function in range and we may neglect the term $\frac{\partial^2\Psi}{\partial r^2}$. Thus, Eq. 2.39 takes the form

$$\frac{\Psi}{r} = \frac{i}{2k_0}\frac{\partial^2\Psi}{\partial z^2} + \frac{ik_0}{2}(n^2-1)\Psi. \tag{2.42}$$

We have now reduced a second order differential equation to a first order one, thereby allowing solution via a non-iterative marching algorithm. Note that we may rewrite Eq. 2.42 as

$$ik_0^{-1}\frac{\partial\Psi}{\partial r} = H_{op}\Psi = (T_{op}+U_{op})\Psi \tag{2.43}$$

where the operators

$$T_{op} = -\frac{1}{2}\left(-ik_0^{-1}\frac{\partial}{\partial z}\right)^2 = -\frac{1}{2k_0^2}\frac{\partial^2}{\partial z^2} \tag{2.44}$$

and

$$U_{op} = U(r,z,\varphi) = \frac{1}{2}(n^2-1). \tag{2.45}$$

Therelationshipbetween the values Ψ of at different ranges can now be expressed as

$$\Psi(r+\Delta r) = \Phi(r)\Psi(r) \tag{2.46}$$

To propagate the solution out in rage requires a representation of the propagator $\Phi(r)$.

2.3.1 Split-Step Fourier Transform Method

There are three common methods of computing PE solutions: (1)the split-step Fourier (PE/ SSF) method (Hardin and Tappert, 1973), (2) the implicit nite difference (IFD-PE) method (e.g., Lee and Botseas, 1982), and (3) the nite element (FEPE) method (e.g.,Collins,1988). Since the first technique is used in this study, we shall isolate our discussion to the implementation of the PE/SSF method. This is easily accomplished by approximating the propagator function by

$$\Phi(r) \approx e^{-ik_0\overline{H}_{op}(r)\Delta r} \tag{2.47}$$

where

$$\overline{H}_{op}(r) = \frac{1}{\Delta r}\int_{r}^{r+\Delta r} dr' H_{op}(r'). \tag{2.48}$$

Using a Dyson time evolution operator,

$$\Psi(r+\Delta r) = \mathbf{T}e^{-ik_0\int_r^{r+\Delta r} dr' H_{op}(r')}\Psi(r) \tag{2.49}$$

where

$$\mathbf{T}e^{-ik_0\int_r^{r+\Delta r} dr' H_{op}(r')} = 1 \quad -ik_0\int_r^{r+\Delta r} dr' H_{op}(r') - k_o^2\int_r^{r+\Delta r} dr' \int_r^{r''} dr'' H_{op}(r'')H_{op}(r') \\ +(\text{higher order terms}). \tag{2.50}$$

The first order approximation is

$$\Psi(r+\Delta r) = e^{-ik_0\int_r^{r+\Delta r} dr' H_{op}(r')}\Psi(r). \tag{2.51}$$

To evaluate $\overline{H}_{op}$ defined in Eq.2.48. Two common approximations are

$$\overline{H}_{op} = H_{op}\left(r + \frac{1}{2}\Delta r\right) \tag{2.52}$$

and simply

$$\overline{H}_{op} = H_{op}\left(r\right). \tag{2.53}$$

There are sometimes referred to as the "centered"and "end point"schemes, respectively. The interpretation of these approximations is that, over the range step r to $r+\Delta r$,the operator(hence the environment) is sampled at either the middle or the beginning of the range step. Presumably, if is small enough the differences between the solutions are negligible. We use the "centered"scheme in this study.

The operator is simply a multiplication operator in z-space and, hence, is a diagonal matrix. The operator T_{op} is not diagonal in z-space so different depth eigenfunctions are coupled. In wavenumber space, however, the corresponding operator $\hat{T_{op}}$ is diagonal. It is desirable, therefore, to separate the application of each operator, one in z-space and one in k-space. Using the Baker-Campbell-Hausdorff expansion (Bellman, 1964), we may write

$$e^{A+B} = e^A e^B e^{[A,B]+[A,[A,B]]+[B,[B,A]]+\ldots} \tag{2.54}$$

where $A = -ik_0 \Delta r T_{op}$ and $B = -ik_0 \Delta r U_{op}$. Since both T_{op} and U_{op} are small then we assume their products are of second order and negligible. Finally then, we have

$$\Phi(r) = e^{-ik_0 \Delta r T_{op}} e^{-ik_0 \Delta r U_{op}} \tag{2.55}$$

Note that this separation of H_{op} into two components, each of which is diagonal in some representation and can be applied independently of the other, is presumed by application of the SSF integration scheme. The various approximations used to separate the operator H_{op} are typically used to distinguish one type of PE/SSF model from another. Note from Eq. (1.24) that if there are no losses present (i.e., $ImT_{op} = ImU_{op} = 0$) then

$$\|\Phi(r)\| = 1, \tag{2.56}$$

and $\Phi(r)$ is a unitary operator. Therefore, the normalization condition is

$$\|\Psi(r)\| = \int_{-\infty}^{\infty} |\Psi(r,z)\|^2 dz = \text{constant}. \tag{2.57}$$

In other words, because of the formulation of the propagator, the PE/SSF scheme is conservative. There are no intrinsic losses due to the numerical scheme.

The general algorithm behind the PE/SSF implementation is then as follows. The PE field function Ψ is specified at some range r in the z-domain. A transformation is made to the k-domain followed by a multiplication of the k-space operator $e^{-ik_0 \Delta r \hat{T}_{op}}$. The result is then transformed again to the z-domain and is followed by a multiplication of the z-space operator $e^{-ik_0 \Delta r U_{op}}$. The final result is the field function at $r + \Delta r$. The FFT subroutine employed in the numerical code assumes the convention

$$\Psi(z) = \text{FFT}(\hat{\Psi}(k)) \tag{2.58}$$

and

$$\hat{\Psi}(k) = [\text{FFT}(\Psi^*(z))]^*. \tag{2.59}$$

Therefore, the PE/SSF implementation can be represented by

$$\Psi(r + \Delta r, z) = e^{-ik_0 \Delta r U_{op}(r,z)} \times \text{FFT}\{e^{-ik_0 \Delta r \hat{T}_{op}(r,k)} \times [\text{FFT}(\Psi^*(r,z))]^*\}, \tag{2.60}$$

where, in k-space,

$$\hat{T}_{op}(k) = \frac{1}{2}\left(\frac{k}{k_0}\right)^2. \tag{2.61}$$

2.3.2 Standard and Wide Angle Approximation

Previously, we have assumed the operators took the forms defined by Eqs. 2.44 and 2.45. These forms, which followed from the derivation of the parabolic equation 2.42, are commonly referred to as the standard PE or SPE forms and are only one set of a number of various operator forms. To obtain other, higher order forms, we return to the original wave equation 2.35. Still ignoring the source term and the azimuthal coupling term, we now define the pressure field as

$$p(r,z) = \frac{1}{\sqrt{r}}u(r,z) \tag{2.62}$$

The function $u(r,z)$ is identical to the pressure field in tow dimensions and the term $\frac{1}{\sqrt{r}}$ accounts for azimuthal spreading. Substituting Eq. 2.62 into the Helmholtz equation in tow dimensions yields the far-field UNCA expression

$$\frac{\partial^2 u}{\partial r^2} + \frac{\partial^2 u}{\partial z^2} + k_0^2 n^2(r,z)u = 0 \tag{2.63}$$

We introduce the operators

$$P_{op} = \frac{\partial}{\partial r} \tag{2.64}$$

and

$$Q_{op} = \left(n^2 + \frac{1}{k_0^2}\frac{\partial^2}{\partial z^2}\right)^{1/2}. \tag{2.65}$$

Eq. 2.62 then becomes

$$(P_{op}^2 + k_0^2 Q_{op}^2)u = 0 \tag{2.66}$$

which can be factored as

$$(P_{op} + ik_0 Q_{op})(P_{op} - ik_0 Q_{op})u + ik_0[p - op, Q_{op}]u = 0. \tag{2.67}$$

The commutator $[P_{op}, Q_{op}]$ is assumed negligible and is, in fact, exactly zero in layered media. Eq. 2.67 therefore represents the combination of incoming and outgoing waves. The outgoing wave satisfies

$$P_{op}u = ik_0 Q_{op}u \tag{2.68}$$

or

$$-k_0^{-1}\frac{\partial u}{\partial r} = Q_{op}u. \tag{2.69}$$

Introduce the notation

$$\epsilon = n^2 - 1 \tag{2.70}$$

and

$$\mu = \frac{1}{k_0^2}\frac{\partial^2}{\partial z^2} \tag{2.71}$$

so

$$Q_{op} = (\mu + \epsilon + 1)^{1/2} \tag{2.72}$$

The first approximation follows from the assumption that both ϵ and μ are small compared to unity. A binomial expansion yield

$$Q_{op} \approx Q_1 = \frac{1}{2}\mu + \frac{1}{2}\epsilon + 1. \tag{2.73}$$

Substitution of Eq. 2.70 and 2.71 shows that this is, within an additive constant, the standard PE operator,

$$Q_1 = Q_{SPE} = \frac{1}{2k_0^2}\frac{\partial^2}{\partial z^2} + \frac{1}{2}(n^2 - 1) + 1. \tag{2.74}$$

Interpreting the operator μ as $\frac{k^2}{k_0^2} = sin^2\theta$ indicates that the assumption $\mu \ll 1$ implies $sin^2\theta \approx \theta^2 \ll 1$, hence this is a small angle approximation. The condition $\epsilon \ll 1$is simply interpreted as assuming primarily stratified media as is typical of most ocean regions. In fact, since $\epsilon = (n^2-1) \ll 1$, we can further approximate this by $\epsilon \approx 2(n-1)$ to obtain

$$Q_2 = \frac{1}{2k_0^2}\frac{\partial^2}{\partial z^2} + (n-1) + 1 \tag{2.75}$$

Both of these approximations were first recognized by Tappert(1977) in his original S[ringer-Verlag article.

A higher order approximation introduced by Thomson and Chapman (1983) is based on an operator splitting of

$$Q_3 = Q_{WAPE} = (1+\mu)^{1/2} + [(1+\epsilon)^{1/2} - 1]. \tag{2.76}$$

Invoking the operator identity

$$(1+\mu)^{1/2} = 1 + \mu[(1+\mu)^{1/2} + 1]^{-1} \tag{2.77}$$

and formulating Eq. 2.76 in terms of T_{op} and U_{op} as

$$Q_{op} = 1 - H_{op} = 1 - (T_{op} + U_{op}) \tag{2.78}$$

leads to

$$T_{WAPE} = -\frac{1}{k_0^2}\frac{\partial^2}{\partial z^2}\left[\left(1 + \frac{1}{k_0^2}\frac{\partial^2}{\partial z^2}\right)^{1/2} + 1\right]^{-1} \tag{2.79}$$

and

$$U_{WAPE} = -(n-1). \tag{2.80}$$

In wavenumber space, we may express Eq. 2.79 as

$$\hat{T}_{WAPE}(k) = \left(\frac{k}{k_0}\right)^2\left[\left(1 - \left(\frac{k}{k_0}\right)^2\right)^{1/2} + 1\right]^{-1} = 1 - \left[1 - \left(\frac{k}{k_0}\right)^2\right]^{1/2}. \tag{2.81}$$

Note that modes with $k > k_0$ are evanescent since

$$\hat{T}_{WAPE}(k > k_0) = 1 - i\left[\left(\frac{k}{k_0}\right)^2 - 1\right]^{1/2}. \tag{2.82}$$

This is commonly referred to as the "wide angle"approximation (WAPE), and is used in this study.

2.4 A Brief introduction to Nonlinear Internal Waves (Soliton)

2.4.1 Reconstruction of 3D IW environment

A detailed, accurate 3D environment is critical in order to model the acoustic propagation in the area, and for a better understanding of the acoustical phenomena occurred during the experiment. However, limited by the equipment and experiment conditions, environmental data usually can only be gathered at sparse mooring points (relative to the massive water body). Next, we explain how we reconstruct the 3D temperature field from various sources and sensors for event 50 during SW06 experiment.

The leading front of internal wave maintains a straight line

Figure 2 shows the combined radar picture of IW at 21:30GMT and 22:00GMT from R/V Oceanus and R/V Sharp with sketched leading wave fronts (red dash line). While the internal wave fronts in general maintain relatively straight across the range (10km), it does demonstrate some curved features under close examination. It's also worth noting that within the range of R/V Oceanus's radar (lower one), and the upper half of R/V Sharp's Radar, the wave fronts are indeed pretty straight, which leads us to believe a 3-segmented line could be a better approximation for a more accurate model without too much manual sketch. Under this assumption, the interpolation on the x-y plane is done on the direction parallel to the IW fronts, i.e., perpendicular to the direction of wave propagation.

Waveform changes only slightly along fronts

Figure **??** shows the temperature records during one internal wave event (Event 50) by 8 thermistor arrays in the farm and one attached to the WHOI receiver array (VHLA). Panel (a) is the arrays roughly perpendicular to the direction of the internal wave propagating (edge "a"), panel (b) is the arrays along the propagation direction (edge "b"). (Fig. **??**) WHOI VHLA is added as a reference.

Using the temperature at 30m as an indicator of the IW waveform, Fig **??** shows the evolutions of IW waveform at two directions at the location close to the acoustic track. The lag is adjusted by aligning the edge of the data. We find the first two or three IW waves are quite stable on Edge a. Starting from wave number 4, there can have wave dissipation or wave merge. Notice the small wave inside the circle on "a" disappears after Shark VLA (SW54), or it can merge with another wave, they both are equally plausible. There are more visible variations along Edge "b" than on Edge "a". Since our interpolation/extrapolation is done on the direction of IW wave front, we expect it will match the real environment reasonably well.

Constant internal wave speed and direction

The speed and direction of the leading IW front are estimated from temperature sensor data as well as the measurements from radar images. Speed and direction are optimized with the MMSE (minimum mean square error) criteria. Consider the size of the T-farm, it is not as "local" as the other two estimation. Nevertheless, all three estimations show very similar results, and again confirmed by the radar observations. The consistence implies when the IW is passing the Shark-SW32 acoustic track, the wave package as a whole is stable in terms of both shape and moving velocity.

Table 2.1: Local velocity and direction of internal waves in event 50

Location	Moorings	IW front direction	IW speed (m/min)
Shark VLA	54,14,15,16,17	38.3022	55.6164
T-farm	4-17, 30, 31	36.8208	53.6021
Madway	32,19,20	39.5210	57.6753
R/V Sharp Radar		∼40	57.5653
R/V Oceanus Radar		∼40	55.1065

2.4.2 Water temperature extrapolation

The water temperature data are collected by the thermistor string moorings at SW54 and SW32. Unfortunately, the surface sensor on SW32 lost during the experiment, and the next one is located at 15 meter down, thus some form of temperature extrapolation is necessary. 15 meter is the up bound of the fast-changing thermocline layer, which causes linear extrapolation to give unrealistic results water temperature can be as hot as $40°C$ at surface. Help comes from a single pressure-temperature sensor attached to the transducer J15.

On Aug. 17th and 18th, J15 were deployed and recovered twice, during which the TD sensor generated 4 temperature profiles shown in Fig. **??**. The top layer of water is very well mixed, and the depth of it is about 15m. The highest water

temperature is about 25C. Based on this observation, the water temperature extrapolation/interpolation is performed for depth >15m, for the water above 15m, we assume the it is well mixed, thus use the temperature measured at the top sensor(15m).

2.4.3 Reconstruct a 3D temperature field

Based on the estimated IW speed and direction, we can reconstruct a 3D temperature field. Figure 6 shows the reconstructed temperature field at various depths. The field is plotted in a new coordinate system. Imaging a coordinate system travel with the internal wave package, the y-axis is the vector from SW54 to SW32, and the direction of x-axis perpendicular to y-axis, and its length is the distance the IW traveled since 19:30, Aug 17th. A sketch of this coordinate system and its position relative to Earth system at 21:30 is draw in figure 1. The gray box in the middle is the area we try to reconstruct, and a few red lines represent the internal wave front.

The temperature fields at different depths are shown in Fig. 6. The track of Shark VLA during m1 m5 transmission periods in the new system is marked as white lines at the bottom, SW32's as black and R/V Sharp's as blue. With different IW speed and direction, different temperature field can be constructed. The mean estimated IW speed (54.4293 m/min) and direction (51.0884 degree w.r.t. North) were used in figure 6.

Chapter 3

SHALLOW WATER 2006 EXPERIMENT

In 2006, from mid-July to mid-September, a large, multi-disciplinary, multi-institution experiment named SW06 was conducted in the New Jersey coast. Part of its goal is to further the understanding of the affects of the nonlinear internal waves on the acoustic propagation in shallow water.

3.1 Experiment site and environment moorings

The SW06 experiment site is approximately 100 miles east of the New Jersey coast (Fig. 3.1), which is known to generate internal waves during summer time and has been a research testbed for many other experiments before (e.g., SWARM 95). To assess the combined acoustic and oceanographic relationship between the acoustic wave propagation and the internal waves, a total of 62 acoustics and oceanographic moorings were deployed in a 'T' geometry to create an along-shelf path along the 80 meter isobath and an across-shelf path starting at 600 meters depth and going shoreward to a depth of 60 meters.

A cluster of moorings was placed at the intersection of the two paths to create a dense sensor-populated area to measure 3-dimensional physical oceanography. Environmental moorings were deployed along both along-shelf and across-shelf paths to measure the physical oceanography long those paths. Moorings with acoustic sources were placed at the outer ends of the 'T' to propagate various signals along these paths. Five single hydrophone receivers (SHRU) were positioned on the across shelf path and a vertical and horizontal hydrophone array (VLA/HLA) was positioned close to the intersection of the 'T' to get large antenna signal receptions from all the acoustics assets that were used during SW06.

There were in total 34 environmental moorings deployed during SW06 experiment to access the physical oceanography of the area. Each of the acoustic moorings (source and receiver) was equipped with thermistors at various depths to help recreate the acoustic channel. Close to the center of the "T" shape mooring layout, a thermistor farm consisting of 16 arrays spacing logarithmically from 0.5 km to 3 km to record the internal waves at different scales.

Out of 34 environmental moorings, 6 of them were also equipped with Acoustic Doppler Current Profiler(ADCP) to measure the current velocity at the location. The ADCP package including a temperature, conductivity, pressure sensor was locate about 7 meters above the sea floor. The space of measuring bins was set at 1m. The sampling interval of ADCP is 30 seconds and capable of solving internal wave passage but not the fine scale of surface waves. Figure 3.2 shows the current data record by ADCP at mooring SW32 during event 50 in SW06 experiment and the temperature data at the same location. It demonstrates the clear correspondence between the direction and the depth profile of the subsurface current.

3.2 Acoustic moorings

3.2.1 Sources

During SW06, several acoustic sources were used to transmit sound while environmental data were collected simultaneously[21]. Here we discuss the acoustic data from a pair of acoustic sources.

1. Fixed source (NRL300) at mooring SW45

   The source was located 72 m below the sea surface and 10.5 m above the sea floor at $39^o10.957'$ N, $72^o56.575'$ W, and transmitted 2.0489 second Linear Frequency Modulating (LFM) signals from 270 to 330 Hz every 4 seconds. Transmissions continued for 7.5 minutes and then repeated every half hour.

2. Moving source J15 towed by R/V Sharp

   There were towed source aboard R/V Sharp of University of Delaware transmitting from 16th Aug. to 20th Aug. Three G34 sources were positioned at depth from 10-30 meters, and one J15 source at approximately 40 meters. The signal transmitted from J15 source (the moving source) will be used in this research.

Table 3.1: Transmission during Ev50 from fixed source (NRL300) & moving source (J15)

Transmission	Time(GMT)	Source
1	20:30-20:37	NRL300
2	21:00-21:07	NRL300
3	21:11-21:26	J15/R.V. Sharp
4	21:30-21:37	NRL300
5	21:41-21:46	J15/R.V. Sharp
6	22:00-22:07	NRL300
7	22:11-22:26	J15/R.V. Sharp
8	22:30-22:37	NRL300
9	22:41-22:56	J15/R.V. Sharp
10	23:00-23:07	NRL300
11	23:11-23:16	J15/R.V. Sharp
12	23:30-23:37	NRL300

The signal type is Linear Frequency Modulating (LFM) from 100 to 400 Hz every 10 seconds. Transmission continued for 15 minutes in the quiet window of NRL300 source and then repeated every half hour.

Table 3.1 lists all the transmissions during the internal wave event 50 (explained later) from both the fixed source and the moving source.

3.2.2 Receiver array

A vertical and horizontal receiver array (the "Shark VHLA") on mooring SW54 was located at $39^o01.252'$ N, $73^o02.983'$ W, about 20.2 km south of the NRL source. The vertical part ('VLA') of the receiver array consisted of 16 hydrophones with 3.5 m spacing and was positioned in the water column from 13.5 m to 77.75 m below the surface. The horizontal part ('HLA') of the array consisted of 32 hydrophones on the seafloor with spacing of 15 m, providing 478 m of horizontal aperture. The sampling rate of the array was 9765.625 Hz. The acoustic track and the locations of the source and receiver as well as the horizontal and vertical array configurations are shown in Fig. 1. The water depth along the acoustic track was about 80 m.

Figure 3.6 shows the fixed source(NRL300), the receiver array(Shark VHLA) and the semi-circular track of R/V Sharp, who was towing the moving source J15 in

the internal wave event 50. Zone 1-5 marks the location of J15 in the transmission windows of J15 in event 50.

3.3 Internal wave observation

The SW06 site is known for generating internal waves. Figure 3.3 shows a radar image of the ocean taken by Canadian satellite RADASAT over the experimental site near the edge of the continental shelf. The picture shows about 8-10 groups of internal wave packages running from south-east to north-west diagonally, with the wave fronts approximately parallel to the edge of the continental shelf. The wave packages are generate at the shelf break (about 200 m in depth), propagate towards the coast and dissipated at about 50 m. The separation between individual wave packages are approximately 10-20 km. Notice the sever curvature caused by the Hudson Canyon and numerous collisions between wave packages.

Although bearing the word "internal" in its name, internal wave can be visible to a electromagnetic radiation recording device such as a camera or a radar. Together with other factors like wind, surface waves, The subsurface current caused by internal waves changes the equilibrium surface and generates an alternating region of rougher or smother than the average surface scattering the electromagnetic wave differently[7][15]. The image captured by radar or optical device mirrors the current under the surface. During SW06, two research vessels, R/V Oceanus from Woods Hole Oceanography Institution (WHOI) and R/V Sharp from University of Delaware were constantly recording the surface expression of internal waves.

The passing of internal waves can also be seen by other environmental sensors. Figure 3.4 shows the depth of 18°C thermocline recorded on WHOI VLA (SW54). Before the internal wave, the thermocline is at about 16m, the first soliton wave pushs the thermocline down the 35m, and the later solitons even push further down towards the bottom. There are about 9 distinguishable soliton waves, followed by a long, slow-decreasing tail, the thermocline didn't return to 16m until 6:00 next day - the total duration of internal wave is about 8 hours.

Using an onboard radar of R/V Sharp of University of Delaware, 60 internal wave event were recorded when the surface expressions were visible on the screen during the period of 21 days with various strength and direction. Fig.3.5 shows their angular distribution. The direction spreads from 280-330 degree with respect to north(0°), with the strongest peak at about 320 degrees. The propagation paths and the their day rates vary considerably from one wave to another. Lynch *et al* [14] reported a similar results by studying satellite imagery. In this study, we focus on a particular internal wave event on August 17, 2006, for which a complete set of acoustic and environmental data were collected simultaneously. In addition, the internal wave surface signatures were captured continuously by the on-board radars of two research vessels prior to the arrival of, and during the passing of, the internal wave packet over the acoustic track.

3.3.1 Internal wave event 50

On August 17, 2006, at about 18:00 GMT, the R/V Sharp from the University of Delaware was located at $38^o59.262'$ N, $72^o57.492'$ W and the R/V Oceanus from the Woods Hole Oceanographic Institution (WHOI) was located at $38^o57.426'$ N, $72^o56.676'$ W. Both platforms observed the origination of the internal wave packet near the shelf break. This event was named Event 50 on R/V Sharp and Rosey on R/V Oceanus.

Figure 3.6 show the track of each vessel following this event from 18:00 GMT on August 17 to 02:00 GMT on August 18, 2006. The R/V Sharp's track was semi circular, centered at the WHOI vertical and horizontal line array (Shark VHLA) with the ship being positioned on the trough of the leading internal wave front and moving with the advancing front. The R/V Oceanus followed the same internal wave packet from its initial location, while keeping a watch on the advancing wave front. Reversals in the track of R/V Oceanus indicate where the wave packet was crossed, and during these periods, intensive profiling of temperature, density, turbulence and sound velocity was conducted.

The two ships observed different parts of the internal wave front, thus providing a large spatial coverage. The surface signatures of the internal waves were digitally

recorded by on-board ship radar images every 30 seconds. Combined radar images from the two vessels, each about 11.1 km in diameter, covered the receiver and about two thirds of the acoustic track.

The direction and speed of the internal wave packet in event 50 can be estimated by measuring the time difference when the leading front arrives at different thermistor arrays, or by averaging the direct measurement from the ship radars. Table 3.2 lists the speed and direction estimations by these two methods. A little discrepancy is to be expected.

Table 3.2: Direction and speed of the internal wave packet in event 50

Data source	IW speed	IW direction
Thermistor arrays	0.55m/s	325°
Ship radar	0.60m/s	330°

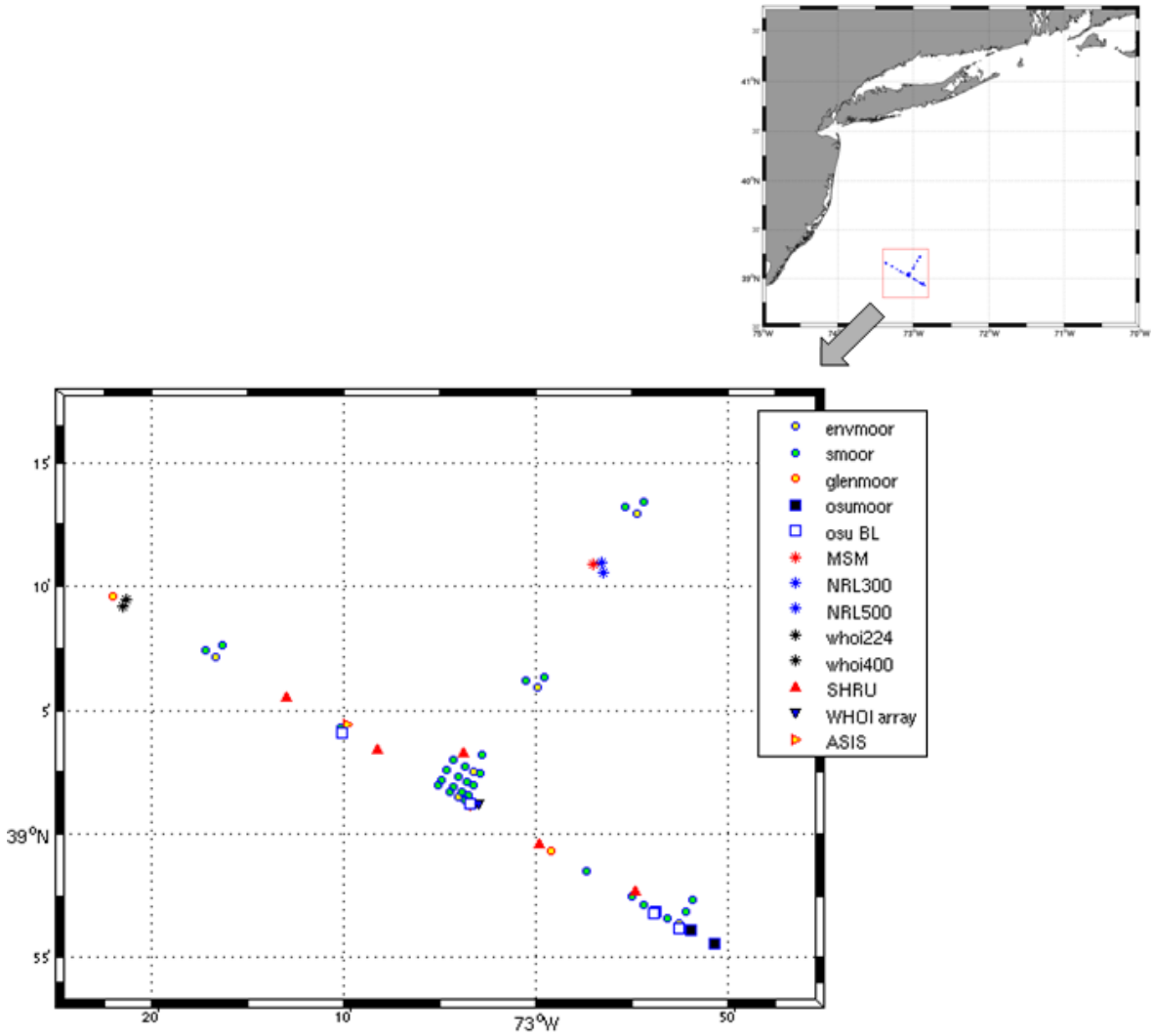

Figure 3.1: Map of SW06 experiment site and the locations of the environment and acoustic moorings

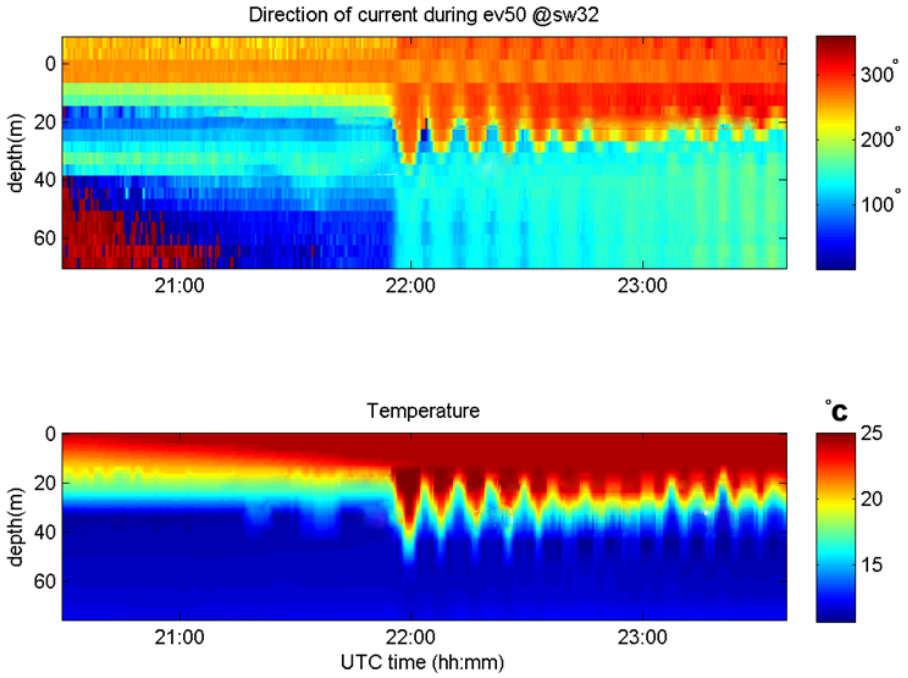

Figure 3.2: Current data record by ADCP at mooring SW32 during event 50 in SW06 experiment (upper panel) and temperature data at the same location.

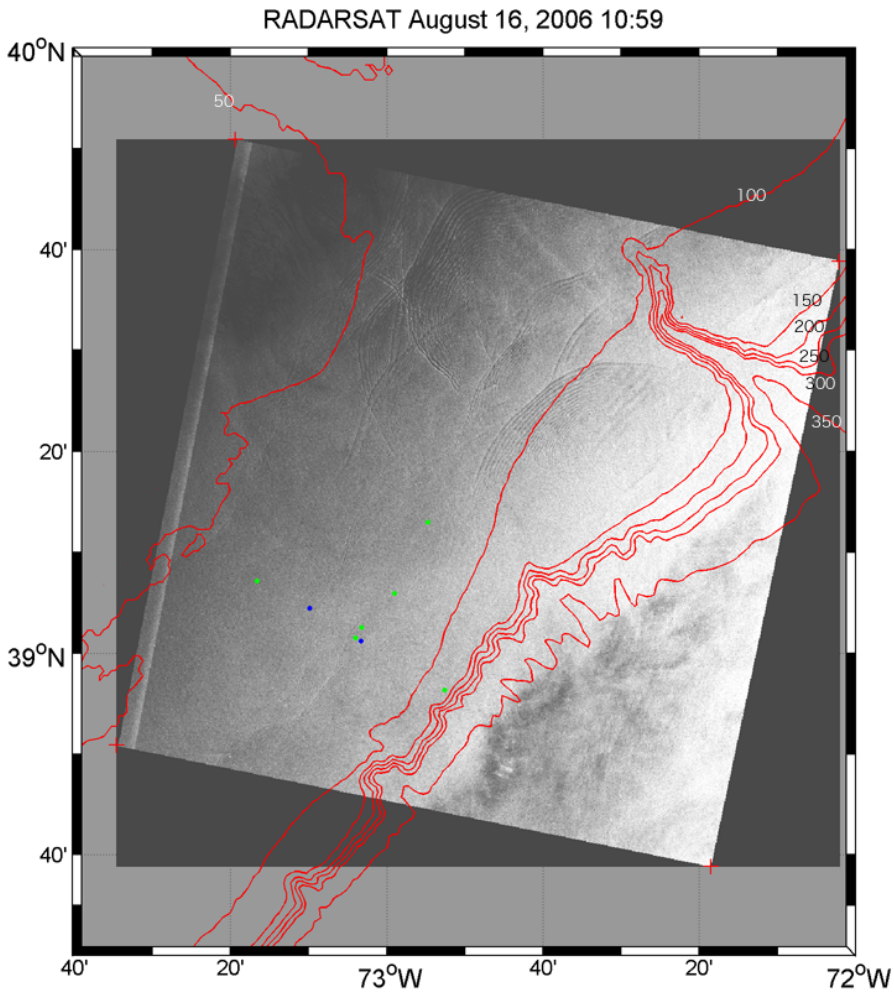

Figure 3.3: Image of SW06 experiment site taken by the Canadian RADARSAT satellite on 16 August, 2006.

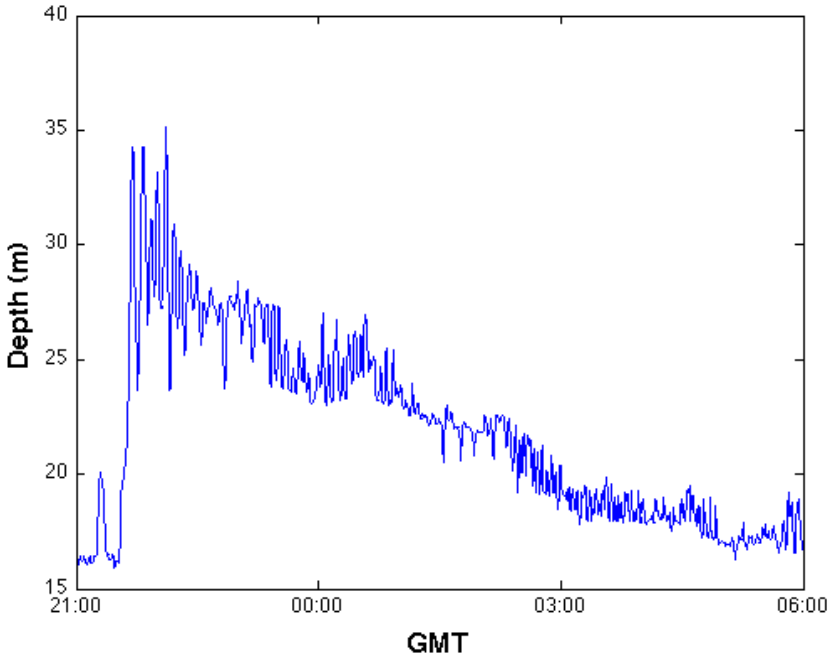

Figure 3.4: Depth of 18^oC degree thermocline on Aug. 17, 2006, recorded on WHOI Sharp VLA (SW54)

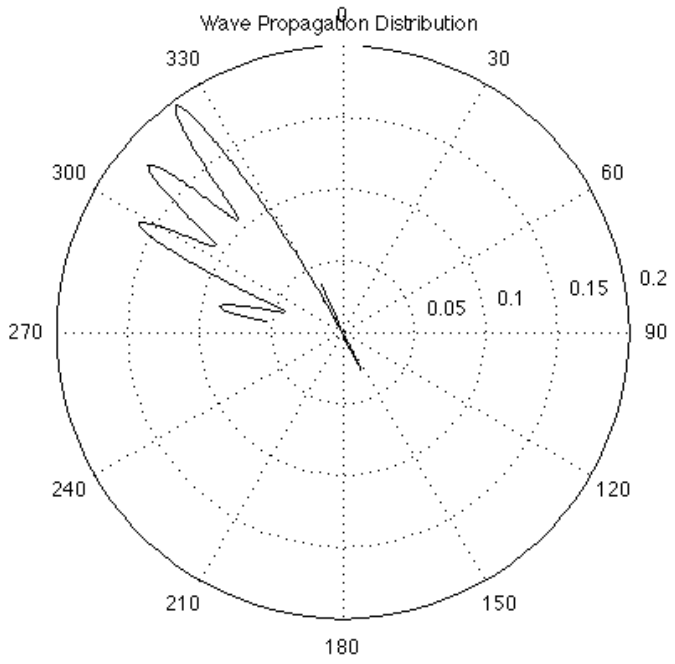

Figure 3.5: Angular distribution of the direction of the internal wave recored during SW06.

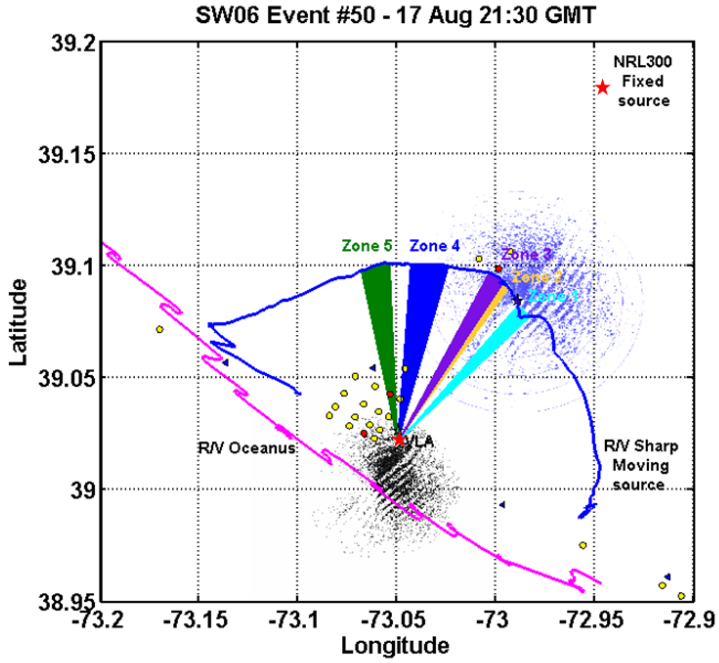

Figure 3.6: Diagram showing the fixed acoustic source(NRL300), receiver array (Shark VHLA) and the semi-circular track of R/V Sharp the IW event 50. Zone 1 5 represent the location of J15 in the time periods when it was transmitting in event 50.

Chapter 4

ACOUSTIC OBSERVATIONS IN EVENT 50

Our goal in SW06 experiment is specifically to examine the relationship between internal wave and acoustic wave propagation. In particular we seek to understand the acoustic wave propagation mechanisms governed by the direction of the acoustic track relation to the internal wave front.

The propagation of acoustic signals is strongly related to the ocean's physical attributes with various time scales and frequencies, such as surface waves, internal waves, tides, currents. Given the conditions of SW06 experiment (acoustic signal transmission interval = 4sec, acoustic listening window = 3hr), we concentrated ourselves to the variation caused by the internal wave activities.

Quantities will be used in the following sections are:

1. Integrated acoustic intensity

   When the propagation and scattering conditions change in the water, the received acoustic intensity changes at the same time. We calculate the intensity of the signal arrivals integrated over a pulse length $\Delta\tau$ at a given depth z as

$$I(z,T) = \frac{1}{\rho c} \int_{\tau}^{\tau+\Delta\tau} p^2(z,T,t)\, dt \tag{4.1}$$

   where p is acoustic pressure,ρ is water density, and c is sound speed. And the total intensity integrated over the depth H is

$$I(T) = \int_{0}^{H} I(z,T) dz. \tag{4.2}$$

   The time integration at a single hydrophone is to show the attenuation and scattering through the medium, both horizontally and vertically, thus carries much information about the environment, in our case the internal wave packet.

On the other hand, the depth integration over the entire water column gives the energy flux through a particular vertical slice, which is of great interests here because the change of this parameter shows how much energy is transported through the horizontal acoustic mechanisms like refraction and reflection, under the condition of constant attenuation and scattering. We will examine the mean and standard deviations of the intensity at different stages during the passing of the internal wave packet.

2. arrival time and pulse spread

   The passing of the internal waves also has an effect at the arrival time (sometimes called the "wander" in literature) and pulse spread. We define the arrival time as the arrival time of the centroid of the acoustic pulse.

$$t_c = \frac{\int_{t_1}^{t_0} I(t)tdt}{\int_{t_1}^{t_0} I(t)dt} \tag{4.3}$$

   in which, t_c is the arrival time, t_0 and t_1 are the beginning and the end time of a received pulse, $I(t)$ is the acoustic intensity. (All the time variables in the equation above t_c,t_0,t_1 are started from a common but arbitrary zero point, due to the lack of a absolute clock between the receiver and the transmitter.) There are other definitions of the "arrival time" in the literature, e.g. the leading edge arrival time and the peak arrival time. We choose the centroid definition due to its insensitivity to the swift changes of the arrival pulse structure, which are quite common in SW06 experiment.

   The pulse spread is the duration of the acoustic pulse after matched filter. We consider the received acoustic signal is part of the pulse, if its level is 10 times bigger than the mean noise level, which is measured during the quiet time between transmissions.

4.1 Transmission from the fixed source(NRL 300Hz)

This part of the experiment can be roughly divided into four phases based on the distance between the acoustic path and the IW packet.

4.1.1 Phase I: 20:30-20:37GMT & 21:00-21:07GMT

Phase I is the quiescent time before the internal wave packet arrive at the source-receiver track and have little impact on the acoustic propagation. Figure 4.4 show the interpolated radar images at the beginning of the transmissions (20:30GMT). The leading front of the IW packet is at about 6 kilometers away at the closest point (SHARK

VLA) of the acoustic track. Integrated intensity of the received signals (squared matched filter output) on Shark VHLA are plotted in Fig. 4.5 for the transmission from 20:30 through 20:37GMT, where, the top and bottom panel shows the received signal on VLA and HLA and the middle palel shows the depth integrated signal intensity. The VLA panel shows a stable 3-stripe pattern, which can be attributed to the strong 2nd and 3rd modes (Fig. 4.6). The acoustic energy has a clear concentration at the lower part of the receiver array, below the thermocline (15m from the surface). The fluctuation of the depth integrated intensity is less than 2.5dB. The results of the next transmission (21:00-21:07GMT) are similar to what we observed here (Fig. 4.8, 4.9 and 4.10). The signals received during these two transmission help us establish the base scenarios to compare with the acoustic propagation in the later phases.

4.1.2 Phase II: 21:30-21:37GMT

Phase II is of particular interests here because from the internal wave map (Fig. 4.13), the leading front of the IW packet is still at about 1km away from the Shark VLA at the end of the transmission session (21:37GMT), but its impact on the acoustic propagation can be seen on the received signal on the Shark array. The impact, which is similar to the optical Lloyd mirror effect, will be further analyzed in chapter 5. Figure 4.13 shows the radar image and the interpolated temperature field at 21:30GMT. The received signal on Shark VLA and HLA shows a clear contrast between the first and second halves of this transmission. During the first half, the signal continues the steady characteristic from phase I. When the IW moves closer in the second half, the acoustic signal changes to a oscillating two-strip pattern.

4.1.3 Phase III: 22:00-22:07GMT, 22:30-22:37GMT, 23:00-23:07GMT & 23:30-23:37GMT

Phase III is when the acoustic signal propagates through the body of the IW packet. The position of the source and receiver in internal waves can cause fluctuations (¿6dB) in the received signal by mechanisms like refraction, focusing and defocusing

depending on the relative positions of the source and receiver in the internal waves. At 22:00GMT, the source is about three kilometers from the leading wave front, but the Shark VlA is at the trough between the second and the third waves, and about half of the acoustic track is directly interacting with the IW packet.

4.1.4 Phase IV: after 23:30GMT

This is the afterward phase when the entire IW packet has well passed acoustic track and has no noticeable acoustical impact. The acoustic path is at the middle of the ISW package, where the wavelength is shorter than the leading fronts. Two focusing events are observed with 15dB variations on total intensity. Mode 1 and 2 show more fluctuation than mode 3, 4 and 5. On HLA, regular slopes are shown, sometimes not consistent with the signals on VLA.

4.1.5 23:00GMT-23:07GMT

The acoustic path now is at the coverage of R/V Sharp's radar, and escapes from R/V Oceanouse's radar. From the temperature plot, the acoustic path is still affected by the ISW package. Tow focusing events are shown with about 15dB fluctuation.

4.1.6 23:30GMT-23:37GMT

No radar image, but the temperature plots shows the acoustic path is still under the influence of ISW. Tow focusing events are recorded on HLA with fluctuation about 15dB.

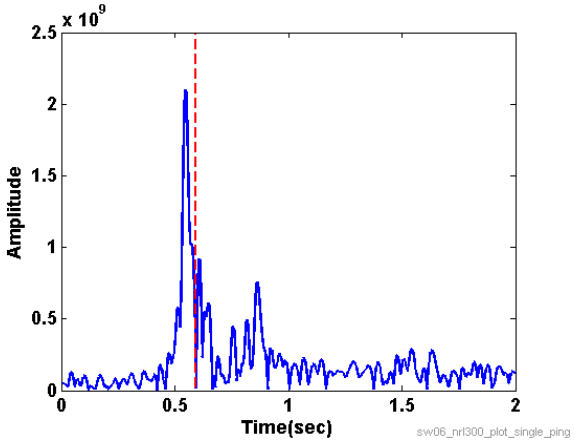

Figure 4.1: Matched filter output of received chirp signal on VLA Shark at GMT 20:30:04, Aug 16th. The red dash line shows the centroid arrival time, which is different than the peak arrival time.

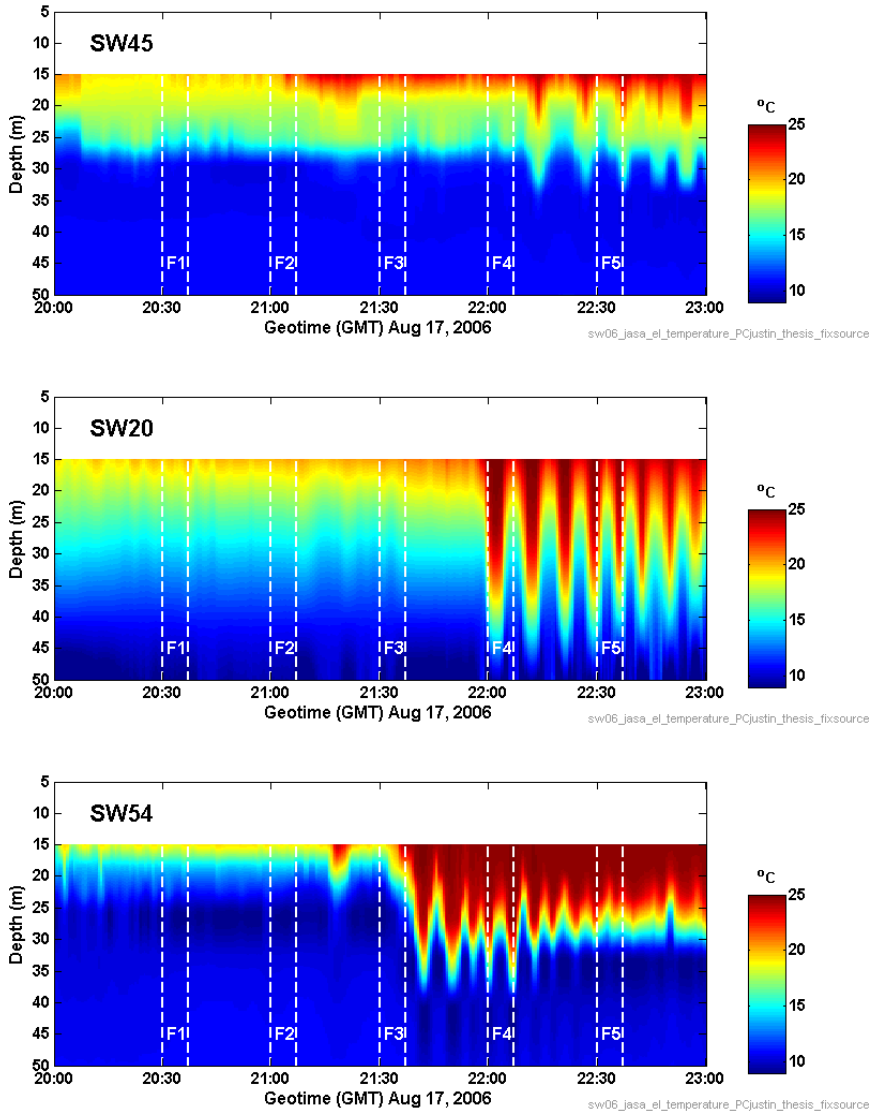

Figure 4.2: Temperature record at three location along the fixed sourc-receiver track. Panel (a), (b) and (c) show the temperature at the NRL300 source (SW45), the midpoint (SW20) and the Shark VLA (SW54).

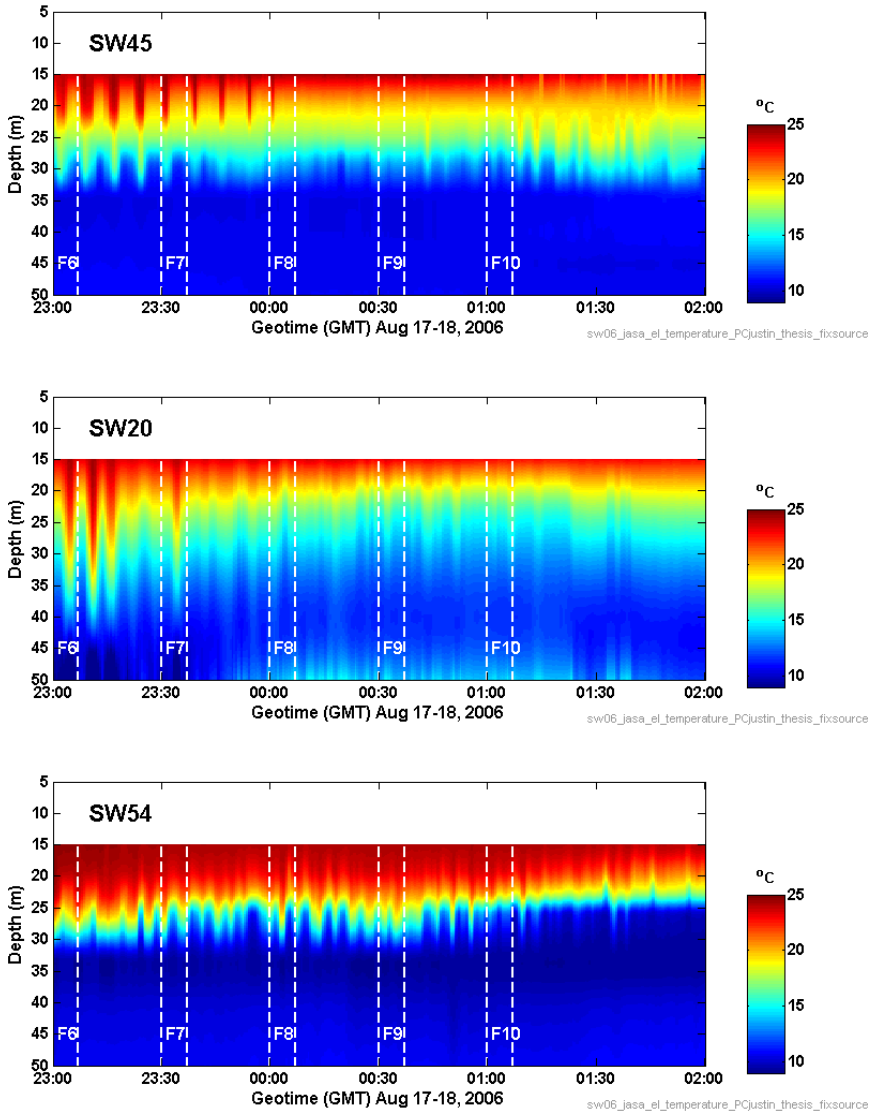

Figure 4.3: Temperature record at three location along the fixed sourc-receiver track. Panel (a), (b) and (c) show the temperature at the NRL300 source (SW45), the midpoint (SW20) and the Shark VLA (SW54).

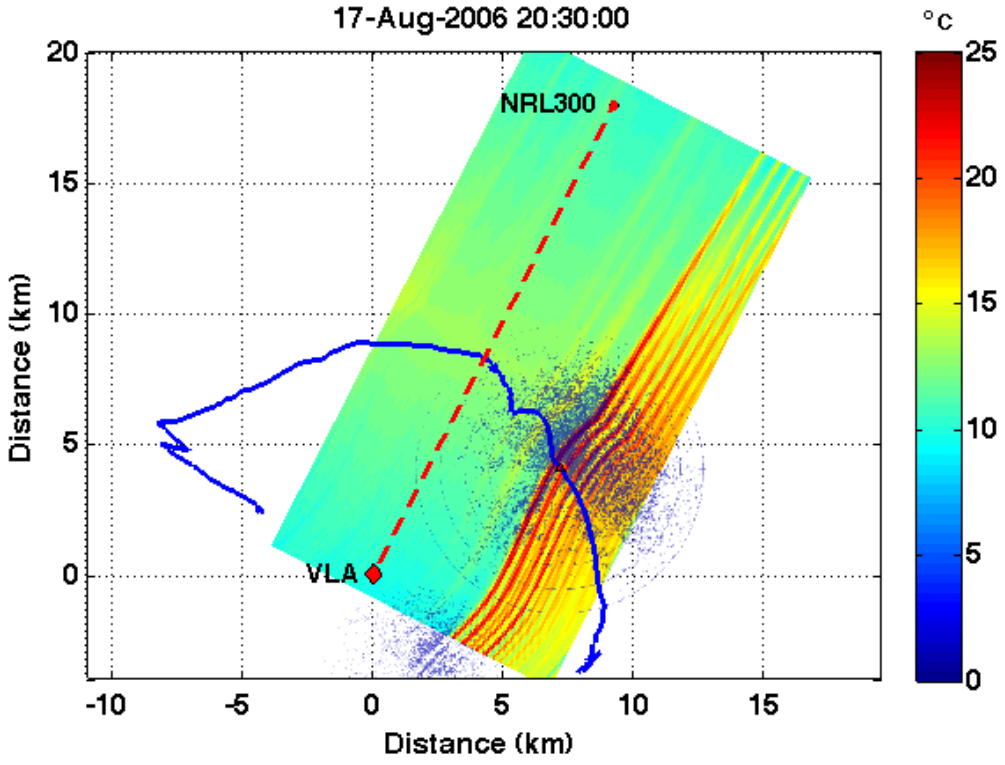

Figure 4.4: Interpolated internal wave field at 20:30GMT, Aug. 17, water depth = 20m. (Refer to section 3.4 for detailed interpolation method)

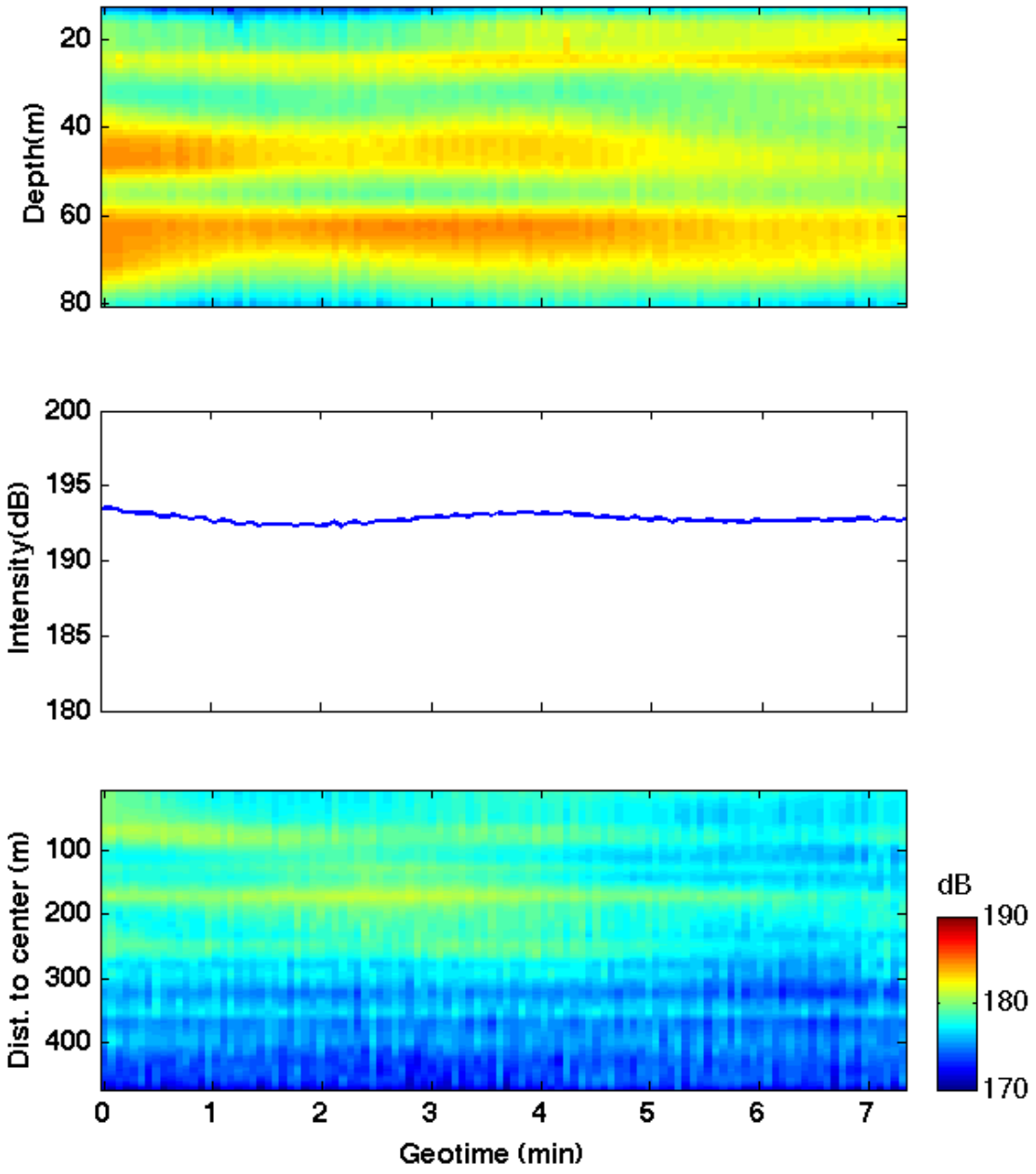

Figure 4.5: Received signal on Shark VLA (top), HLA (bottom) and signal intensity (middle) from Aug.17 20:30GMT to 20:37GMT

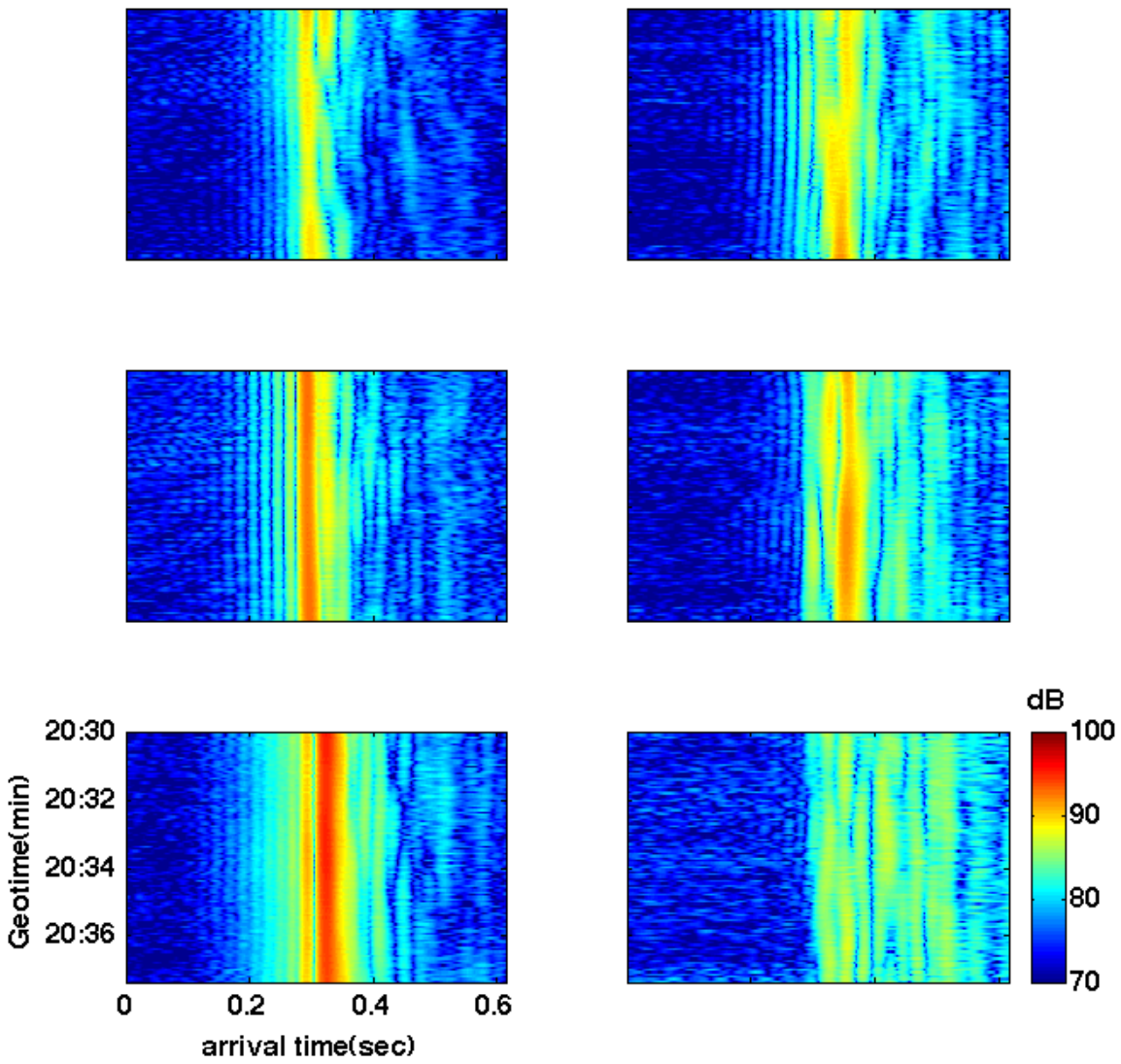

Figure 4.6: Mode decomposition of received signal on Shark VLA. Left column: mode 1-3, right column: mode 4-6

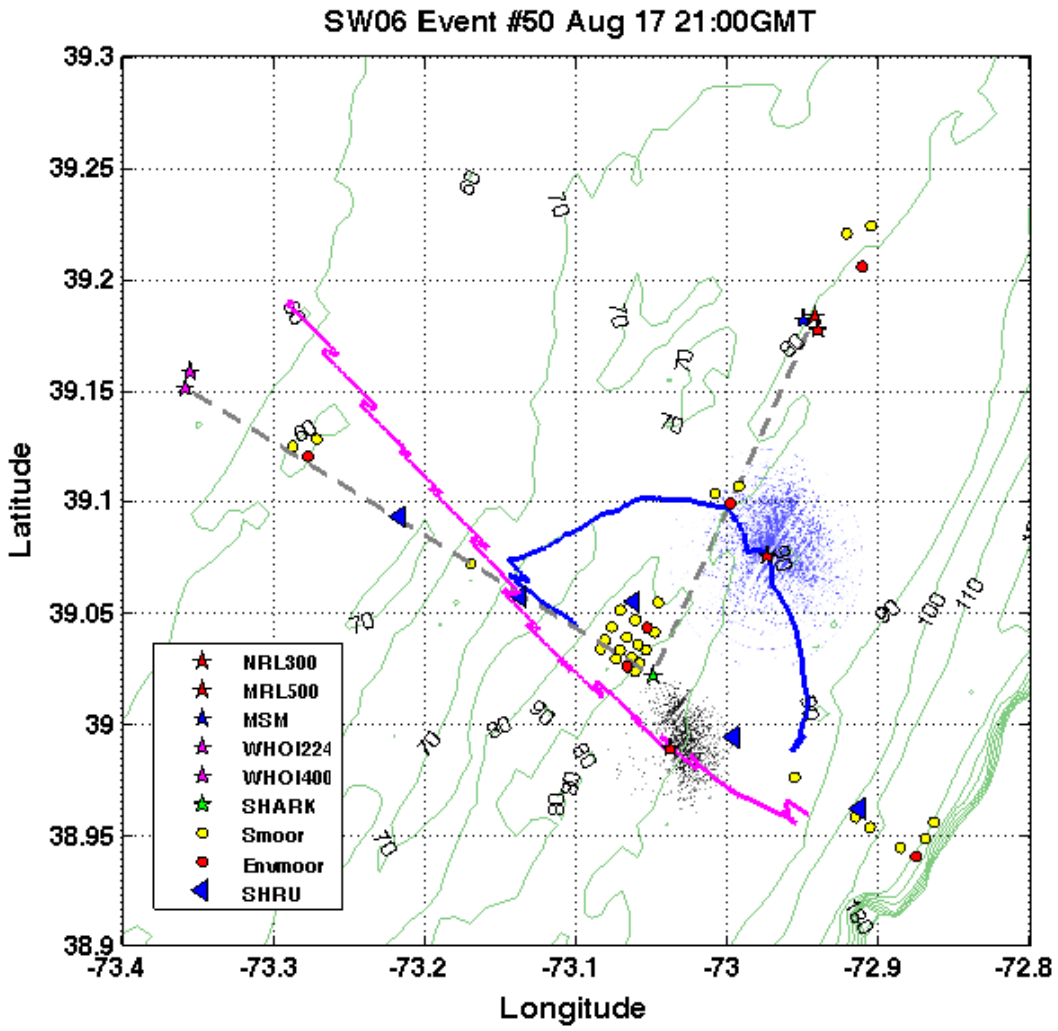

Figure 4.7: Surface expression of internal wave package at 21:00GMT, Aug. 17, recorded by R/V Sharp and R/V Oceanus. Blue and red lines indicate their movements, respectively. (Blue: R/V Sharp's, red: R/V Oceanus'

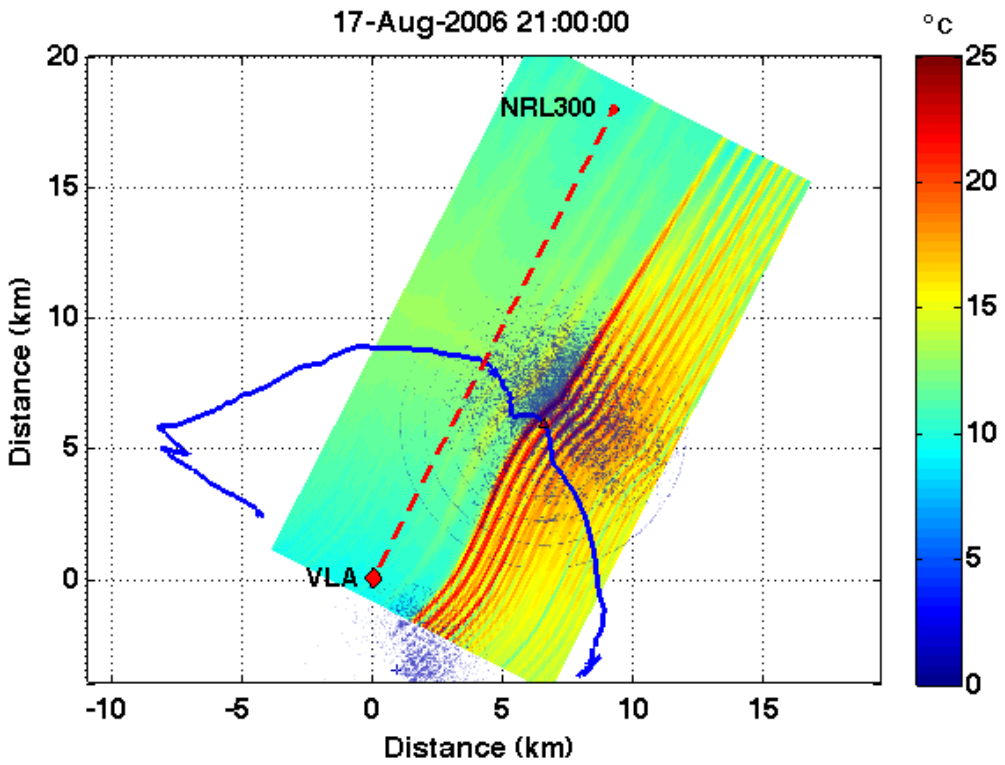

Figure 4.8: Interpolated internal wave field at 21:00GMT, Aug. 17, water depth = 20m. (Refer to section 3.4 for detailed interpolation method)

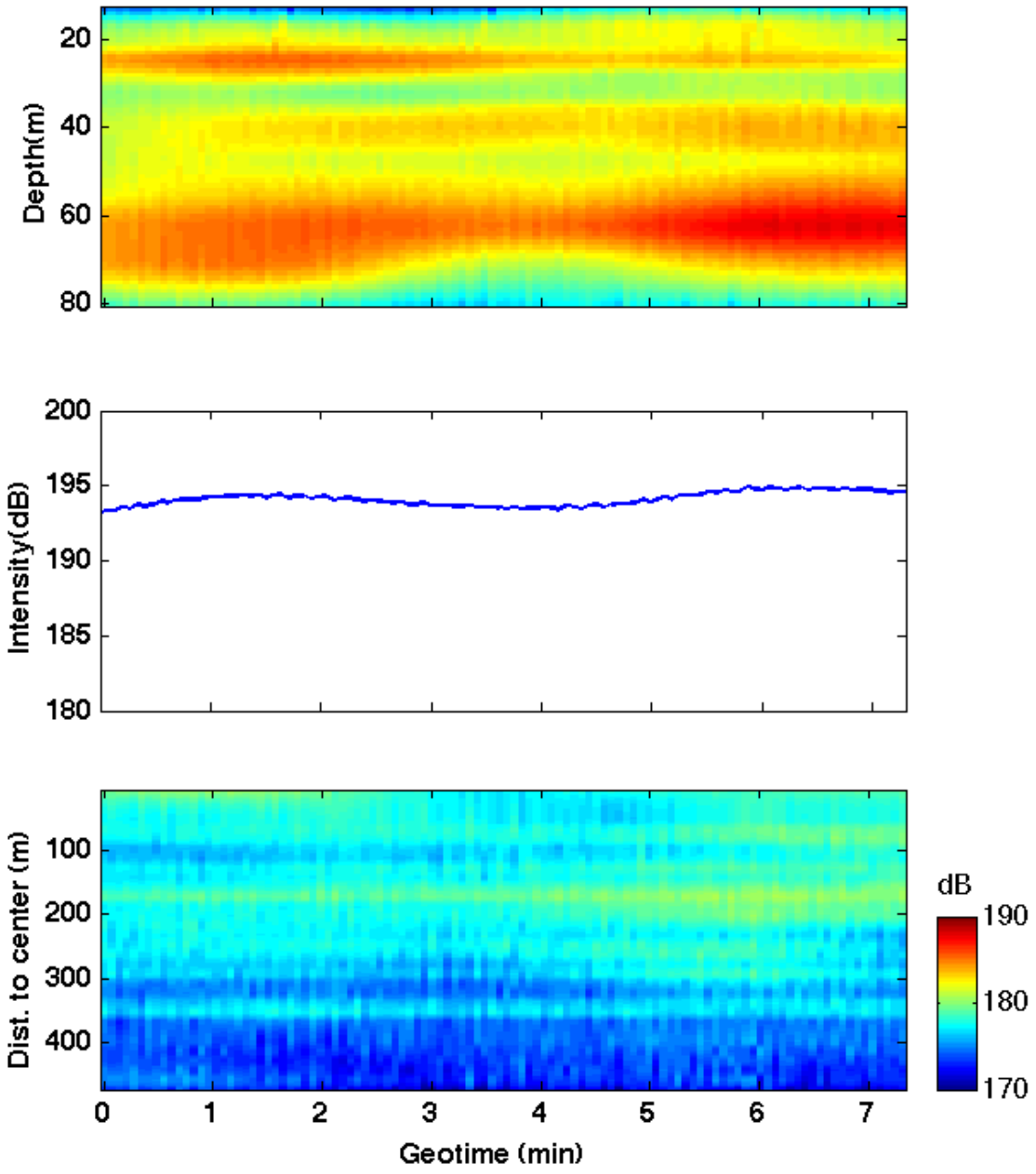

Figure 4.9: Received signal on Shark VLA (top), HLA (bottom) and signal intensity (middle) from Aug.17 21:00GMT to 21:07GMT

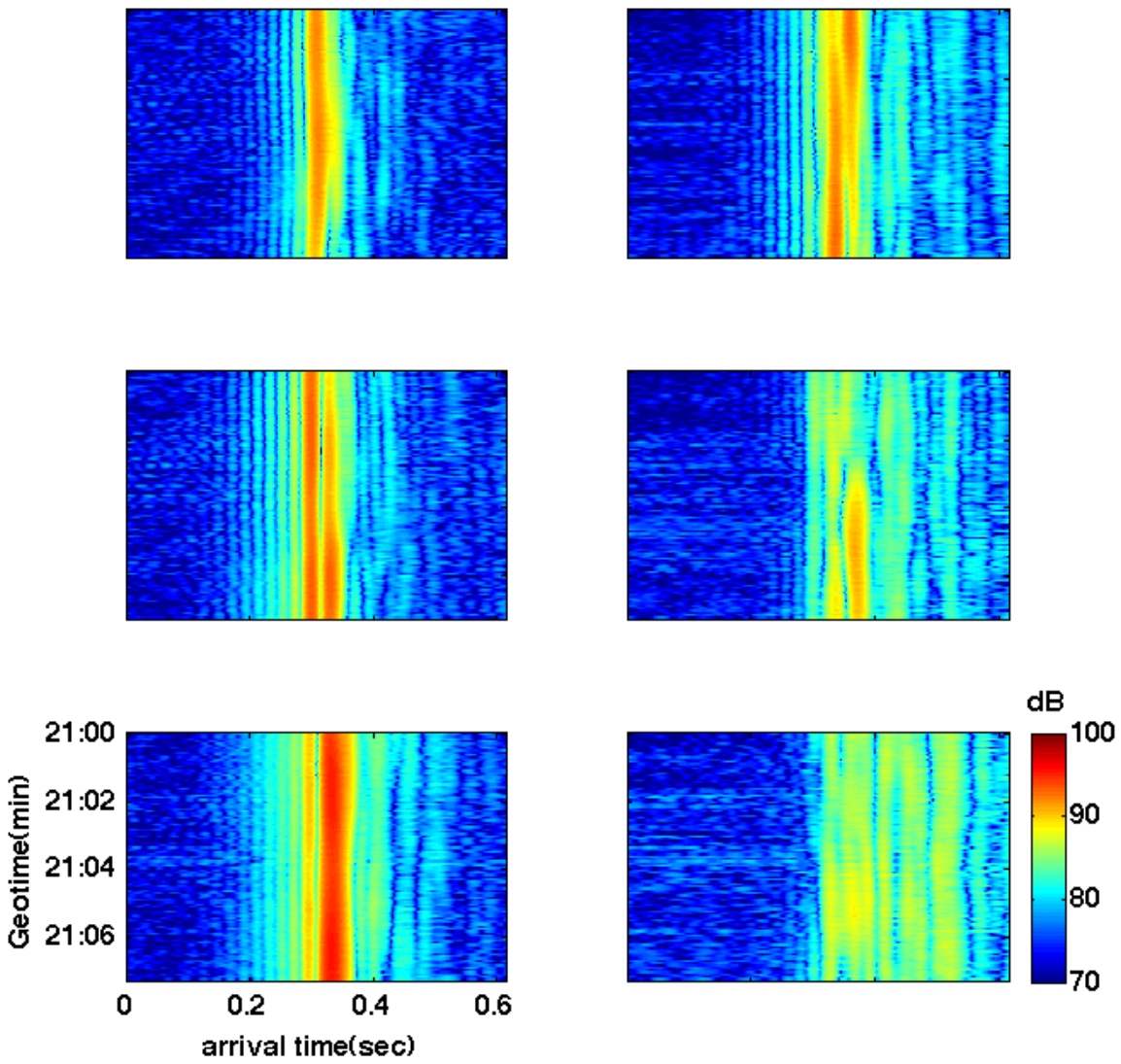

Figure 4.10: Mode decomposition of received signal on Shark VLA. Left column: mode 1-3, right column: mode 4-6

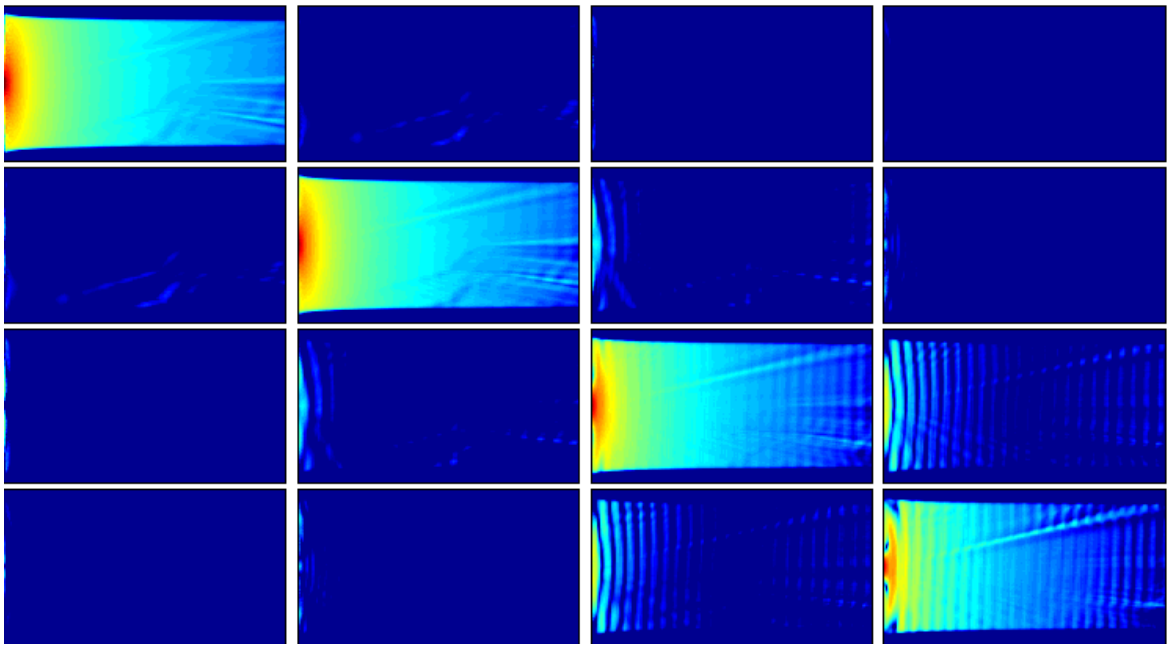

Figure 4.11: Mode coupling between mode 1 4

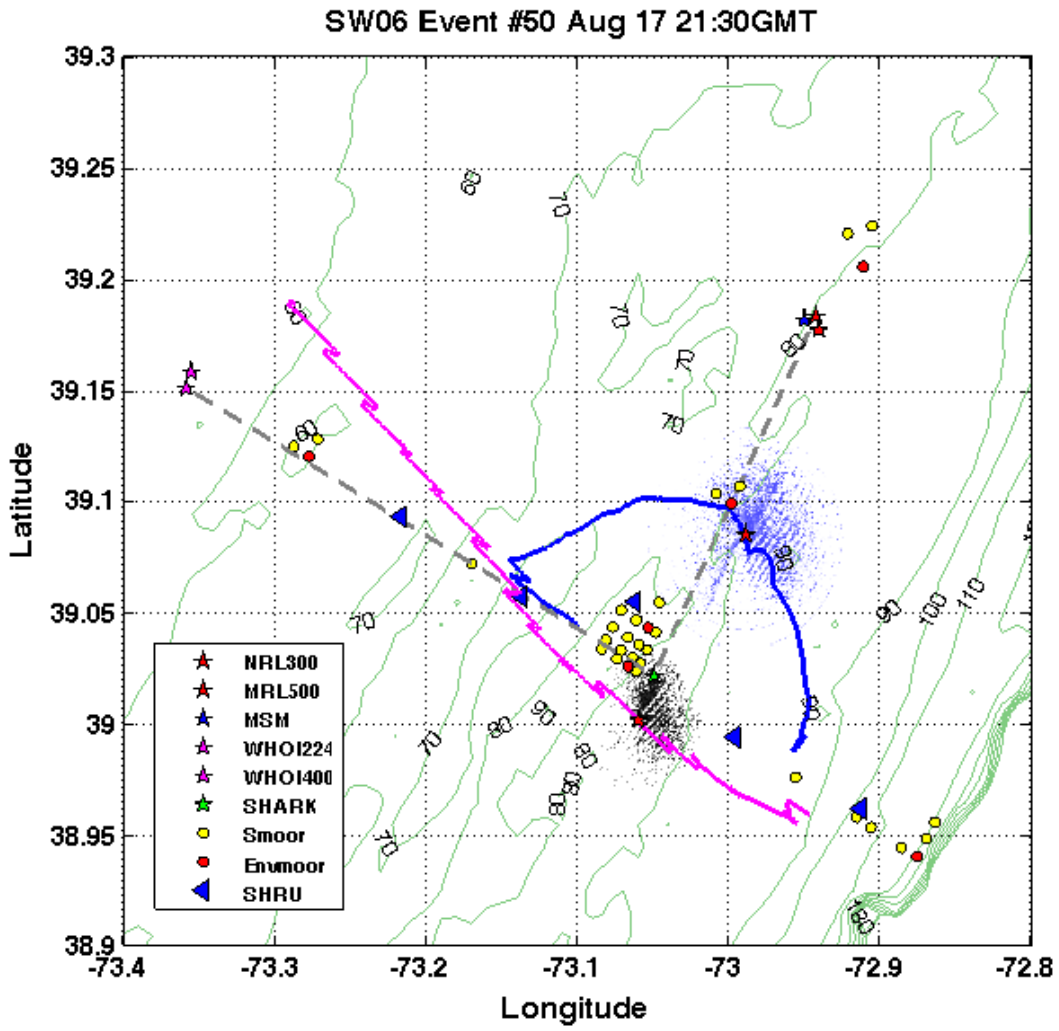

Figure 4.12: Surface expression of internal wave package at 21:30GMT, Aug. 17, recorded by R/V Sharp and R/V Oceanus. Blue and red lines indicate their movements, respectively. (Blue: R/V Sharp's, red: R/V Oceanus'

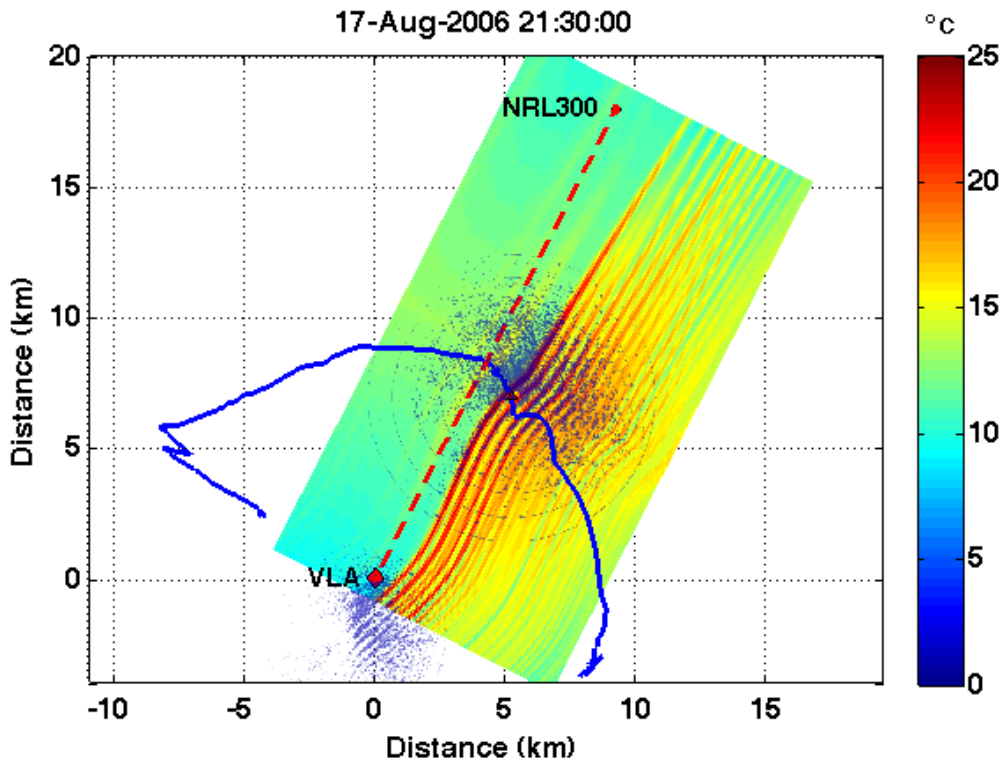

Figure 4.13: Interpolated internal wave field at 21:30GMT, Aug. 17, water depth = 20m. (Refer to section 3.4 for detailed interpolation method)

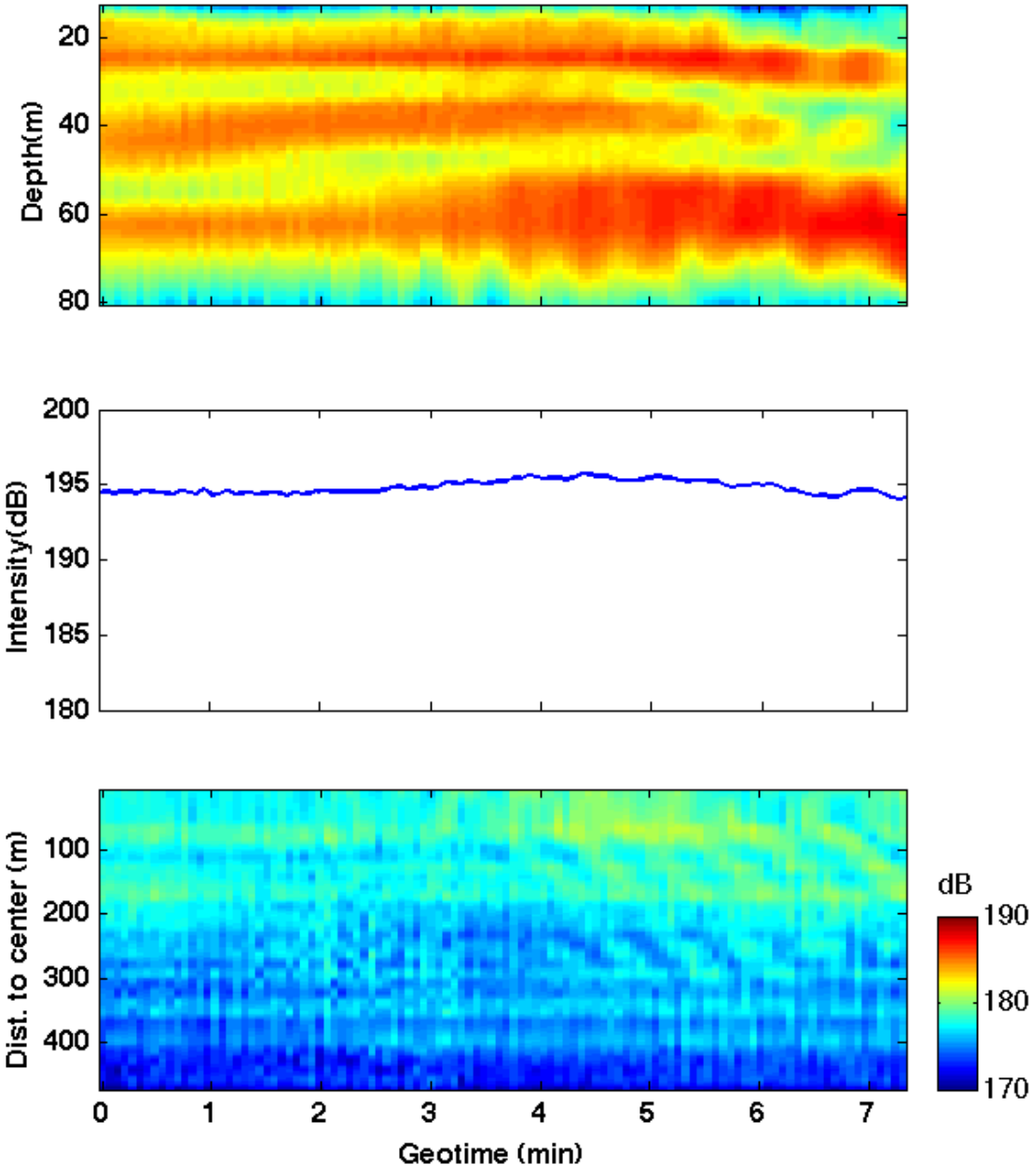

Figure 4.14: Received signal on Shark VLA (top), HLA (bottom) and signal intensity (middle) from Aug.17 21:30GMT to 21:37GMT

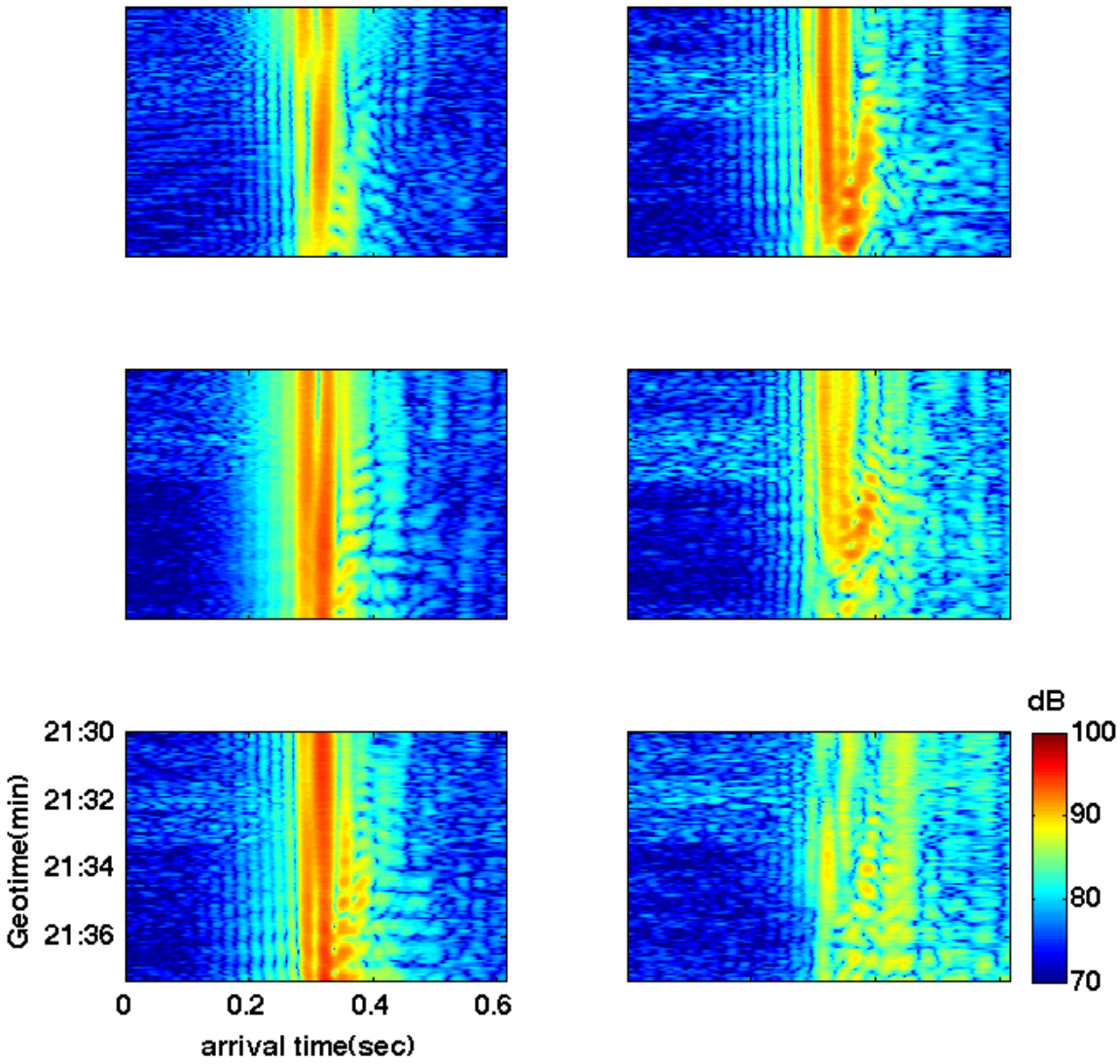

Figure 4.15: Mode decomposition of received signal on Shark VLA. Left column: mode 1-3, right column: mode 4-6

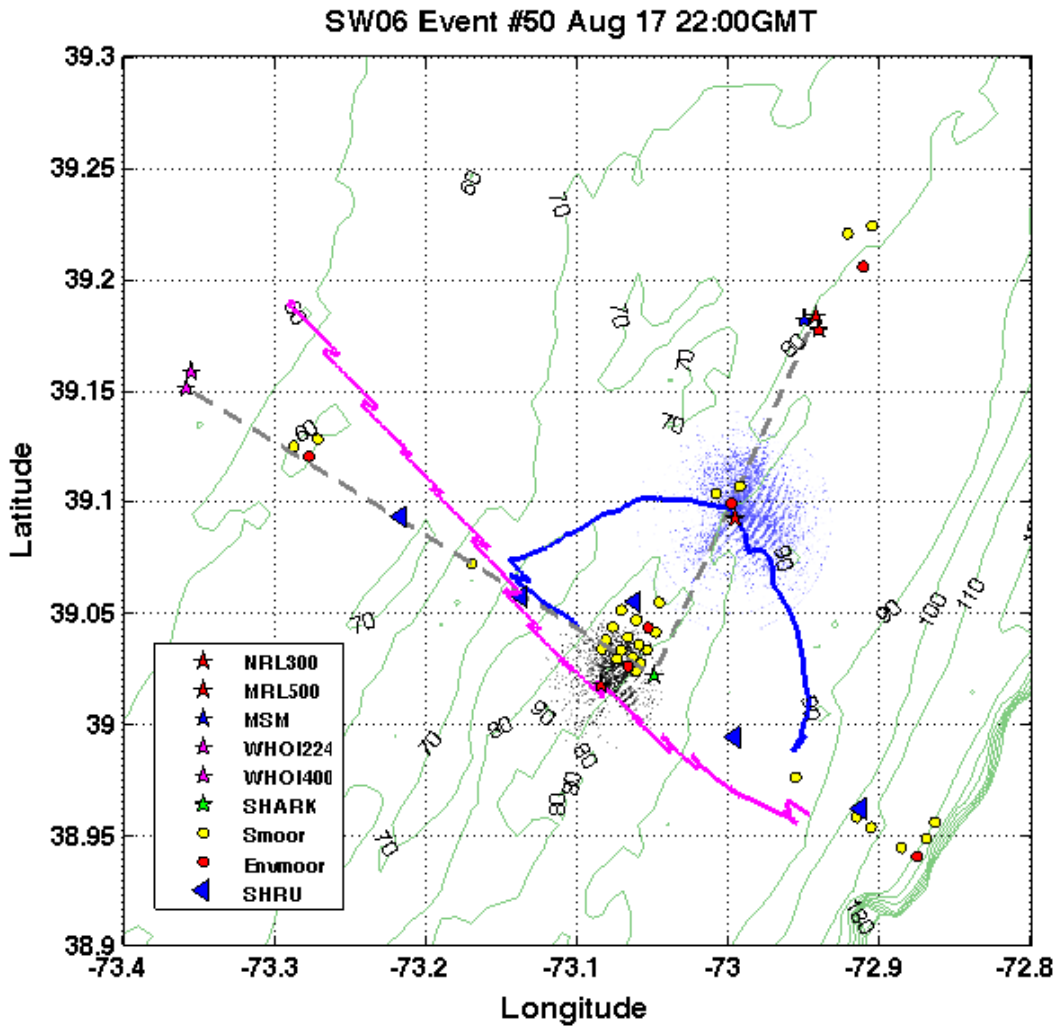

Figure 4.16: Surface expression of internal wave package at 22:00GMT, Aug. 17, recorded by R/V Sharp and R/V Oceanus. Blue and red lines indicate their movements, respectively. (Blue: R/V Sharp's, red: R/V Oceanus'

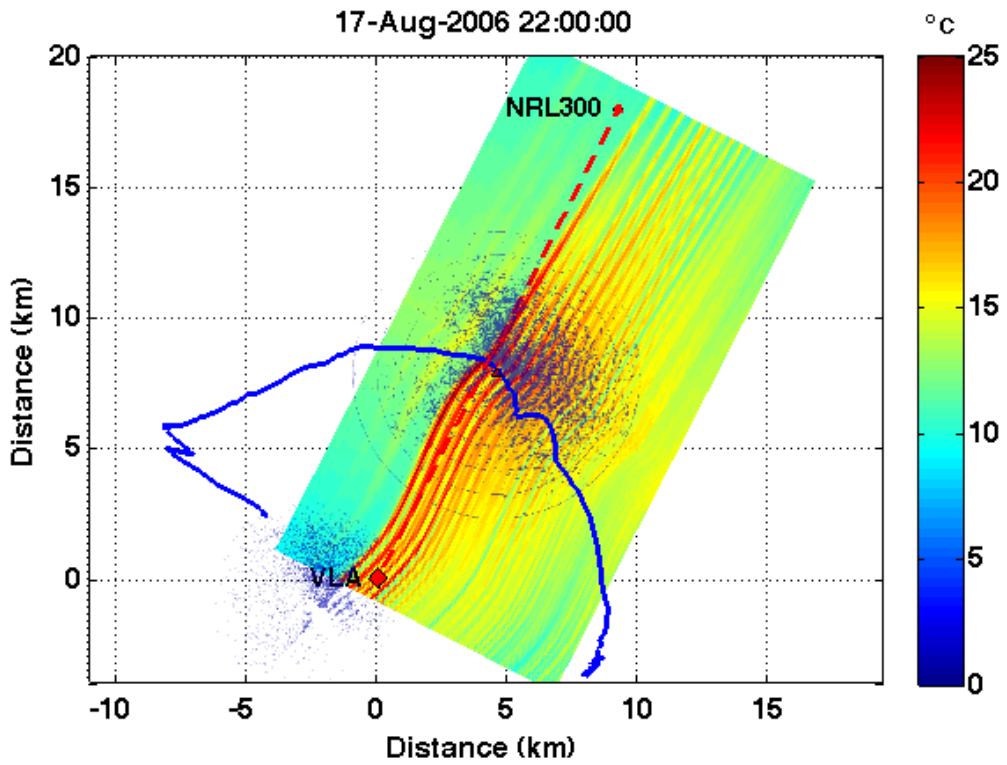

Figure 4.17: Interpolated internal wave field at 22:00GMT, Aug. 17, water depth = 20m. (Refer to section 3.4 for detailed interpolation method)

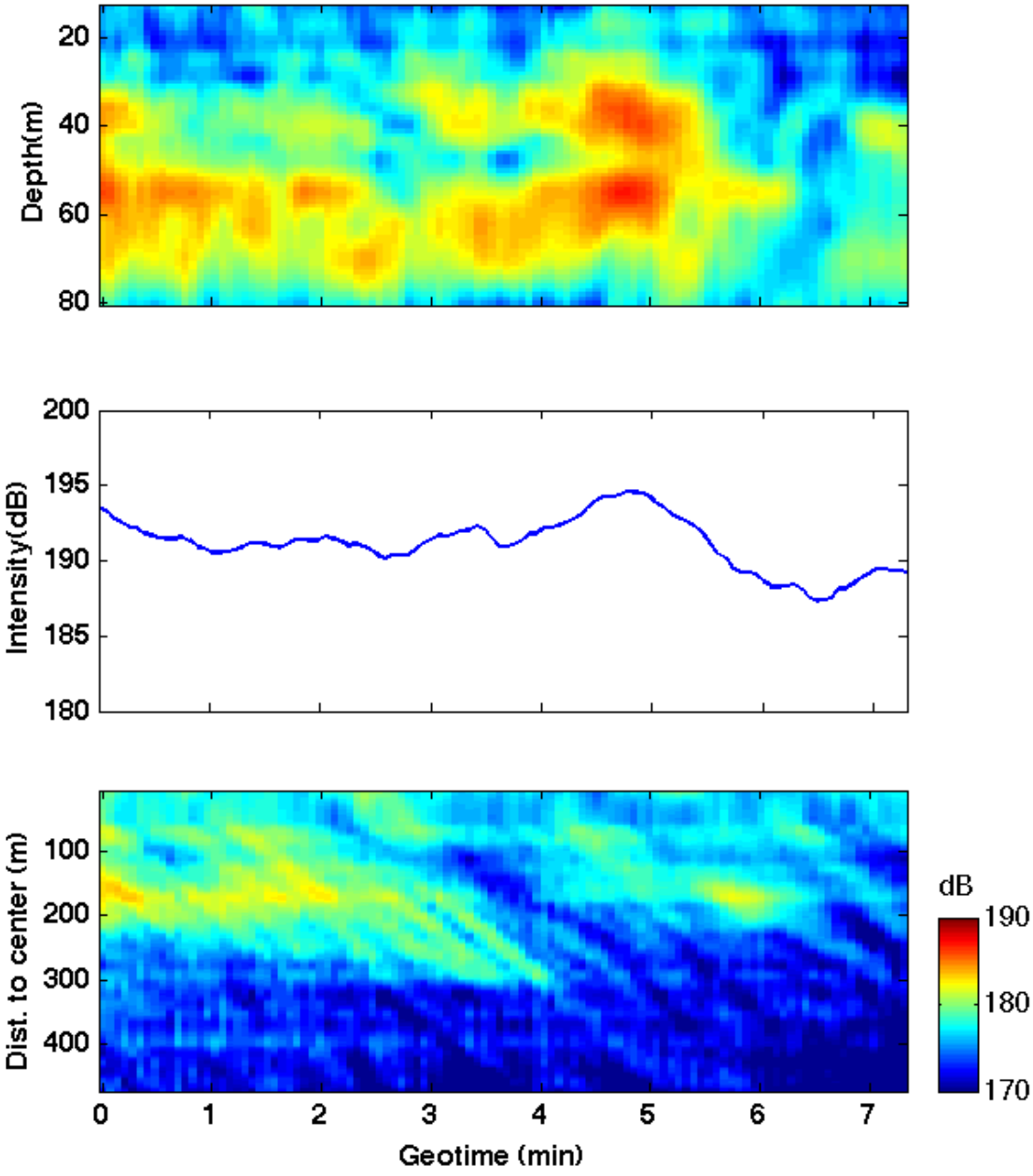

Figure 4.18: Received signal on Shark VLA (top), HLA (bottom) and signal intensity (middle) from Aug.17 22:00GMT to 22:07GMT

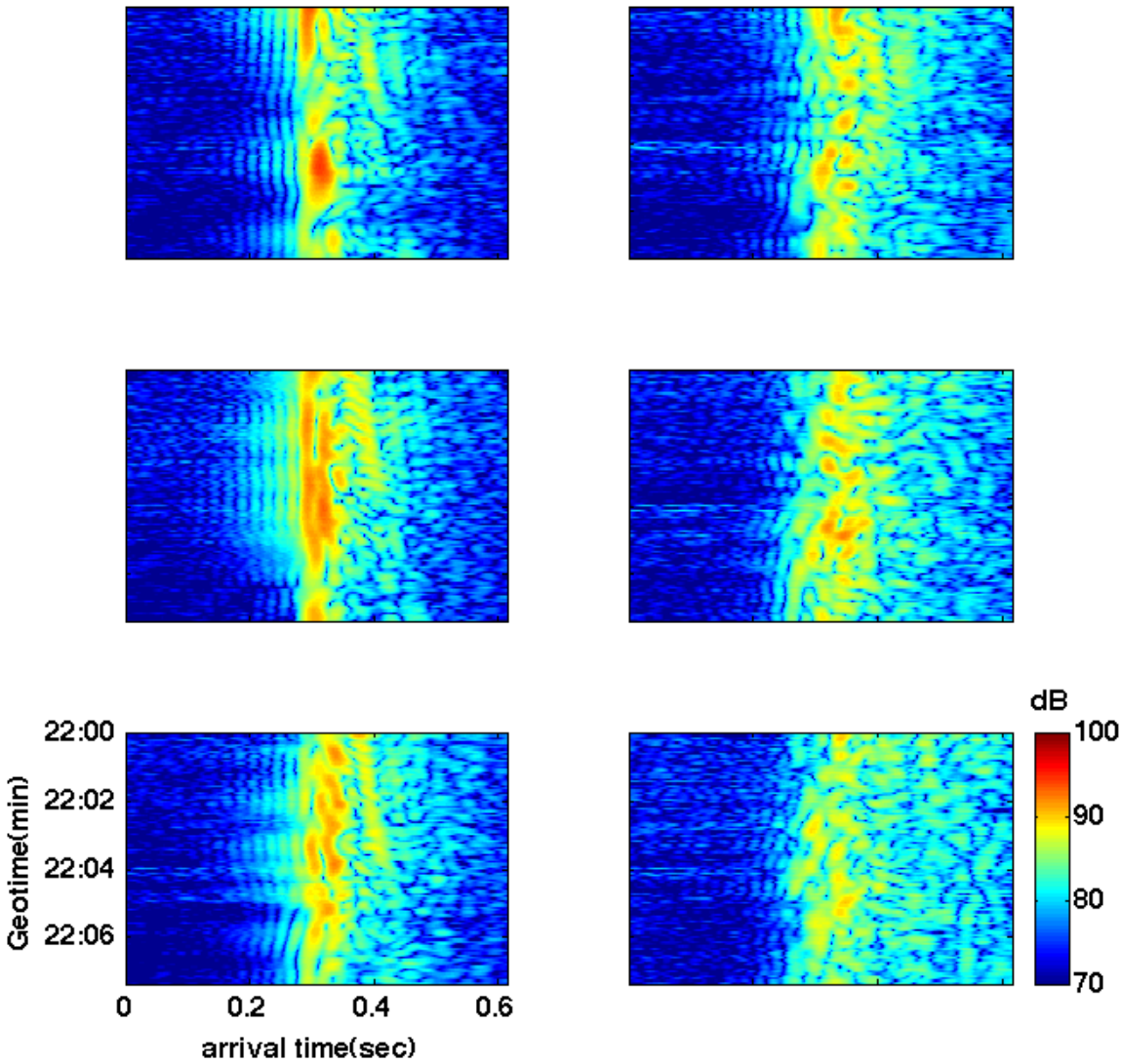

Figure 4.19: Mode decomposition of received signal on Shark VLA. Left column: mode 1-3, right column: mode 4-6

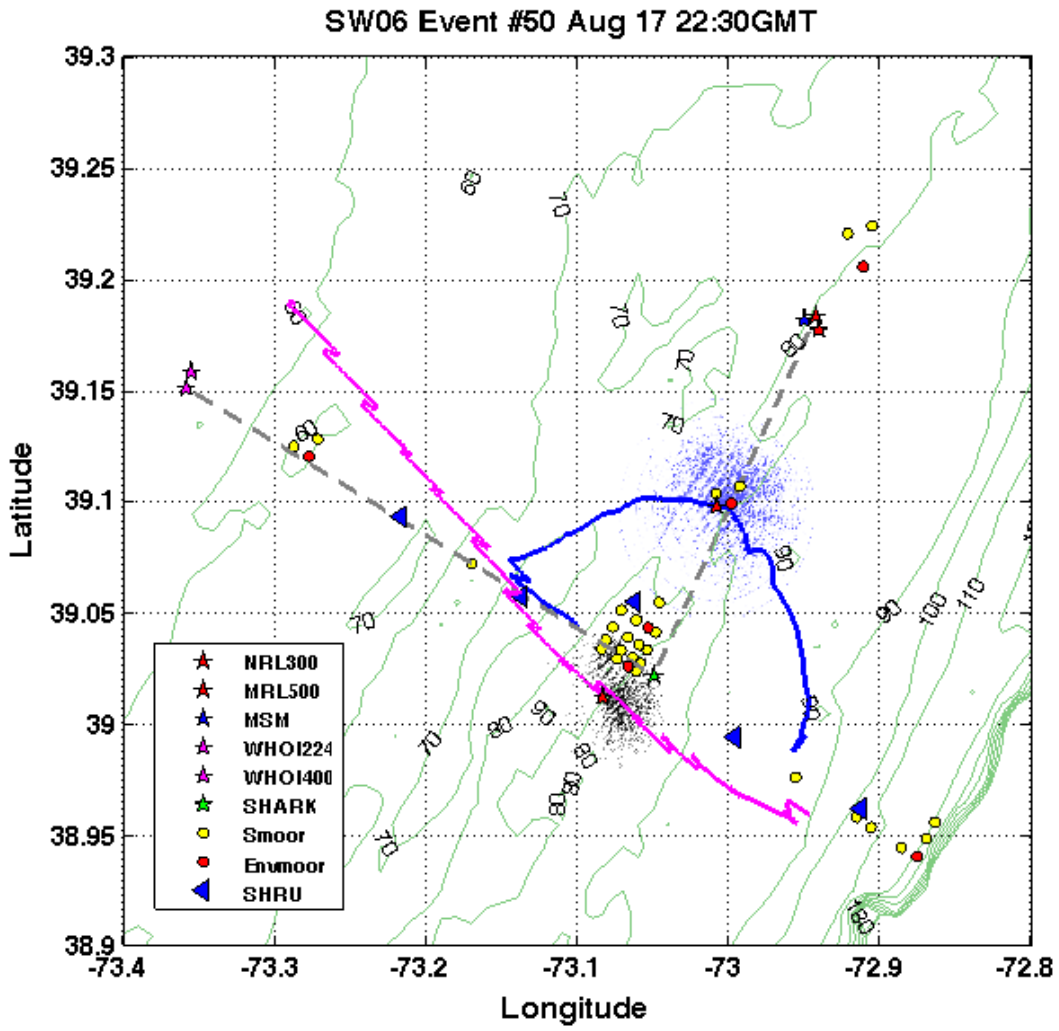

Figure 4.20: Surface expression of internal wave package at 22:30GMT, Aug. 17, recorded by R/V Sharp and R/V Oceanus. Blue and red lines indicate their movements, respectively. (Blue: R/V Sharp's, red: R/V Oceanus'

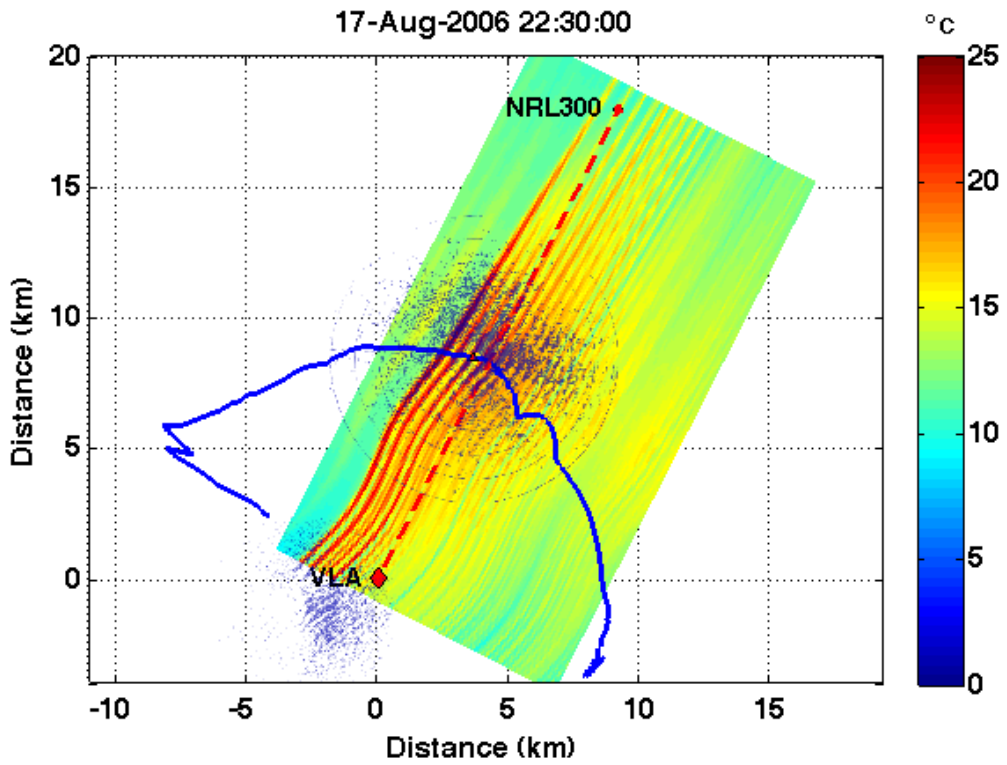

Figure 4.21: Interpolated internal wave field at 22:30GMT, Aug. 17, water depth = 20m. (Refer to section 3.4 for detailed interpolation method)

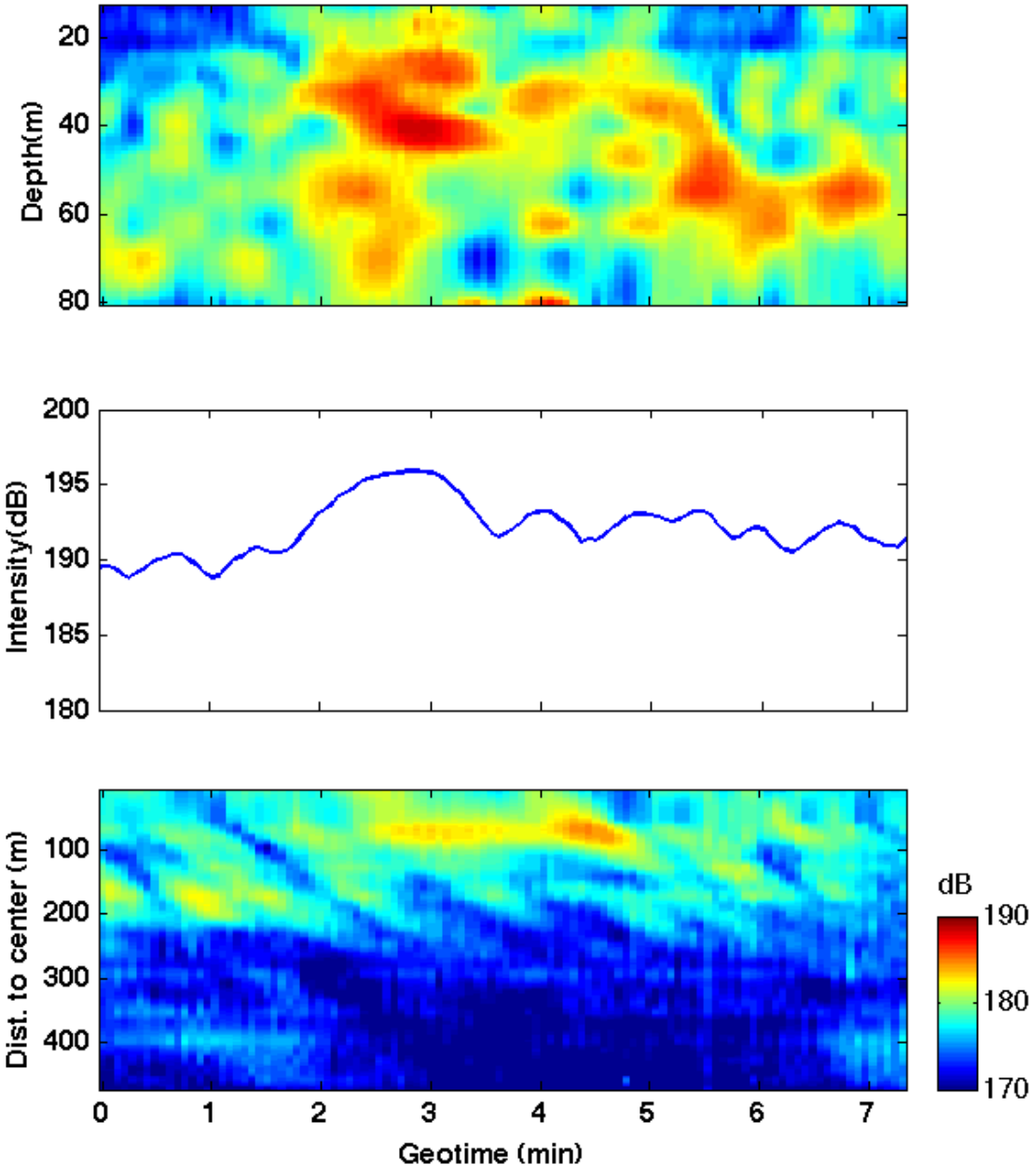

Figure 4.22: Received signal on Shark VLA (top), HLA (bottom) and signal intensity (middle) from Aug.17 22:30GMT to 22:37GMT

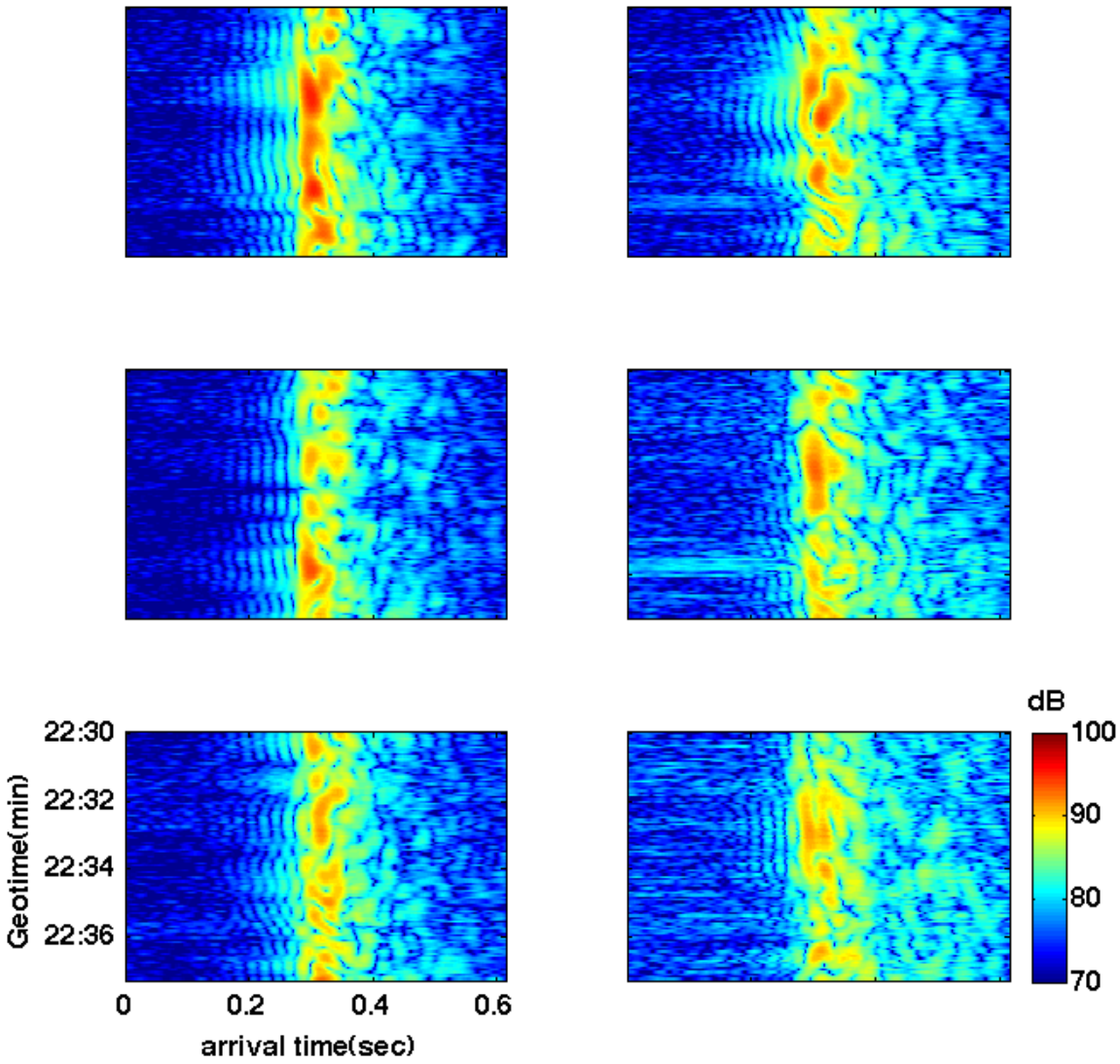

Figure 4.23: Mode decomposition of received signal on Shark VLA. Left column: mode 1-3, right column: mode 4-6

4.2 Transmissions from mobile source (R/V Sharp)

4.2.1 21:11GMT-21:27GMT

Radar image (figure??) shows at about 21:15GMT, a small ISW package reaches the VLA, which can also be verified on the temperature plots(figure??). Modes 3, 4 and 5 are starting to increase and oscillate around 21:22GMT, while the total intensity still shows little fluctuation.

4.2.2 21:41GMT-21:57GMT

ISW totally intersects the acoustic path. The fast oscillation in the previous period of the signal is replaced by single, strong focusing/defocusing. The fluctuation of the total intensity is about 8dB. Both VLA and HLA show strong fluctuation. HLA shows slopes during all transmission - means ISW is in the path. Also, note that the slope changes during 6 minutes. From the modal decomposition plots, it can be shown the focusing mainly happens to mode 1 and 2, when mode 3, 4, and 5 show little increase in intensity.

4.2.3 22:11GMT-22:27GMT

ISW moving across the entire acoustic path. At about 22:13, there is a small focusing event with 5dB increase in total intensity, which is shown on all the modes but more pronounced on mode 1 and 2 (??dB). It also shows on the HLA with a weak but consistent slope across all the hydrophones. At about 22:21-22:25, a longer-lasting focusing is recorded, which only happens at the water column below 35m. Mode 2 is the biggest contributor among all modes. On HLA, the focusing stops showing about 200m away from the center of SHARK.

4.2.4 22:41GMT-22:57GMT

The acoustic path starts to enter the tail of the ISW package, when the wave fronts are more irregular, and we lost the radar coverage at the receiver. The angle

between the acoustic path and the leading front is about 15° - the small angle assumption no long holds. Peaked at 22:51GMT, a major focusing event are clearly recorded with 8dB fluctuation in total intensity. It crosses all the hydrophones on the VLA and HLA. Modal decomposition shows the mode 1, 2 and 3 are the major contributors.

4.2.5 23:11GMT-23:27GMT

R/V Sharp is transmitting by a very big angle (30°). The fluctuation is very small (2dB). Mode 1 shows a peak at 23:14GMT, while mode 2 and 4 start to grow at 23:13GMT. Mode coupling?

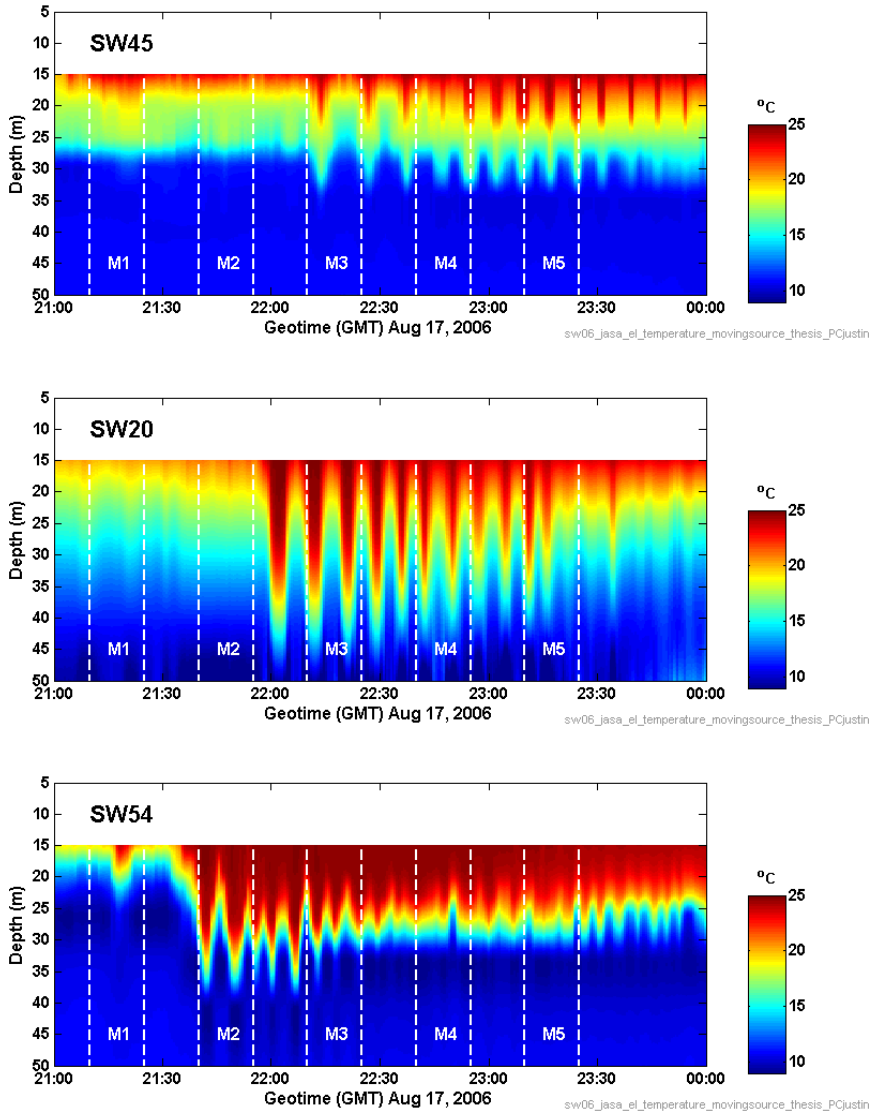

Figure 4.24: Temperature record at three location along the fixed sourc-receiver track. Panel (a), (b) and (c) show the temperature at the NRL300 source (SW45), the midpoint (SW20) and the Shark VLA (SW54).

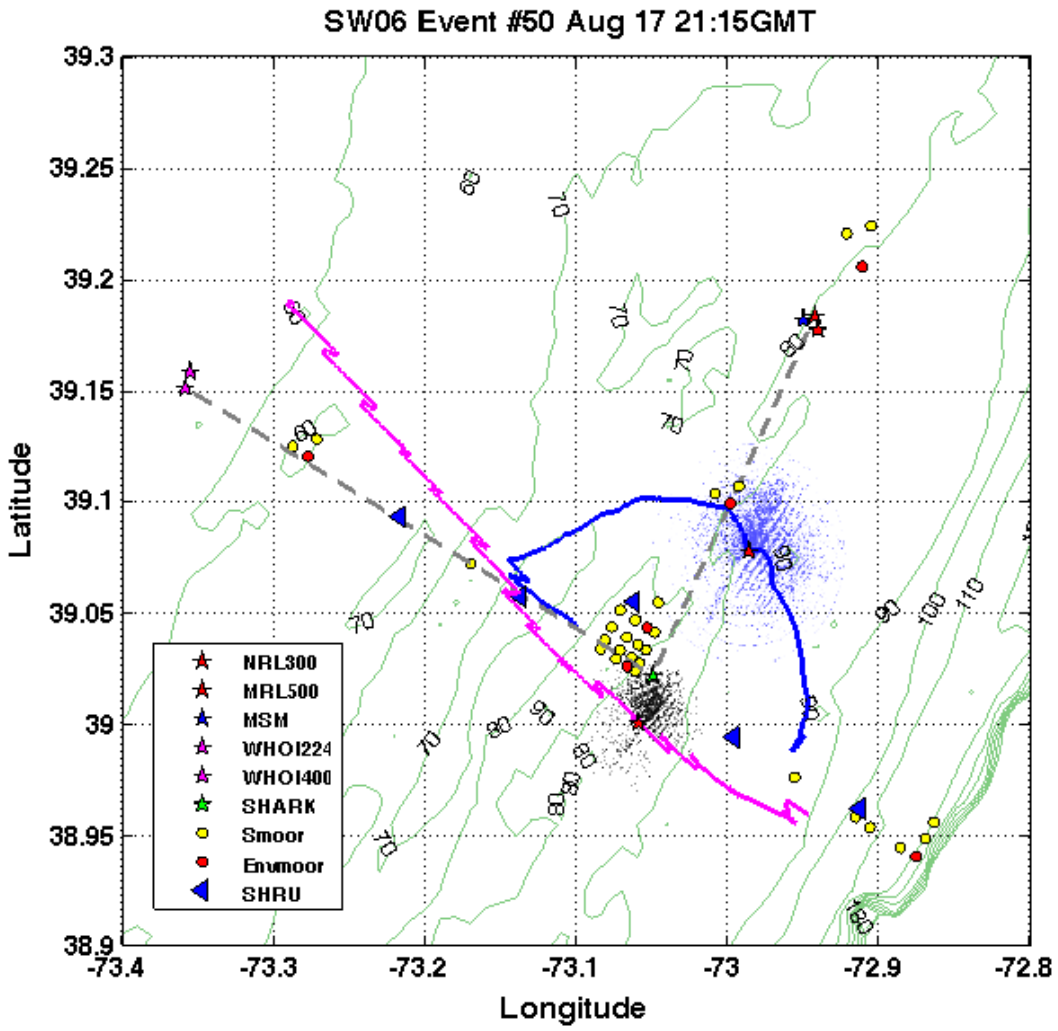

Figure 4.25: Surface expression of internal wave package at 21:15GMT, Aug. 17, recorded by R/V Sharp and R/V Oceanus. Blue and red lines indicate their movements, respectively. (Blue: R/V Sharp's, red: R/V Oceanus'

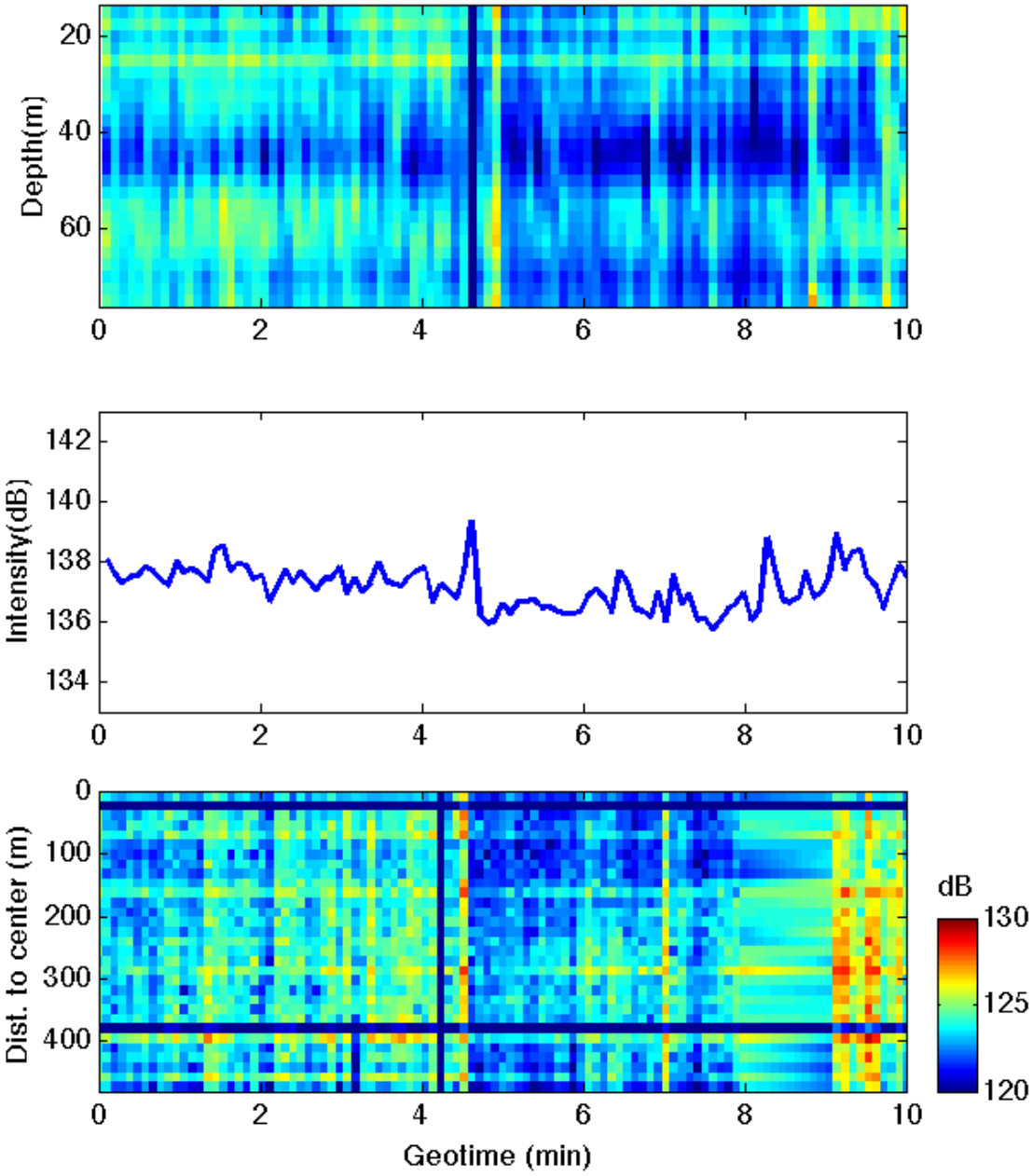

Figure 4.26: Received signal on Shark VLA (top), HLA (bottom) and signal intensity (middle) from Aug.17 21:15GMT to 21:25GMT

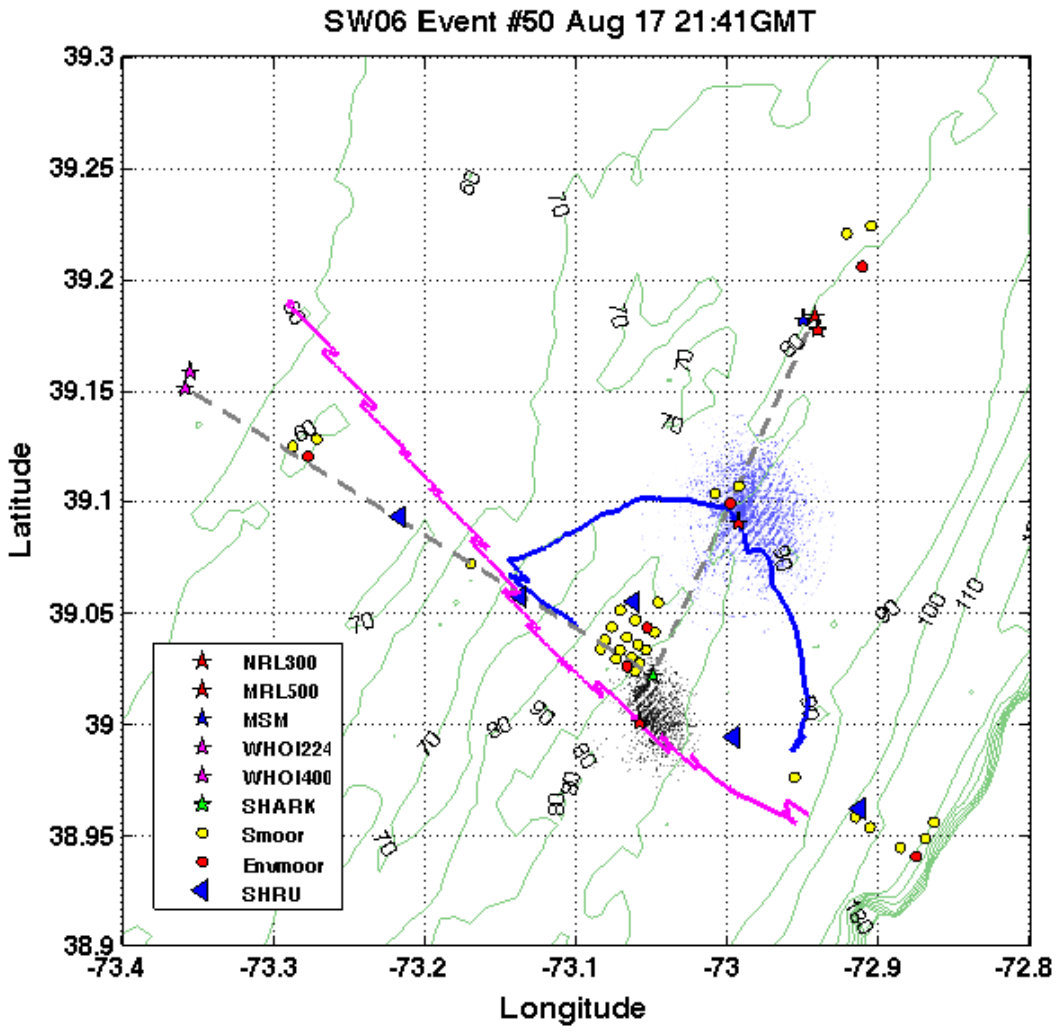

Figure 4.27: Surface expression of internal wave package at 21:41GMT, Aug. 17, recorded by R/V Sharp and R/V Oceanus. Blue and red lines indicate their movements, respectively. (Blue: R/V Sharp's, red: R/V Oceanus'

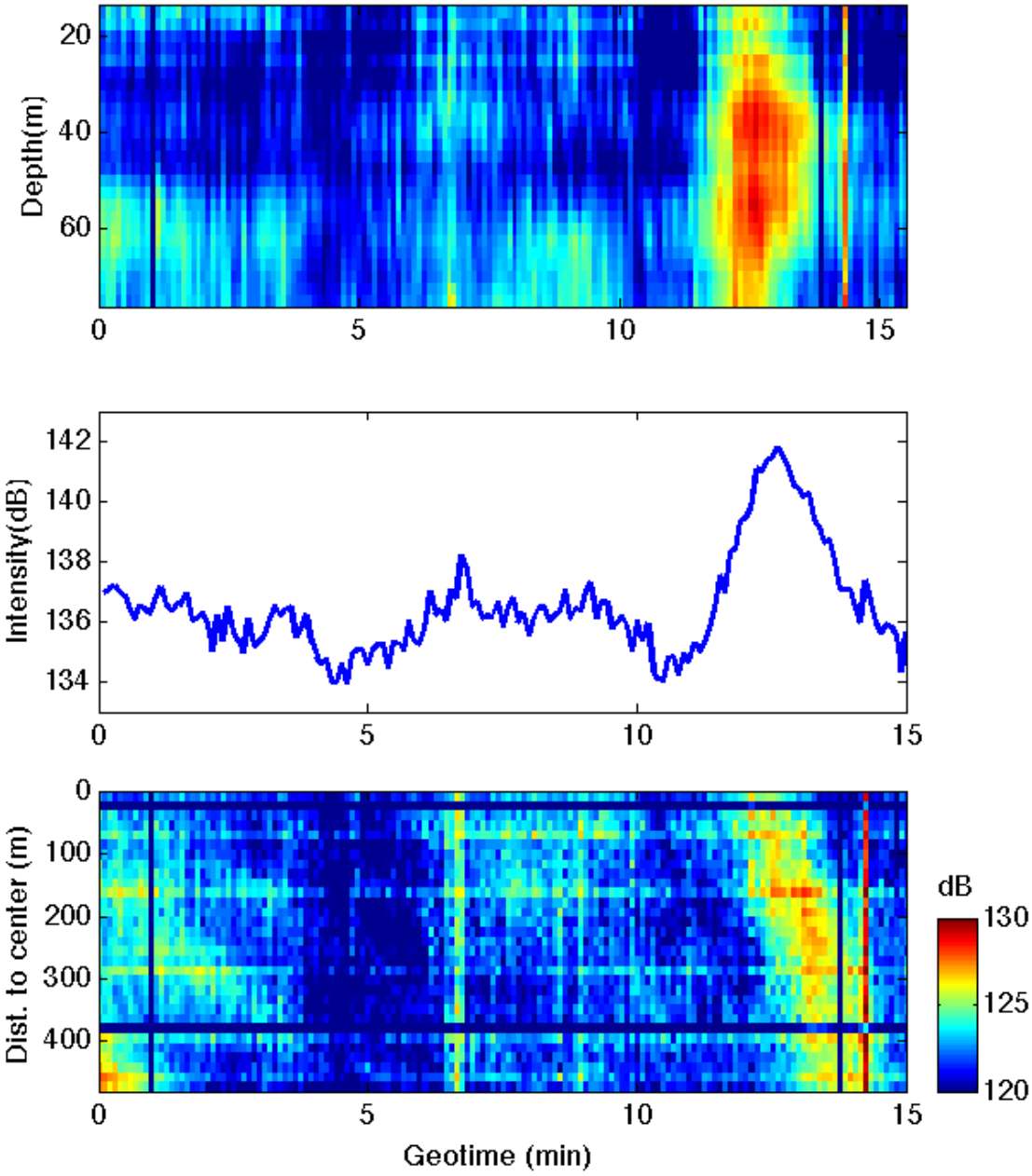

Figure 4.28: Received signal on Shark VLA (top), HLA (bottom) and signal intensity (middle) from Aug.17 21:41GMT to 21:56GMT

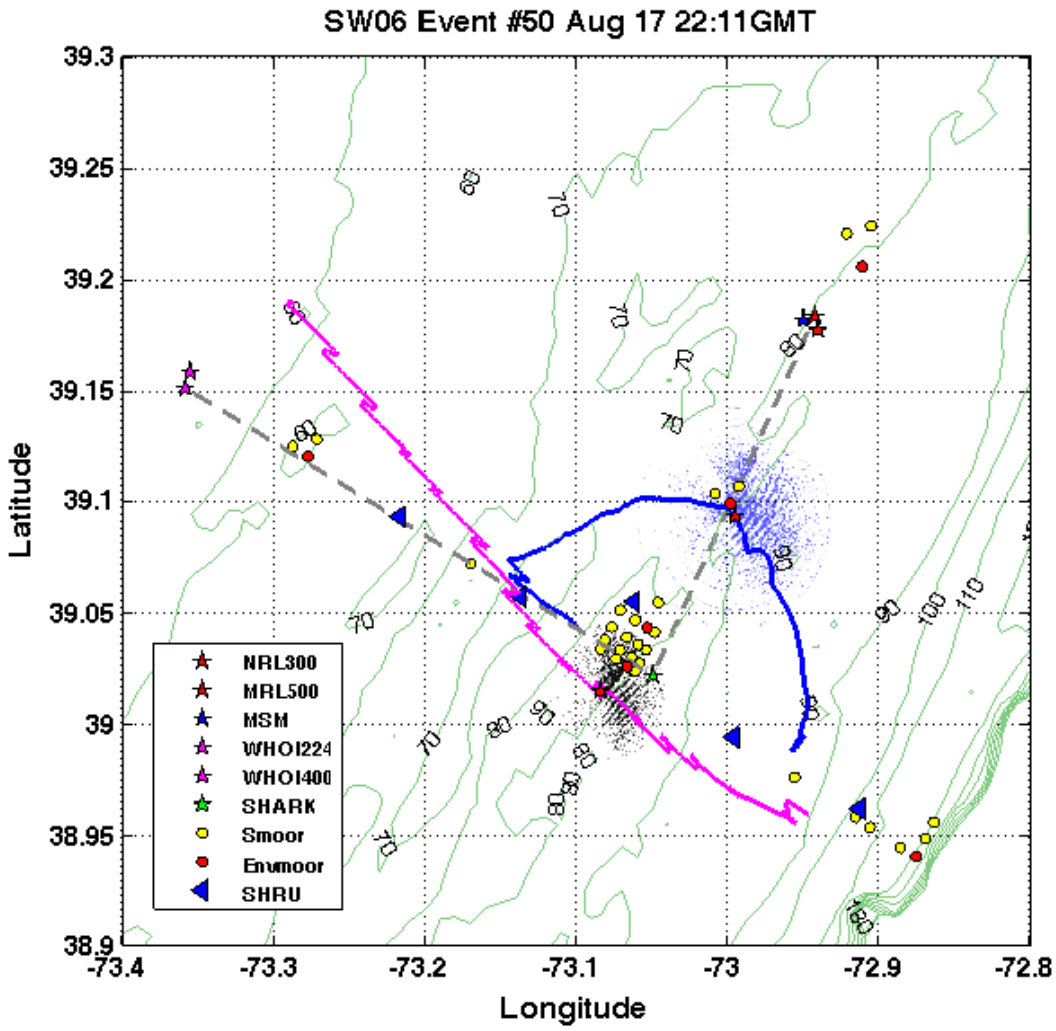

Figure 4.29: Surface expression of internal wave package at 22:11GMT, Aug. 17, recorded by R/V Sharp and R/V Oceanus. Blue and red lines indicate their movements, respectively. (Blue: R/V Sharp's, red: R/V Oceanus'

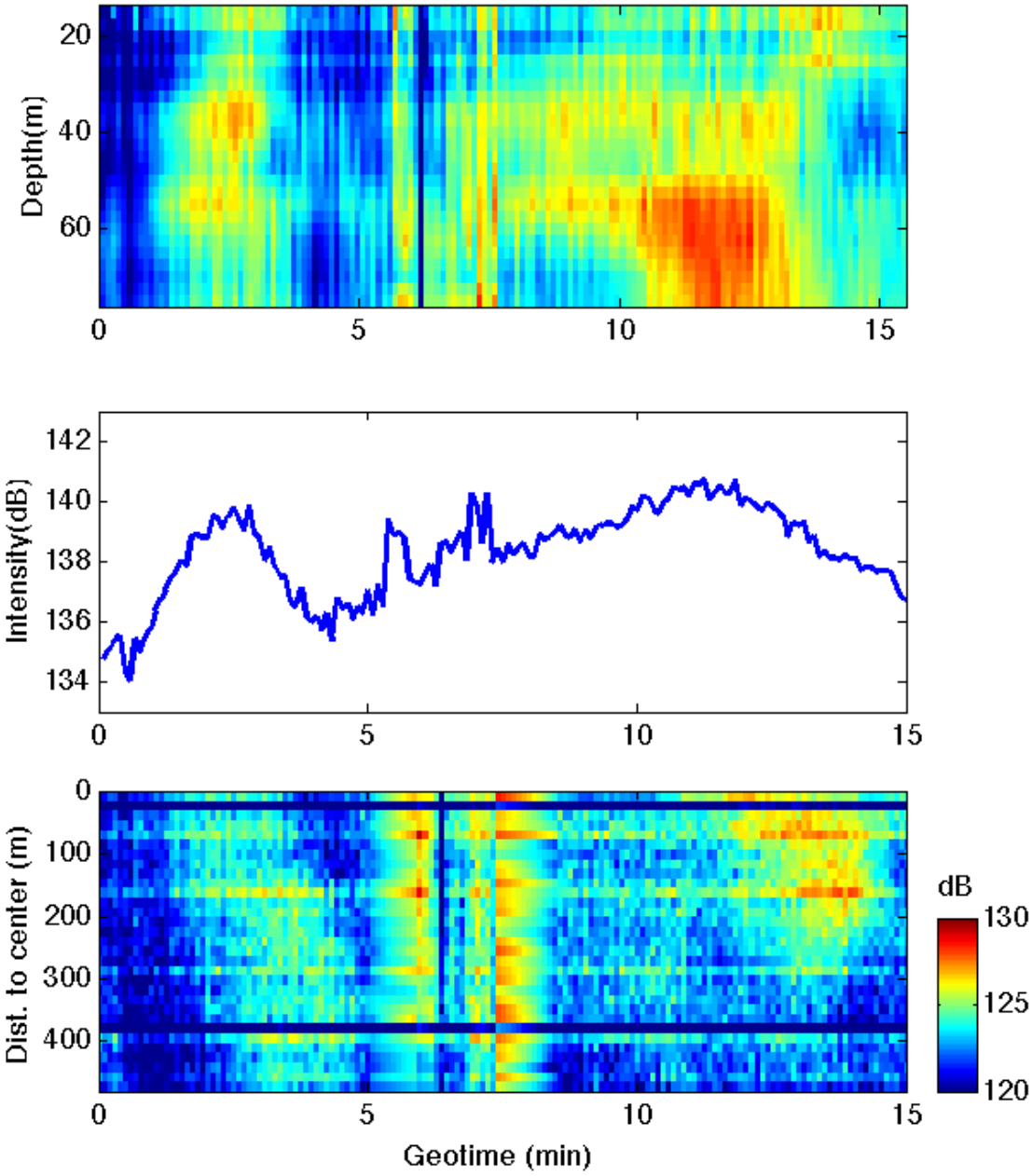

Figure 4.30: Received signal on Shark VLA (top), HLA (bottom) and signal intensity (middle) from Aug.17 22:11GMT to 22:26GMT

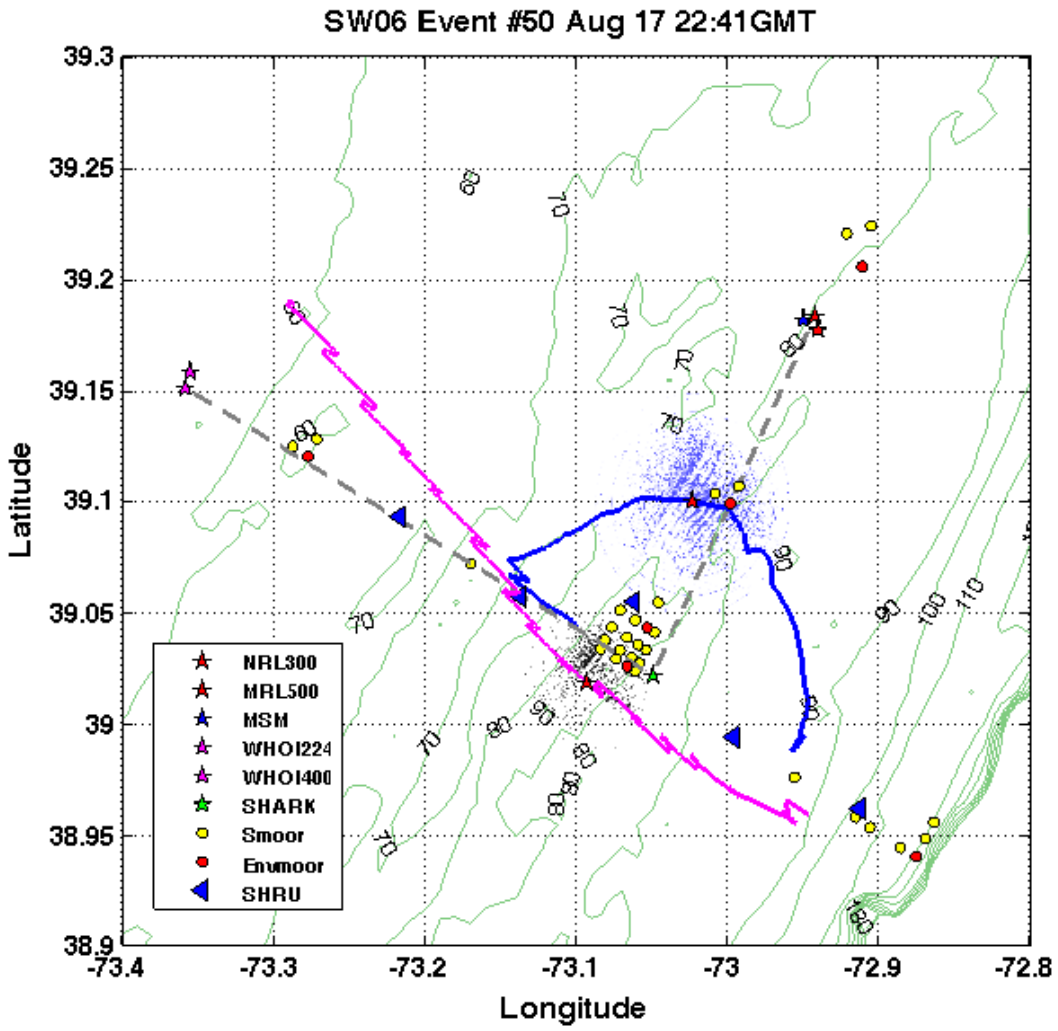

Figure 4.31: Surface expression of internal wave package at 22:41GMT, Aug. 17, recorded by R/V Sharp and R/V Oceanus. Blue and red lines indicate their movements, respectively. (Blue: R/V Sharp's, red: R/V Oceanus'

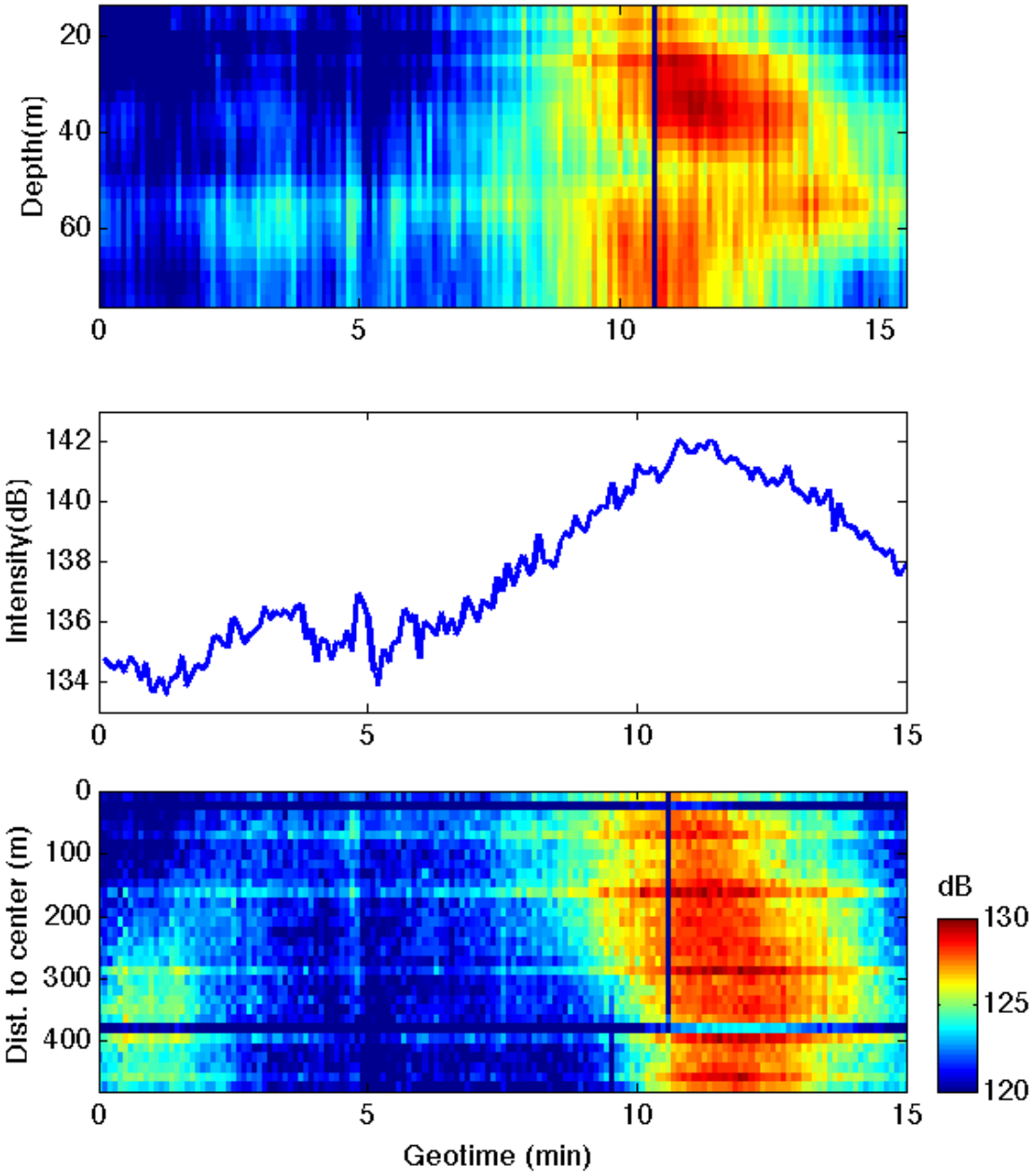

Figure 4.32: Received signal on Shark VLA (top), HLA (bottom) and signal intensity (middle) from Aug.17 22:41GMT to 22:46GMT

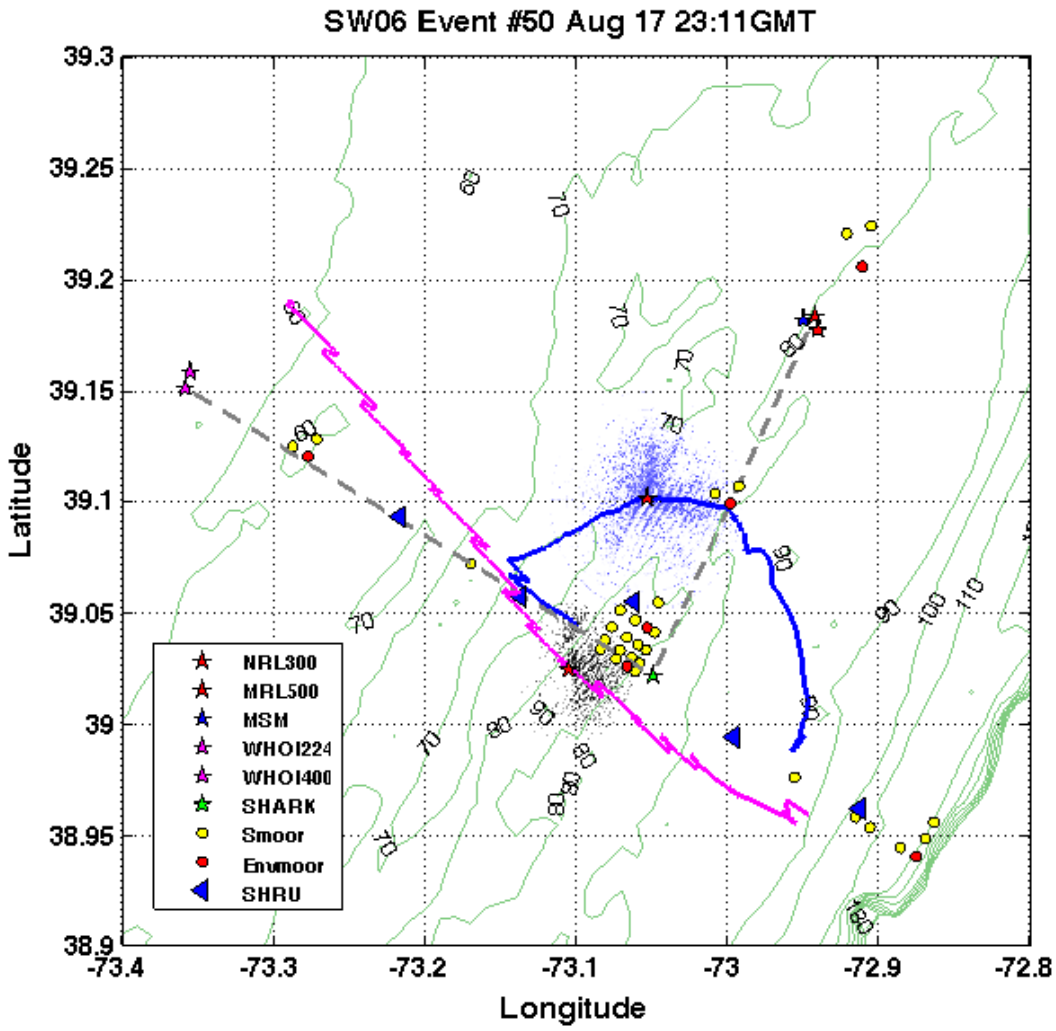

Figure 4.33: Surface expression of internal wave package at 23:11GMT, Aug. 17, recorded by R/V Sharp and R/V Oceanus. Blue and red lines indicate their movements, respectively. (Blue: R/V Sharp's, red: R/V Oceanus'

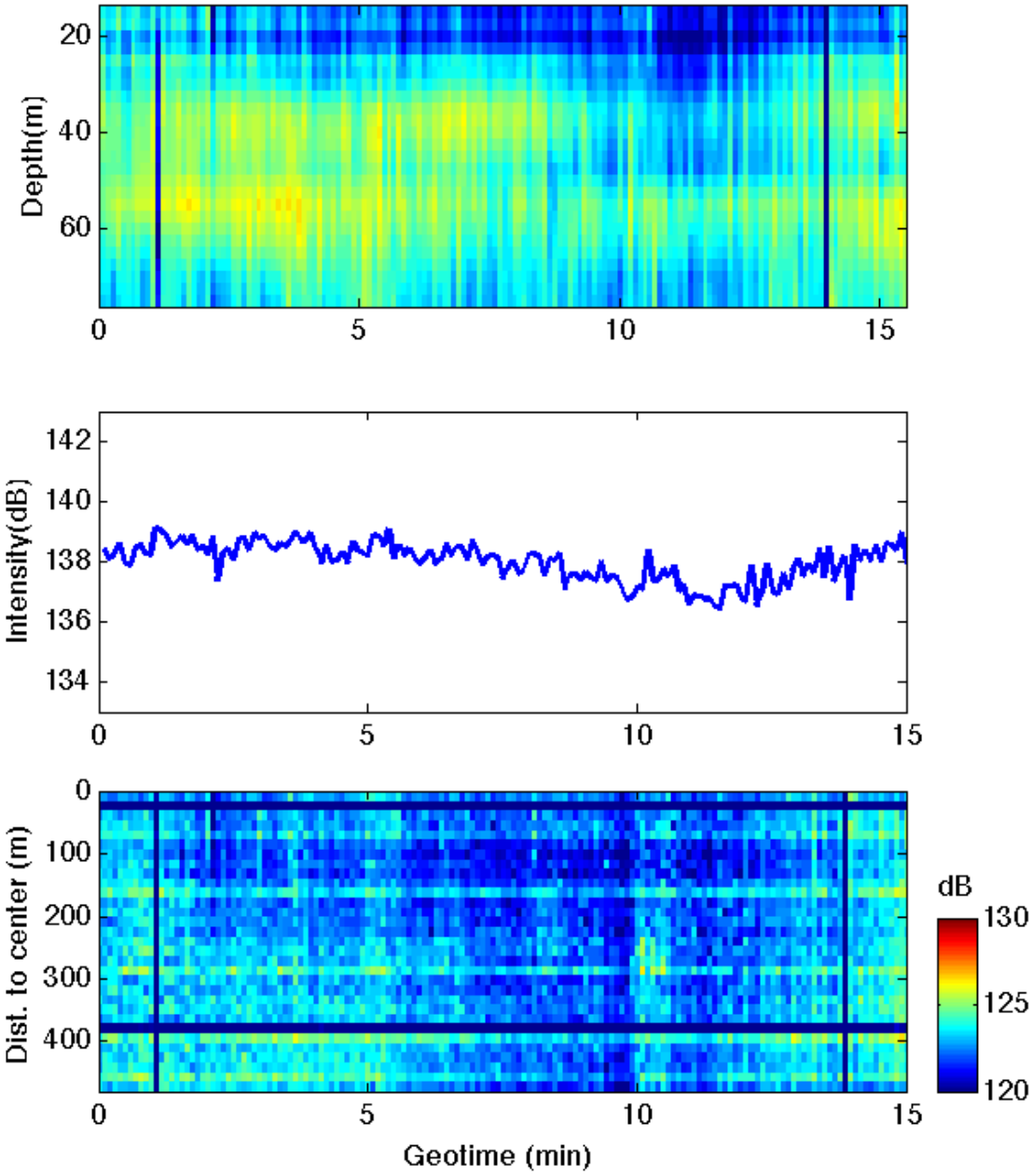

Figure 4.34: Received signal on Shark VLA (top), HLA (bottom) and signal intensity (middle) from Aug.17 23:11GMT to 23:26GMT

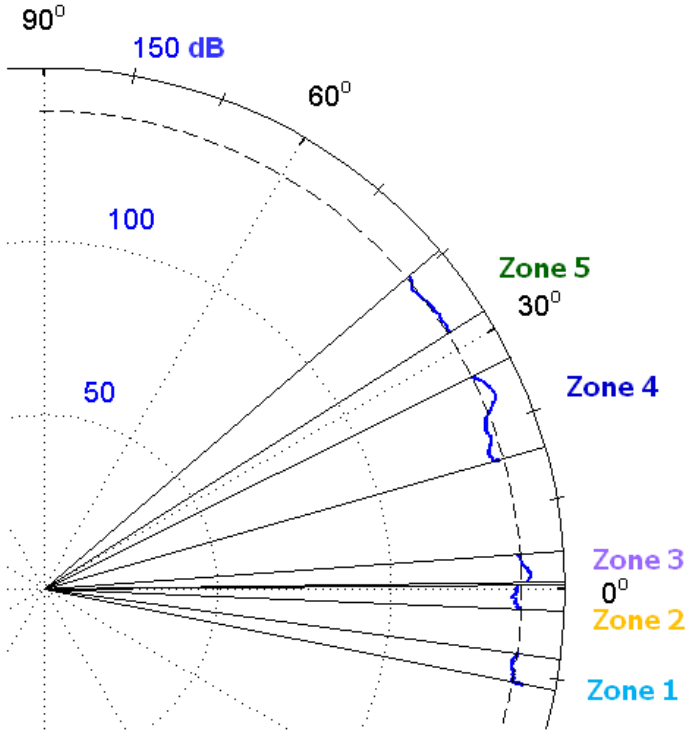

Figure 4.35: Data of depth-integrated intensity and estimated angle for each zone

Chapter 5

ANALYSIS AND MODELING

5.1 Intensity fluctuation and statistics

Based on the theory proposed in our previous work, the angle between the ISW fronts and the acoustic track determines the mechanism of the intensity fluctuations. Small angles provide horizontal refraction and focusing while larger angles cause mode coupling. Between these limits, there is an angular region for which the propagation is adiabatic. During internal wave Event 50, the ISW fronts passed through the acoustic track at an angle of about 5° providing the condition for horizontal refraction. Prior to the ISW arrival, we observe stable adiabatic propagation in a stable water column. Hence, a transition can indeed be observed between these two mechanisms.

To show a focusing event, we consider two geotimes: (a) T_{g1} when the leading internal wave front had not reached the acoustic track and, (b) T_{g2} when the internal wave packet occupied most of the acoustic track. We calculate the total intensity integrated over the depth H as

$$I(T) = \int_0^H I(z,T)dz \tag{5.1}$$

where $I(z,T) = \frac{1}{\rho c} \int_{\tau}^{\tau+\Delta\tau} p^2(z,T,t)\,dt$ is the intensity of the signal arrivals integrated over a pulse length $\Delta\tau$ at a given depth z, where p is acoustic pressure,ρ is water density, and c is sound speed. The distribution of the ISWs in the horizontal plane can be assessed by carefully examining the radar image and the depth distribution of the temperature at three points (SW45, SW20, SW54) along the acoustic track.

The temperature distribution starting at 20:30:00 GMT (T_{g1}) for the transmission period (i.e. $\sim$ 7.5 minutes) at three different moorings shows very little fluctuation

along the acoustic track (see Fig. 2).This indicates that the ISW has not reached the acoustic track during T_{g1}, as is also shown in the radar image. In Fig.**??**(a) we show a plot of I(z,T) for the VLA. It is shown that for a repeated pulse of the same radiated intensity, only minor temporal intensity variation exists. In Fig.**??**(b) we plot the depth integrated intensity for all geotimes, I(T). The very small fluctuations (3 dB) at T_{g1} indicate a quiescent condition without ISWs in the track. This means that during this period of observation there is no redistribution of sound energy in the horizontal plane, i.e. there is no horizontal refraction. Small variations of the depth distribution of the sound intensity correspond to the adiabatic case. Fig.**??**(c) shows the acoustic intensity on the HLA. There are no apparent temporal intensity variations on the HLA during this geotime.

I(z,T) for T_{g2} is plotted in Fig.**??**(d). Here we see increasing and decreasing trends in sound intensity over the VLA, which are synchronous in depth. The average intensity I(T) using Eq. (1) peaks to 35 dB around 22:04:30 to 22:05:00 GMT, and decreases to 20 dB around 22:06:37 GMT as shown in Fig.**??**(e). This significant fluctuation corresponds to redistribution of the acoustic energy in the horizontal plane, which in the limit can be referred to as focusing or defocusing events and is related to the position of the source and/or receiver with respect to the internal wave crests. The focusing and defocusing are also shown in Fig.**??**(c) and Fig.**??**(d). In this case (i.e. T_{g2}), the receiver is between two adjacent maxima of the thermocline displacement, and the high intensity fluctuations (15 dB peak to peak) are due to horizontal refraction effects similar to those shown in previous studies.3 Temporal fluctuations correlate with oscillations of the thermocline layer at the receiver (see Fig. 2) due to ISWs (period is 7-8 min). The fluctuations in the presence of internal waves (i.e. at T_{g2}) are about 15 dB, which are much larger than those of T_{g1} (3 dB) with no internal wave in the acoustic track. Although the total jump in the thermocline thickness (i.e. from 15 m to 30 m) could make a difference in the 'absolute' value of the acoustic intensity, it does not play a significant role in the temporal intensity fluctuation with periods corresponding to the ISW.

As in the quiescent case shown above, Fig.**??**(f) shows the acoustic intensity on the HLA for the active period (T_{g2}). During the geotime of about 7.33 minutes, we see the variation of the sound field at the horizontal array. For the variation observed during the first 3 minutes, there are two large intensity maxima observed at the HLA. These become weaker and disappear during the second half of the time period (after 22:03 GMT). This behavior, in our opinion, is a manifestation of horizontal redistribution of the sound intensity, which we call focusing/defocusing phenomena. The sloped intensity modulations correspond to the motion of an interference pattern registered on the horizontal array, which can be a result from any motion of the water layer (such as an ISW packet). The velocity of this interference pattern is estimated as 1-1.5 m/s from the acoustic data [shown as a slope in Fig. 4(f)]. This may not be directly related to the velocity of the internal solitons (measured from shipboard radar to be about 1 m/s). Further detailed modeling is needed to understand the nature of these fluctuations and their relationship to the slope of the lines shown in Fig. 4(f).

5.2 Acoustic signal coherence time and length

The fluctuation of received acoustic signal can also be described with its coherence time and length using the lagged autocovariance function defined as

$$C_{i,t} =< I(t,z)I(t+\tau,z) > \tag{5.2}$$

The autocovariance function is strongly dependent on the position of the internal wave front with respect to the acoustic path.

5.2.1 Fixed source

Before IW, the autocovariance function (Fig

5.2.2 Moving source

5.3 Behavior of horizontal ray beams

5.3.1 Horizontal Ray

5.3.2 Horizontal beamforming

5.3.3 Single mode propagation

5.3.4 Mode coupling

5.4 Horizontal Lloyd's mirror effect

Introduction to optical Lloyd's mirror effect and acoustic equivalent.

5.4.1 Two-dimensional case

We start with 2D propagation case on the horizontal plane in an environment with an approaching wave front. This provides a concise picture of the relationship between the internal wave movement and the acoustic propagation.

We assume the high temperature front brought by internal waves is well mixed and is across the entire water column. This assumption effectively reduces the problem to a 2D case. Figure 3 shows the geometry of the simplified experimental setup on the horizontal plane. For a single frequency acoustic signal, the acoustic pressure at receiver can be written as

$$p(r,t) = a_1 e^{i(\omega t - kr_1} + a_2 e^{i(\omega t - kr_2)} \tag{5.3}$$

r_1 is the direct path between the source and receiver, and r_2 is the reflected (or refracted) ray path from the high temperature internal wave front in horizontal plane, hense a function of geotime $r_2 = r_2(T)$. Here, a_1 and a_2 are the amplitudes of acoustic wave along two paths. ω is the angular frequency, k is the acoustic wave number, and as usual, $k = \frac{\omega}{c}$, where c is the sound speed.

The intensity of a sinusoidal acoustic signal $I = |p|^2$ is,

$$I(T) = a_1^2 + a_2^2 + 2a_1 a_2 cos\{k[r_1 - r_2(T)]\} \tag{5.4}$$

Figure 4(a) shows a 7.5 min segment of the frequency dependent intensity pattern matching the LFM transmission in SW06 experiment. A 30min segment is plotted

in Fig. 4(b) to show the long geotime trend that is the changing of the slope and the broadening of the stripes, as observed from experimental data in Fig. 2(d).

The period Γ and the slope of the beating interference patterns shown in Fig. 2(d) both increase as the internal wave front approaches the acoustic track. Although the slope only changes slightly during the 7.5min transmission time, it is a measurable quantity that can be calculated as follows. From Eq. ??, the angular frequency of the oscillating intensity as a function of wave number k is

$$\Omega = \frac{d}{dt}k(r_1 - r_2) \tag{5.5}$$

If specular reflection assumption is used (i.e., the path shown by the dashed line in Fig. 3), Ω can be written in terms of the IW approaching speed v , the source position $(0, y_s)$ and receiver position $(x_r, 0)$.

$$\Omega(T) = 2k\frac{(y_s - 2vT)v}{\sqrt{x_r^2 + (y_s - 2vT)^2}} \tag{5.6}$$

The period of the beating oscillations is simply $\Gamma(T) = 2\pi/\Omega$, and is a function of the geotime. As the IW front gets closer to the acoustic path, interference between the direct and reflected (or refracted) paths causes a beating pattern. Using the specular reflection assumption, we can write the period as

$$T = \frac{\pi\sqrt{x_r^2 + (y_s - 2vT)^2}}{k(y_s - 2vT)v} \tag{5.7}$$

The minima of the acoustic intensity occurring at , from which the length difference of the two paths can be written as

$$r_1 - r_2 = (2n + 1)\pi/k \tag{5.8}$$

in which, the integer n represents the number of stripes. The acoustic frequency $f = kc/2\pi$ can be written as a function of geotime as

$$f = \frac{(2n + 1)c}{2(r_1 - r_2(T))} \tag{5.9}$$

The slope $s = df/dt$ of the n-th stripe in the time-frequency spectrogram is

$$s = \frac{d}{dT}\left(\frac{(2n+1)c}{2(r_1 - r_2(T))}\right) \tag{5.10}$$

Using specular reflection assumption,

$$s = -c \cdot v(2n+1)\frac{(y_r + y_s - 2vT)}{(r_1 - r_2)^2 r_2} \tag{5.11}$$

The period and the slope in equations 5.7 and 5.11 are plotted in Fig. ?? and ?? for $f = 280Hz$, which is the frequency of the largest intensity in the received signal. To demonstrate the gradual increase of these variables, we show a 30-minute geotime segment prior to the IW arrival at the acoustic track. The IW reaches the receiver at 0 minute. At the -7 minute mark, the period $\Gamma = 0.70min$ and the slope $s - 50.83Hz/min$ respectively. These are in excellent agreement with the values in the experimental data at 21:37GMT, shown in Fig. ??.

Next we discuss the intensity of a broadband LFM signal. The integrated acoustic intensity of a LFM signal can be written as:

$$I_{int} = (a_1^2 + a_2^2)\Delta\omega + \frac{4a_1 r_2 c}{r_1 - r_2}\left(sin\frac{\Delta k(r_1 - r_2)}{2} \cdot cos(k_c(r_1 - r_2))\right) \tag{5.12}$$

5.4.2 Three-dimensional case

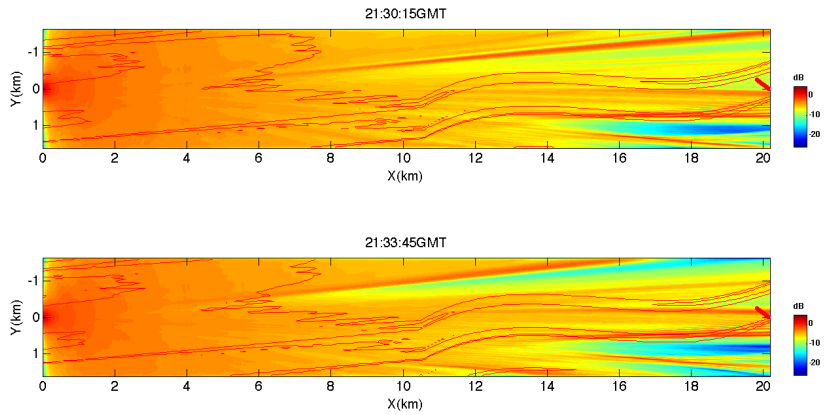

Figure 5.1: Depth integrated intensity from PE modeling results at 21:30:15GMT and 21:33:45GMT repectively, with a short white line indicating the length and direction of the Shark HLA

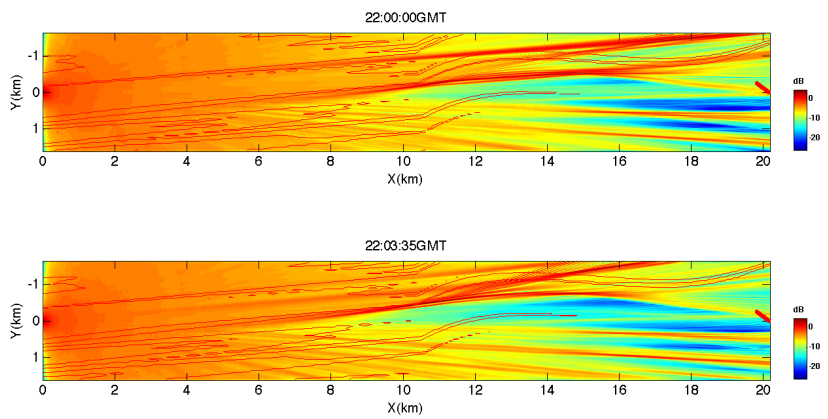

Figure 5.2: Depth integrated intensity from PE modeling results at 22:00:00GMT and 22:03:35GMT repectively, with a short white line indicating the length and direction of the Shark HLA

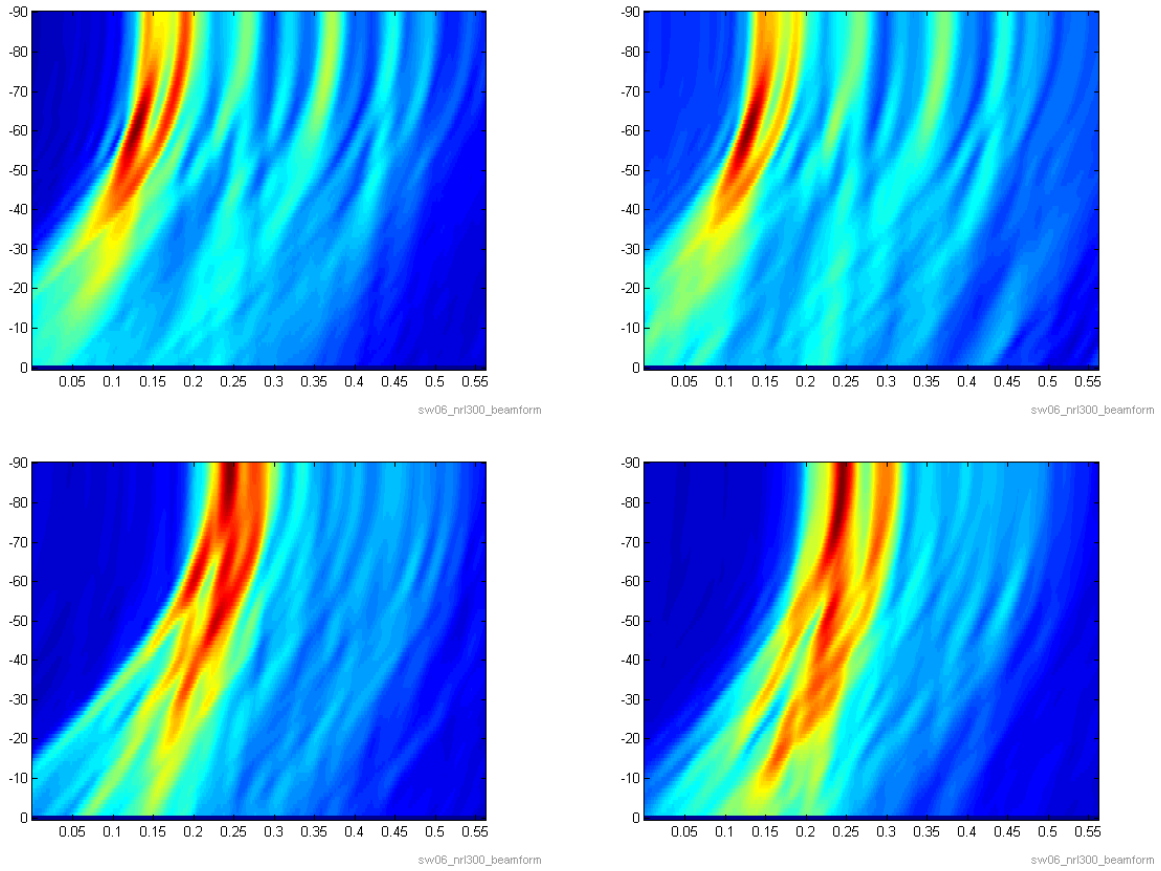

Figure 5.3: Beamforming results on Shark HLA

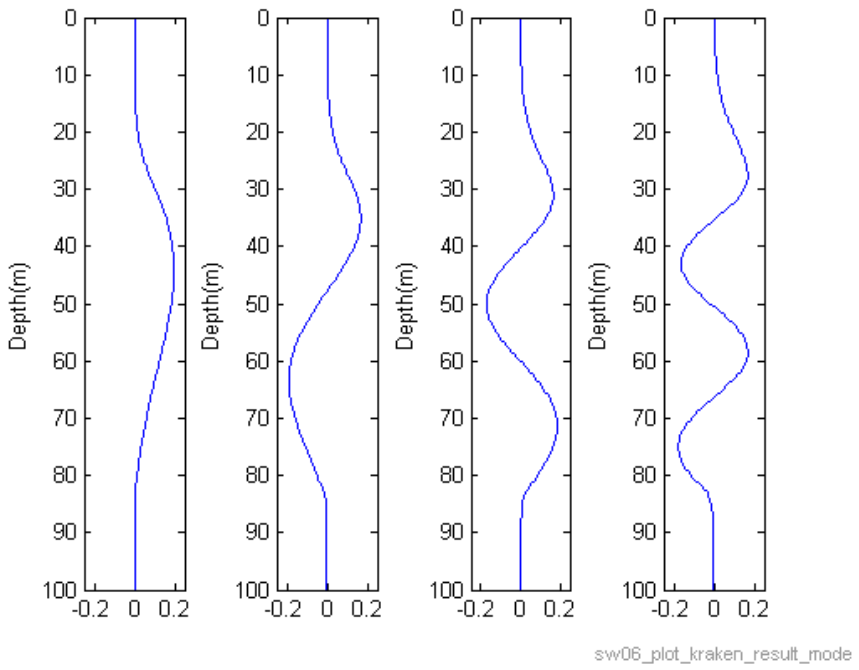

Figure 5.4: From left to right, vertical modes 1-4 excited by a 330Hz frequency signal. Temperature data were recorded at NRL300 source, GMT21:30, Aug 17, 2006.

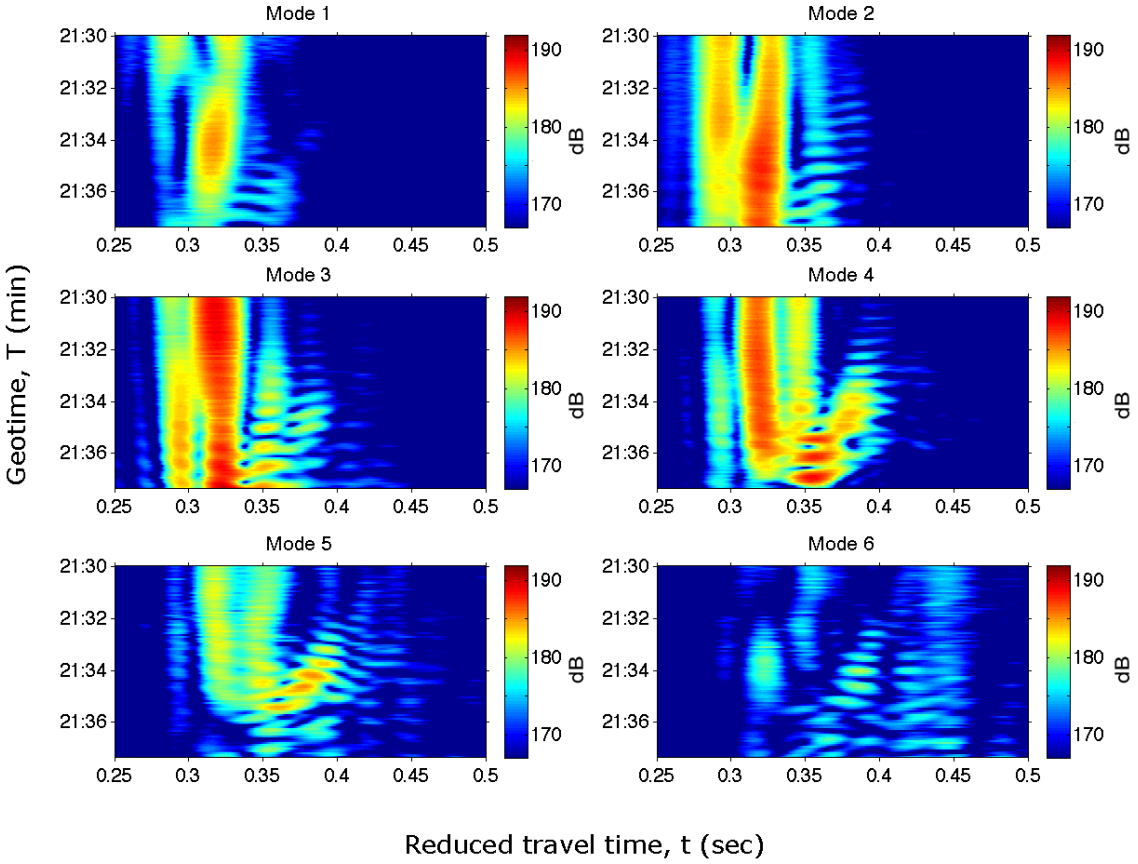

Figure 5.5: Broadband model decomposition of acoustic signal from 21:30GMT to 21:37GMT (mode1-6).

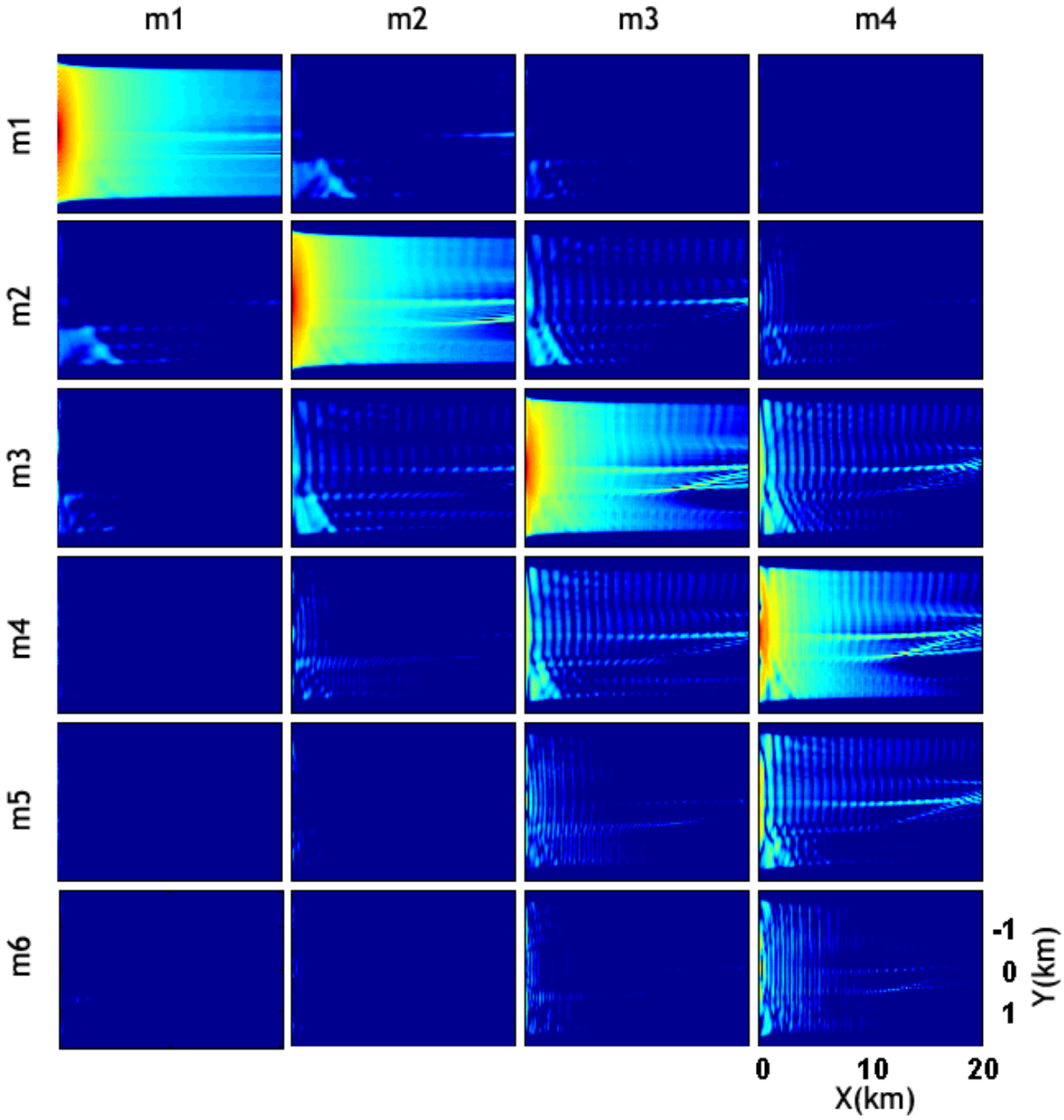

Figure 5.6: PE modal coupling. From left to right, the excited modes at source; from top to bottom, the coupled modes. Most energy is confined at the excited mode at the source, which is consistent with the theory about adiabatic propagation at near-parallel environment. Higher modes show stronger coupling effects than lower modes. Energy from mode 1 will couple to mode 3, while mode 4 can couple up to mode 8.

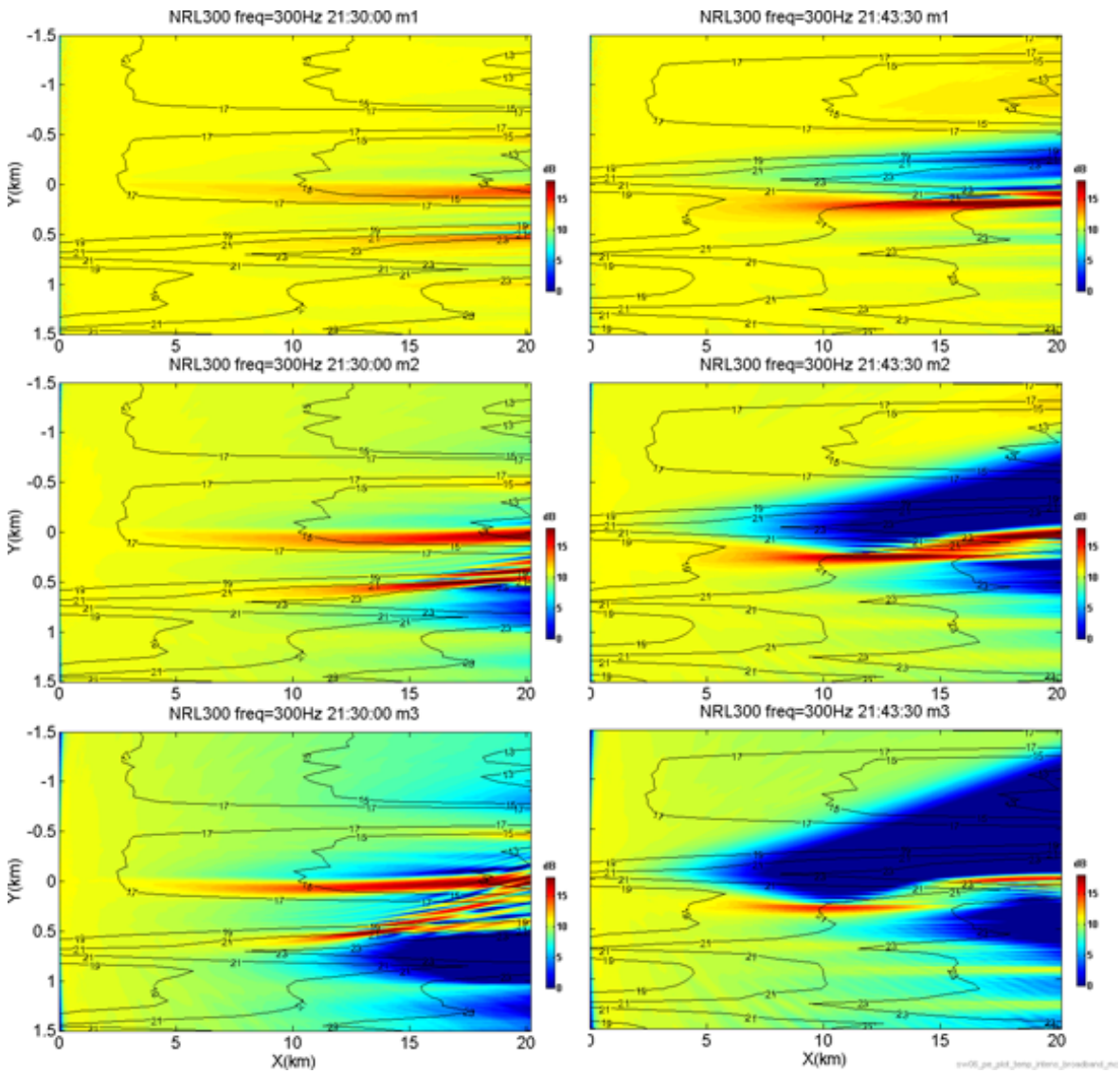

Figure 5.7: (Modal dependence) Acoustic intensity is shown for vertical modes 1 3 at GMT21:30:00(left) and GMT 21:43:40(right) respectively. A single frequency signal (330Hz) source is placed at (0,0), depth = 70m. Temperature contour overlay shows the passing internal waves.

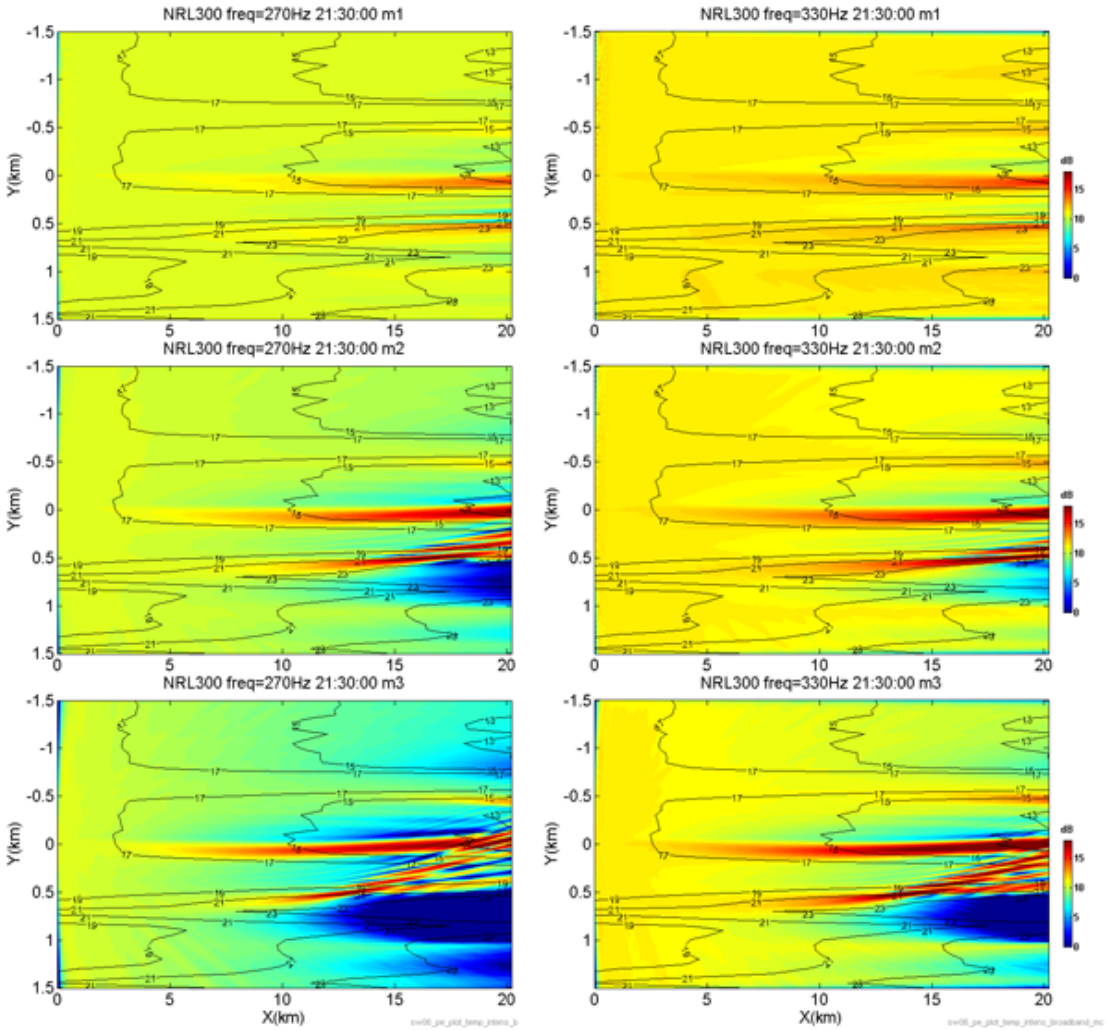

Figure 5.8: (Frequency dependence) Acoustic integrated sound intensity of vertical modes 1-3 at frequency = 270Hz, 330Hz at GMT21:30:00. Source position (x,y) = (0, 0) and source depth = 70m. Temperature contour overlay shows the passing internal waves.

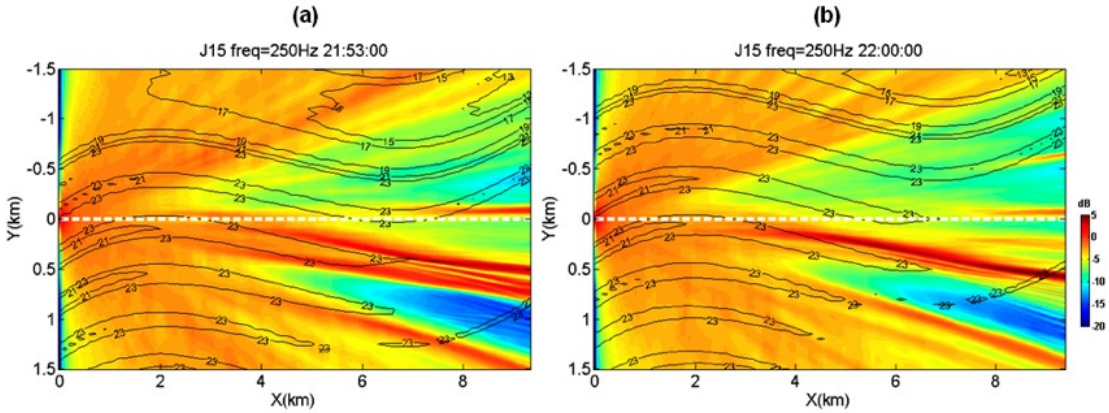

Figure 5.9: 3-D PE modeling results showing the acoustic intensity and the temperature contour at depth 20 m. Source is located at point (0,0) and white dashed lines indicate the acoustic track.

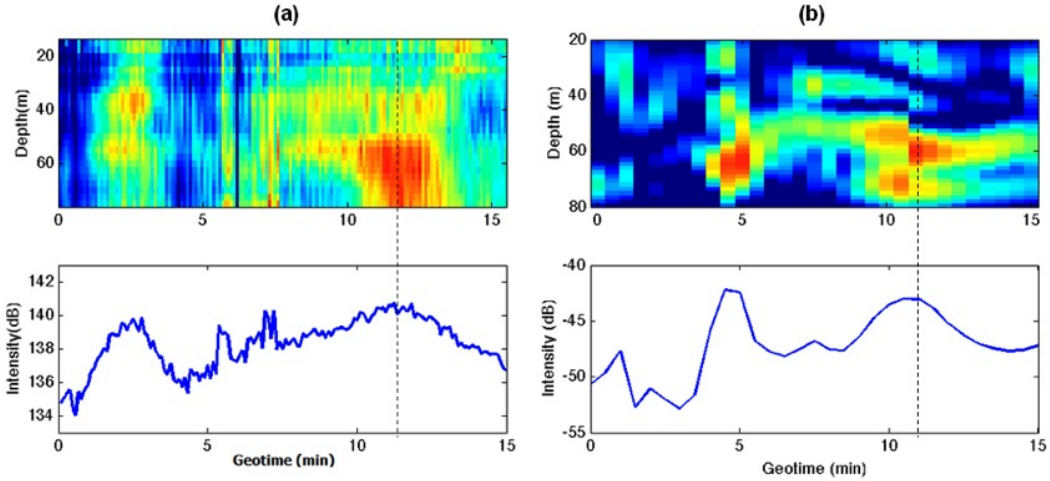

Figure 5.10: (a) Data and (b) model comparison of the intensity as a function of depth (top panels) and depth-integrated intensity (bottom panels) on Zone 3, August 17, 2006 at 22:11 to 22:26 GMT. The occurrence of focusing at geotime about 22:21:30 observed in the data was well predicted by the model.

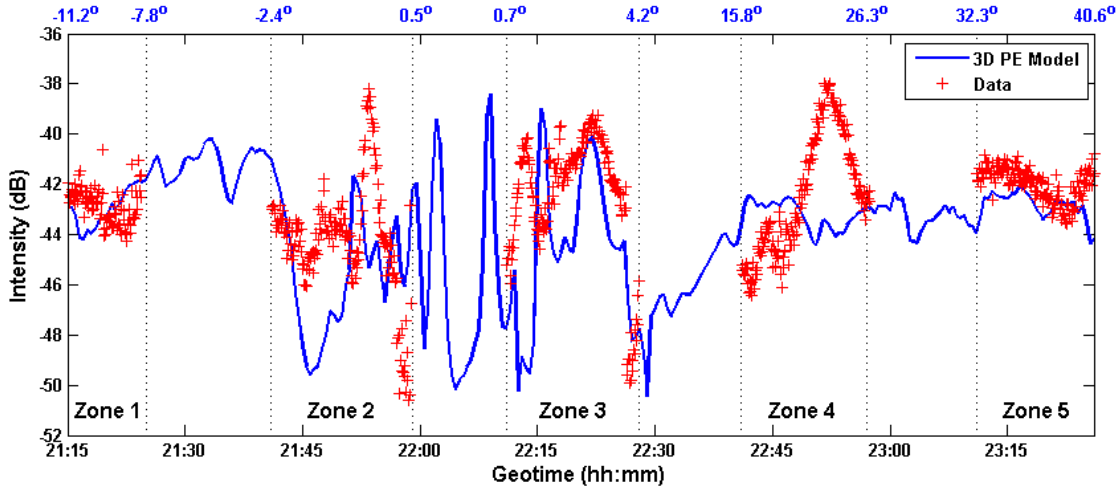

Figure 5.11: PE model results and experiment data comparison for moving source J15. Solid line shows the results of 3D PE model. The propagating angles are shown at the top for the beginning and end of each transmission session

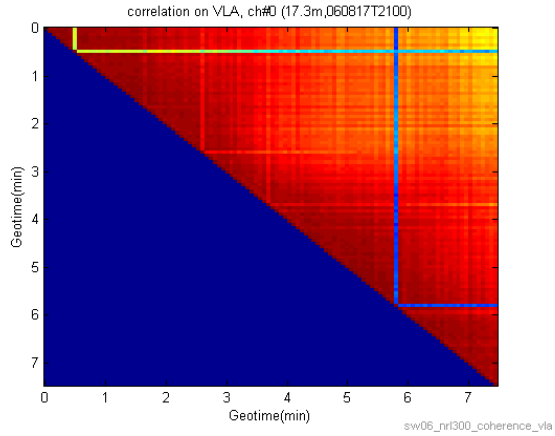

Figure 5.12: autocovariance function of channel 0 at 21:00

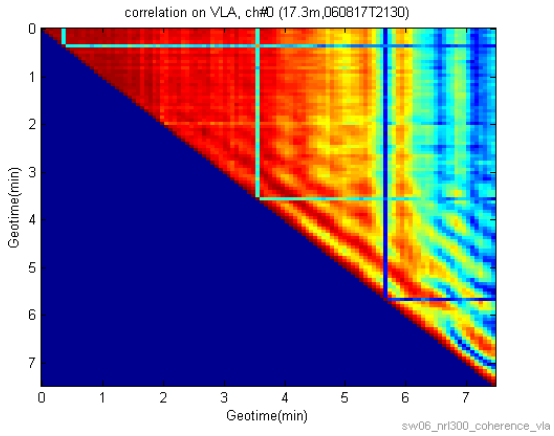

Figure 5.13: autocovariance function of channel 0 at 21:30

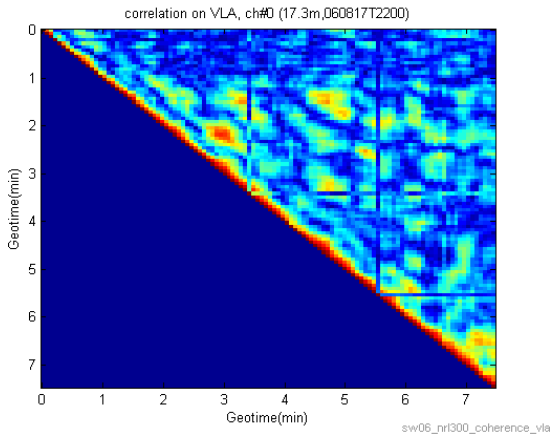

Figure 5.14: autocovariance function of channel 0 at 22:00

Chapter 6

SUMMARY

The SW06 experiment has provided high quality acoustic and environmental data to investigate the acoustic wave interaction with internal waves. Preliminary analysis of the acoustic data and observations of radar images and temperature records shows that during the passage of an ISW event, horizontal refraction results in significant acoustic intensity variation. This observation agrees with the recently proposed theory of sound propagation through ISW.3 Future work includes mode and frequency filtering of this acoustic data as well as modeling to establish the transition of acoustic field behavior from adiabatic to other mechanisms when an ISW passes an acoustic track.

BIBLIOGRAPHY

[1] Miles, J.W.,"Solitary waves", Ann. Rev. Fluid Mech., 12, 11-43

[2] Lee, Ch.-Y., and R. C. Beardsley, 1974, "The Generation of long nonlinear internal waves in a weakly stratified shear flows", J. Geophys. Res., 79, n. 3, 453-457

[3] Apel,. J.R., H. M. Byrne, J. R. Proni, and R.L. Charnell, 1975, "Observations of oceanic internal waves from the Earth Resources Technology Satellite", J. Geophys. Res., 80, 865-881

[4] L. A. Ostrovsky and Y. A. Stepanyants, Internal solitons in laboratory experiments: Comparison with theoretical models, Chaos 15, 037111 2005

[5] The 1998 WHOI/IOS/ONR Internal Solitary Wave Workshop: Contributed Papers, edited by T. F. Duda and D. Farmer, Technical Report WHOI-9907, 1999.

[6] J. R. Apel, Linear and nonlinear internal waves in coastal and marginal seas, in Oceanographic Applications of Remote Sensing, edited by M. Ikeda and F. Dobson CRC Press, Boca Raton, 1995

[7] J. R. Apel, L. A. Ostrovsky, and Y. A. Stepanyants. "Internal solitions in the ocean". Technical Report MERCJRA0695, John Hopkins APL, July 1995.

[8] Ji-xun Zhou, Xue-zhen Zhang, and Peter H. Rogers, "Resonant interaction of sound wave with internal solitons in the coastal zone," JASA 90(4), 2042-2054

[9] J. C. Preisig and T. F. Duda, Coupled acoustic mode propagation through continental shelf internal solitary waves, IEEE J. Ocean. Eng. 222, 256-269 1997.

[10] B. Katznelson and V. Petnikov, 2000,"Low frequency horizontal acousitc refraction caused by internal wave solitons in a shallow sea",it Acoustical Physics, 46 n.6, 774-788

[11] M. Badiey, Y. Mu, J. F. Lynch, X. Tang, J. R. Apel, and S. Wolf, Azimuthal and temporal dependence of sound propagation due to shallow water internal waves, *IEEE J. Ocean. Eng.* 27(1), 117129 2002.

[12] M. Badiey, B. G. Katznelson, J. F. Lynch, S. A. Pereselkov, and W. Siegmann, Measurement and modeling of 3-D sound intensity variations due to shallow water internal waves, J. Acoust. Soc. Am. 1172, 613625 2005

[13] Rubenstein,D. 1999, "Observations of Cnoidal Internal Waves and Their Effect on Acoustic Propagation in Shallow Water ", *IEEE J. Ocean. Eng.*24(3), 346-357

[14] Lynch, J.F.; Ying-Tsong Lin; Duda, T.F.; Newhall, A.E. 2010,"Acoustic Ducting, Reflection, Refraction, and Dispersion by Curved Nonlinear Internal Waves in Shallow Water", *IEEE J. Ocean. Eng.* 35(1) 12-27

[15] R. A. Kropfli, L. A. Ostrovski,T. P. Stanton, E. A. Skirta, A. N. Keane, and V. Irisov, "Relationships between strong internal waves in the coastal zone and their radar and radiometric signatures", *Journal of Geophysical Research*, Vol. 104, NO. C2, p.p. 3133-3148, Feb. 15, 1999

[16] M. Badiey, Y. Mu, J. Lynch, J. R. Apel, and S.Wolf, "Temporal and azimuthal dependence of sound propagation in shallow water with internal waves," IEEE J. Oceanic Eng. 27(1), 117-129 (2002).

[17] M. Badiey, B. G. Katsnelson, J. F. Lynch, and S. Pereselkov, "Frequency dependence and intensity fluctuations due to shallow water internal waves," J. Acoust. Soc. Am. 122(2), 747-760 (2007).

[18] Newhall, A. E., T. F. Duda, J. D. I. K. von der Heydt, J. N. Kemp, S. A. Lerner, S. P. Liberatore, Y.-T. Lin, J. F. Lynch, A. R. Maffei, A. K. Morozov, A. Shmelev, C. J. Sellers, and W. E. Witzell, "Acoustic and oceanographic observations and configuration information for the WHOI moorings for the SW06 experiment," WHOI technical report WHOI-2007-04, (2007).

[19] Collis, J. M., T. F. Duda, J. F. Lynch, H. A. DeFerrari, "Observed limiting cases of horizontal field coherence and array performance in a time-varying internal wavefield," JASA, this issue (2008).

[20] D.J. Tang, J.N. Moum, J. Lynch, P. Abbott, R. Chapman, P. Dahl, T. Duda, G. Gawarkieweicz, S. Glenn, J. Goff, H. Graber, J. Kemp, A. Maffei, J. Nash and A. Newhall, "Shallow Water '06 A Joint Acoustic Propagation / Nonlinear Internal Wave Physics Experiment", Oceanography , 20(4), 156-167, 2007.

[21] Newhall, A.E., Duda, T.F., Von der Heydt, K., Irish, J.D., Kemp, J.N., Lerner, S., Liberatore, S.P, Lin, Y.T., Lynch, J.F., Maffei, A., Morozov, A.K., Shmelev, A., Sellers, C., and Witzell, W. Acoustic and oceanographic observations and configuration information for the WHOI moorings from the SW06 experiment, Woods Hole. Oceanog. Inst. Tech Report, WHOI-2007-04, June 2007.